ABSTRACT

Title of Dissertation:	EFFECTS OF DOPING AND DEFECTS IN $BaSnO_3$ AND COVETIC ALLOYS
	H. M. Iftekhar Jaim, Doctor of Philosophy 2018
Dissertation directed by:	Professor Ichiro Takeuchi & Professor Lourdes G. Salamanca-Riba, Department of Materials Science and Engineering

Doping and defects have played major roles for optimizing the structural, electrical, optical and mechanical properties of materials over the centuries. With the advent of modern fabrication and characterization tools, we are engineering materials by modifying the fundamental structure at the nano-scale. Such research and innovations are necessary to find alternatives of the known materials to meet technological, economic and environmental challenges. In this dissertation, we will discuss two classes of materials to identify the effects of atomic level engineering on the enhanced properties of Covetic alloys and $BaSnO_3$ perovskites.

The first part of the thesis is based on the nanoscale and surface characterizations of the carbon doped metal alloys of aluminum and silver produced by the Covetic process. We have found the presence of sp^2 bonded 3D epitaxial carbon in graphene nano-ribbon form on the aluminum and silver atomic planes. Such directional presence of sp^2 carbon in the crystalline form along with other allotropes will be studied. Here, we have

detailed the bonding, strain, defect concentrations, and oxidation characteristics of these compositions, and distinguished Covetic materials from other carbon based composites. Covetic process is significant as it defies the traditional metal-carbon phase diagrams under non-equilibrium conditions.

The second part of the dissertation focuses on the $BaSnO_3$, a major candidate in s-band electronics and transparent conducting oxide industry. Here, we will demonstrate the role of oxygen vacancies for inducing high conductivity in the $BaSnO_3$ thin films from insulating state and their stability on single crystal substrates deposited by pulsed laser deposition. To further investigate the role of multi-valent rare earth element doping on optical and electronic properties, results of Lead (Pb), Bismuth (Bi) and Strontium (Sr) substitution by combinatorial synthesis of $BaSnO_3$ are presented. We have tuned the bandgap from 3 to 4 eV based on the substitutions, and observed clustering and in-gap states for Pb and Bi-substitutions, respectively. Lastly, experiments regarding the search of the $BaSnO_3$ based superconductors by carrier injection, multi-valent states and strain engineering will be discussed.

EFFECTS OF DOPING AND DEFECTS IN $BaSnO_3$ AND COVETIC ALLOYS

by

H. M. Iftekhar Jaim

Dissertation submitted to the Faculty of the Graduate School of the
University of Maryland, College Park, in partial fulfillment
of the requirements for the degree of
Doctor of Philosophy
2018

Advisory Committee:
Professor Ichiro Takeuchi, Chair
Professor Lourdes G. Salamanca-Riba, Co- Chair
Professor Richard L. Greene, Dean's Representative
Professor Manfred Wuttig
Associate Professor John Cumings

Dedication

To my late mother Bilkis Jaim who missed my graduation, my father Prof. W. M. H. Jaim and sister Dr. Jasmine Jaim. My father's Ph.D. in Economics from Imperial College London inspired me and my sister to pursue Ph.D. in western academia in different avenues, and my mother was always supportive in these three Ph.D. programs.

Acknowledgements

I would like to thank my advisor, Professor Ichiro Takeuchi, for his guidance in the last two and a half years in various projects which enabled me to learn through the different avenues of condensed matter physics and materials engineering. Without his support, it would not have been possible for me to complete this dissertation. I am very grateful for the AFSOR grant which funded me in this period.

I also have appreciated working with my co-advisor Prof. Lourdes G. Salamanca-Riba, who taught me the use of TEM & EELS with great care for over one year. Working with her under DARPA and ONR funded Covetic projects allowed me to learn metallurgy and low dimensional carbon analysis in great detail.

My sincere gratitude also goes towards the committee members of this dissertation: Prof. Richard L. Greene, Prof. Manfred Wutting, and Prof. John Cumings for their time and scholarly remarks about my research.

I would like to thank my first advisor Dr. Kevin D. Osborn at the Laboratory for Physical Sciences who generously funded me in my first year at UMD, and introduced me to the complicated realm of superconducting quantum computing. Under his supervision, I had the chance to work in one of the nation's premium federal labs, and learned many micro-fabrication techniques.

I wish to thank my former employer Dr. Karen Gaskell at the Surface Analysis Center for the graduate assistantship of over a year. It exposed me to an industry standard environment to run XPS, Raman and AFM, and analyze data like a chemist. Moreover, I have gained the experience of office management, and of dealing with a diverse class of surface analysis techniques.

For multiple collaborative projects on Covetics and 3D printed additive manufacturing, I am indebted to Dr. Daniel P. Cole from the U.S. Army Research Laboratory, Aberdeen Proving Ground. His excellent skills in KPFM were instrumental for the success of these projects. I would also like to thank Prof. Johnpierre Paglione and his group for allowing me to use their furnace lab frequently in Center for Nanophysics and Advanced Materials (CNAM).

I have greatly benefitted from my colleagues in the three different groups with whom I have worked for in the last 5 years. I wish to specially thank Dr. Seunghun Lee and Dr. Xiaohang Zhang for their contributions in my projects with Prof. Takeuchi on many different occasions including low temperature measurements, ion-milling, coating and XRD. Dr. Philip M. Piccoli was extremely caring to teach me the details of EPMA. I am also grateful to many of the CNAM staff members in the Department of Physics for their constant support for maintaining instrumentations and helping me out whenever I had technical issues. Dr. Joshua Higgins, Doug Bensen and Brian Straughn are the few names in the long list. Discussions with Dr. Ippei Suzuki, Dr. Gilad Kunse and Dr. Kamala Bharathi were resourceful regarding my research. Two undergraduate students Megan McGuffey and Edward Morozov played important roles in maintaining the PLD lab and target preparations for more than a year. I also wish to thank my colleagues Yangang Liang, Naila Al Hasan, Eric Marksz, and Drew Stask for their help from time to time. Our group alumni Rich Suchoski and Dr. Sean Fackler have helped me to solve the puzzles of graduate school.

In Covetic projects, I always got strong support from Romaine A. Isaacs for TEM sample preparation, SEM and analyzing the experimental results. Joshua Taillon

helped me to learn the Hyperspy program for PCA analysis. Xiaoxiao Ge was also helpful on many occasions. For complicated XRD phase analysis, the expertise of Dr. Peter Y. Zavalij's is worthy to note.

I wish to thank the staffs and directors of the AIMS Lab for their supports while using TEM, SEM and carbon coater. At Nano-center Fablab, Thomas Loughran, John Abrahams, Mark Lecates, and others always happily extended their hands whenever I used PECVD, ALD, LPCVD and wet benches.

It was an honor for me to work with the quantum physicists at LPS. Although I worked there for one and a quarter year only, I made very good friendship with my excellent colleagues and staffs. Dr, Yaniv Rosen was not only a good PostDoc, but also a wonderful person who patiently helped me out in a totally unknown area of physics and Labview programming. Dr. Bahman Sarabi, then a senior graduate student, mentored me in advanced fabrication techniques. His designs of resonator circuits were critical for our TiN kinetic inductor based project. Dr. A. N. Ramanayaka's expertise in mK- measurements, noise reduction techniques, and thoughtful feedbacks in fittings were important to explain two-level system contribution in my project. We also used resources form Dr. Ben Palmer's lab from time to time. Among many colleagues with whom I have shared office space and laboratories, a few include Dr. Nathan Siwak, Dr. Anita Roychowdhury, Dr. Joyce Coppock, Dr. Baladitya Suri, Shavindra Premaratne, Dr. Sergey Novikov, and Dr. Rich Leavitt. It was my pleasure to work with Dr. Cliff Hull, Toby Oliver, Dan Hinkel, Rob Gambella, Sean Flannery, Curt Walsh and Steve Brown in the cleanroom, and learn interesting things from Victor Yun in the lunch room.

Thanks to our former graduate program director Dr. Kathleen Hurt for guiding during the PhD program, and administrative staff Michael McNicholas, Olivia Noble, Kay Morris, Jenna Bishop at MSE department, Mary Sutton at CNAM and Althia Kirlew at LPS for constantly taking care of the issues that physicists and engineers are not at all good at.

I am also indebted to Professor K. Bärner of Georg-August-Universität Göttingen for his help in superconducting simulation research in my early graduate life.

Lastly, I wish to give special thanks to our department chair Professor Raymond Phaneuf and Dr. Christopher J. K. Richardson for mentoring me in my PhD program.

Table of Contents

List of Tables

List of Figures

Chapter 1: Introduction

1.1 Motivation

In this dissertation, we emphasize the role of doping and defects on the carbon nano-structure based aluminum (Al) and silver (Ag)-Covetic alloys, and thin films of barium tin oxide ($BaSnO_3$). In these material systems, we have used advanced characterization techniques to correlate the structural, electrical, optical and surface properties with the doping of different elements. We have also studied the effects of defects generated on the surface and the bulk in these materials. These materials have great significance for their future applications to meet the challenges of US national energy policies. Successful implementation of these materials will have economic benefits, and can create US jobs for both the high-tech industry as well as smaller industries.

The long-term goal of the US energy policy and defense strategy is to become independent in materials processing related to the electronics industry and infrastructure. In the first 9 months of 2017, the U.S. imported $687.2 million Al from China alone creating trade tensions [1]. The US is also purchasing electronic materials from many foreign countries such as China, Japan, South Korea and Germany for the semiconductor industry. Solar cells purchased from China have reached a staggering level of $5-8 billion in the last few years [2]. Therefore, it is necessary to find alternatives of the current materials to be competitive in the global market and to create these industries at home.

From environmental perspectives, both studied materials are vital to reduce green-house gas emissions by introducing novel solar cell materials, the consumption

of materials and upgrading the aging electrical grid systems. Some of the rare earth based electronics are highly toxic and expensive. Any geo-political crisis in the Asian region will severely impact the US economy and tech-industry because of the excess dependency on the foreign imports. One of the major options to avoid such scenarios is to explore novel materials.

The invention of better metal-alloys is important for the future infrastructure development in the upcoming years. For strategic purposes, the USAF and US Navy are searching for high strength and light-weight alloys. Therefore, detailed research on carbon based metal-Covetic materials are quite significant and meets the national interest. In the first part of the thesis, we will characterize these metal-Covetic systems with different techniques. Besides, among some of the top candidates in the materials research, a perovskite based oxide such as $BaSnO_3$ (BSO) is unique for its promising nature in diverse fields in electronics. In the second part of the dissertation, we will discuss the role of oxygen defects and chemical substitution by Sr, Pb, and Bi in BSO to tune the optical and electronic properties.

1.2 Study of Metal-Covetic

The first part of the thesis focuses on the characterizations of a novel nano-carbon structured metals named Metal-Covetics. In the Covetic process, a very high electric current is applied to the molten metal and carbon micro-particles are added simultaneously. Then it is slowly cooled down in an inert environment. These newly found alloys have shown enhanced mechanical, electrical and structural properties. Under DARPA and ONR grants, we have investigated the Al-6061 and Al-7075 Covetic alloys in detail, and contributed in surface and nano-scale characterizations of

Ag-Covetic. The success of our research has been to establish the Covetic process as a technique to overcome the barriers to form a graphene like structure in these metals which defies the traditional theoretical frame work based on the metal-carbon phase diagrams.

We have applied many different characterization techniques to identify the carbon doped structure by X-ray diffraction (XRD), Raman and transmission electron microscopy (TEM). We have shown the presence of carbon with epitaxal orientation with the metal at nano-scale in both dark field (DF) and bright field (BF) imaging, and electron energy loss spectroscopy (EELS). Selected area diffraction patterns (SADP) were obtained to identify the crystalline state of carbon in Al and Ag. The epitaxial nature of carbon creates strain and gives directional property which can be used to interpret the greatly improved properties. By ultra-high vacuum X-ray photoelectron spectroscopy (XPS), we have defined sp^2 bonding and level of oxidation in metal alloys. Therefore, we distinguished the alloy from other carbon doped systems with convincing evidence. It also helps to explain the possible mechanism of creating carbon ions which act like plasma in the metal matrix under non-equilibrium conditions. We have published these findings regarding the Al-Covetic in *Carbon* titled '*Sp^2 Carbon in Al- 6061 and Al-7075 alloys in the forms of Crystalline Graphene Nanoribbons'*.

With EELS and Raman, we have mapped the elements at high resolution and analyzed the chemistry of the bonds formed at atomic scale, and compared the variations of strain and defect concentrations due to gradual carbon doping on both Al-Covetic and Ag-Covetic. We have implemented the machine learning techniques to show that sp^2 bonded carbon is dominantly present in the materials by remapping with

an individual class of signals obtained by EELS. Also, KPFM results supported the previously observed results. In the second paper in *Carbon* titled *'Characterization of carbon nanostructures in Al and Ag Covetic alloy'*, we detailed these findings.

1.3 Study of Oxygen Vacancy Enriched and Site Substituted $BaSnO_3$

In the second part of this dissertation, the role of the vacancy enriched and site substituted $BaSnO_3$ will be explored in detail. Both pure and doped BSO compositions are showing promising results in opto-electronics [3], solar-cell electrodes [4], s-band wide bandgap semiconductors [5], gas sensors [6] and fuel cells [7]. Although BSO has been studied for gas sensor applications for quite a while, it came into the limelight in 2012 when La doping of BSO exhibited high conductivity and optical transparency[8]. Since then, a lot of studies have been conducted by various fabrication methods. Based on doping elements, various functional properties are observed. Currently, it is considered as one of the most prominent candidates for replacing indium tin oxide (ITO).

However, there are significant challenges for applying BSO in industry due to its insulating nature. Here, we will demonstrate a new technique to overcome the insulating behavior of the BSO by controlling the oxygen pressure in pulsed laser deposition (PLD). By X-ray photoelectron spectroscopy (XPS), we have explicitly shown the role of the oxygen vacancy as a donor state affecting the electronic transport and structural properties in BSO. Our contribution is important from several aspects. Firstly, it opens an avenue to rethink the theoretical background of band-structure calculation in s-band perovskite systems, an emerging field in semiconductors. Previously, there were discrepancies among the theoretical band structure calculations

and very recent experimental results of the oxygen deficient BSO without clear explanations. Our experimental technique can be applied in other perovskite systems to explore metal to insulator or semiconductor transitions in strongly correlated materials, and correlate with the oxygen defects.

Secondly, maintaining high conductivity with high optical transparency and crystallinity from the original insulator BSO without adding any dopant, and any post-processing such as annealing at very high temperature makes our processing technique applicable for practical uses. We succeeded in controlling different orders of conductivity by this technique creating a wide range of choices. This procedure might be used to fabricate all BSO based field effect transistor (FET). Dielectric and gate electrodes can be fabricated using BSO by just tuning the oxygen pressure. This will reduce fabrication steps and overall costs.

Thirdly, this work shows the stability of the oxygen deficient films even at fabrication temperatures of 760 ^{o}C regardless of substrates. This finding is critical for progressing all perovskite based electronics in field effect transistors as most of them become structurally and electronically unstable at high temperature limiting applications. We authored one article titled '*Stability Studies of the Oxygen Vacancy Induced Conductivity in $BaSnO_3$ Thin Films on $SrTiO_3$*' in *Applied Physics Letters* presenting these findings.

We have also studied the site substituted BSO structure. By chemical substitutions of the multi-valent elements such as Lead (Pb), Bismuth (Bi), and Strontium (Sr) in BSO, we succeeded in tuning the bandgap and optical properties. These studies have been carried out by combinatorial technique. Combinatorial

synthesis allows probing the material properties in a wide range of compositions fabricated at once. It is an efficient system for finding new phases, electronic and magnetic properties with reduced time and cost. Based on the results obtained from the first few samples, we focus on the narrow regions of interest. By substituting with these different elements, we tuned the optical band-gaps of BSO from 3 to 4 eV. We have observed that structural distortion, different valence states and the clustering of the elements are all correlated to the bandgaps. These samples give a wide range of choices for optimizing electrical and optical properties previously unknown to the scientific community.

We have discovered the role of clustering of Pb at higher concentrations to explain the non-monotonic change in band gaps with the help of the theoretical calculations based on the AVBN0 approach obtained from our collaborators. Similarly, for Bi-clusters, we have observed additional electronic states into the energy gaps. It is worthy to note that due to the presence of the strongly correlated systems, theoretical studies often fail to estimate band-gaps in these materials. Therefore, this high throughput based study can provide future guideline to improve the simulation techniques in $BaSnO_3$ and similar materials. These results are published in the *Chemistry of Materials (ACS)* titled '*Systematic band-gap tuning of $BaSnO_3$ via chemical substitutions: the role of clustering in mixed-valence perovskites*'.

Aside from the band-gap engineering, we have also studied the possibility of superconductivity in these stannate based materials. Search of novel superconductors are important to explore new quantum materials. Since the uses of perovskite electronics are rising, non-cuprate superconductors with simpler structures are getting

more attention. Our strategy was to inject excess carriers and create multi-valence states by doping with rare earth elements in various BSO compositions. This is a well-known method to study superconductivity in layered perovskite structures.

1.4 Outline of Thesis

In Chapter 2, we will briefly discuss the combinatorial PLD synthesis technique. Mostly similar characterization techniques are applied for the materials analysis in both parts of the dissertation. For quantifying the elemental compositions of the thin films, we have used Electron Probe Micro-Analysis (EPMA). Details of the valence states of the elements were analyzed by XPS. Different techniques of XRD were useful to analyze the structural properties, symmetry and epitaxial nature. Low temperature properties were measured in Physical Property Measurement System (PPMS). We performed atomic force microscopy (AFM) to characterize the surface topography and phases. To find nano-scale features, we have utilized TEM and EELS for the Covetic samples. Raman mapping was vital to characterize carbon bonding and defects. The fundamental basis of these instrumentations along with the commercial models will be discussed in this chapter.

In Chapter 3, the background and importance of carbon doped metals will be discussed. Briefly, the role of low dimensional carbon, its characterization techniques, and thermodynamic limits of the carbon solubility in metals is covered to realize the importance of the Metal-Covetic system. The setup for the Covetic processing will be described. We will present some of the mechanical and electrical properties of the studied Al-6061, Al-7075 and Ag-Covetics in this section.

In Chapter 4, the characterization results of the Al-Covetic samples will be presented. Presence of sp^2 carbon in crystalline graphene nanoribbon forms are confirmed by TEM, EELS, XPS and Raman mapping. These results explain the enhanced mechanical and electrical properties of Al-Covetic alloys. Future studies of these materials are suggested at the end of the chapter.

In Chapter 5, the surface and spectroscopic analysis of the Ag-Covetic samples are shown. Presence of sp^2 carbon networks enveloped by sp^3 carbon clusters are found in Ag-Covetic samples.

In Chapter 6, the background and past research works on BSO are summarized. We will introduce perovskite and oxide materials from general perspective, and will focus on the pure and doped BSO system. The limitations of the band-structure calculations will be discussed briefly.

In Chapter 7, we will present the effects of the oxygen vacancy in the BSO system. The fabrication process and characterization results will be discussed in detail. The contribution of the oxygen vacancy will be quantified to correlate with the structural and electronic properties. Moreover, the stability of these films under high temperature and oxygen pressure will be discussed.

In Chapter 8, Bi, Pb and Sr substituted BSO thin films fabricated by combinatorial synthesis will be analyzed. The effect of the site distribution of these dopants at various concentrations, and their contributions to the optical and structural properties will be investigated.

In Chapter 9, the experimental works for searching BSO based superconductor thin films will be discussed. By carrier injection using La doping and lattice distortion,

Sr, Pb and Bi-substituted BSO compositions are studied for superconductivity. The role of lattice mismatch to induce tetragonal nature is also examined in thickness gradient BLSO films.

Chapter 2: Experimental Setup & Characterization Tools

2.1 Thin Film Fabrication

2.1.1 Pulsed Laser Deposition

Pulsed laser deposition (PLD) is categorized as a physical vapor deposition (PVD) process. In PLD, photonic energy is utilized to ablate desired materials from the bulk known as target in a high vacuum system. The laser is focused with optical lenses and mirrors to create a small size of a focused laser on the surface of the target materials. Based upon the composition of the target materials and photonic energy, the target absorbs the incident energy and creates a plume. Perpendicular to the plume a substrate like silicon wafer piece or perovskite single crystals are placed on a heater. The PLD is a complicated process as parameters of the depositions are often cross-correlated with the distance between the target and substrate, laser energy, temperature, oxygen pressure and other reactant gases. The plume size and its energy are dependent on the fluency of the laser source and pressure of the gases inside the PLD chamber. The shape of the plume is critical to control the evaporation rate from the target surface. The plume contains atoms, molecules and particulates, and can be tuned by the laser energy and other physical parameters. The creation of the plume is a nano-second phenomena, and the deposition process takes place at micro second scale. The energy of the plume reaching the substrate surface is important for controlling the growth modes as it provides the kinetic energy of the ad-atoms to redistribute and surface morphology. The thickness of the deposited film can be controlled by the number of laser shots, the frequency of the laser and substrate temperature.

In the early days of PLD during the 1960s, photonic energy of a laser source was the Ruby laser. Later the Neon based laser excimer Yd:NAG and solid state lasers were used at different wavelengths [9]. The fluence energy and ablation rates are related to the laser types and frequency of the shots. The advantages of the PLD over other methods can be summarized as follows:

a. Stoichiometry: One of the major advantages of PLD is to precisely control the stoichiometry and layer by layer atomic depositions. This is especially useful in fabricating superconductor thin film where the order between the layers needs to be preserved. Similarly, the semiconductor thin films and other complex oxide systems are deposited by PLD.

b. Simpler system: PLD is relatively simpler system compared to molecular beam epitaxy and other sputtering systems where bias voltage and RF sources are involved for creating plasma. The designs are more flexible and less cumbersome than other processes. Also, low maintenance and cheaper costs of the PLD makes it an attractive option for many research labs in the long run.

One of the major disadvantages of PLD is the non-uniformity of the films in larger areas. Generally, the size of the uniform regions during deposition is around 1 cm^2, which is much smaller compared to the sputtering or other chemical vapor deposition (CVD) systems. There is always a thickness gradient along the radial distances which makes it difficult to study beyond the small region and the stoichiometry of the composition. Such variations create inhomogeneity in the chemical nature and the physical features such as surface topography. Therefore, PLD is an initial step of investigating new materials in a simpler and faster way.

2.1.2 Combinatorial Synthesis of Materials in PLD

Traditionally, materials are synthesized for a specific composition based on the theoretical background or experimental need, and then tested or analyzed to find the desired properties. In case, it fails to achieve the perceived goals, new material compositions are fabricated to redo the characterization and performance studies. Therefore, it becomes a tedious time consuming process to follow and expensive to perform for individual composition. Also, in many cases the properties of the unknown composition ratios which might have novel characteristics in other fields are not explored. To avoid these limitations, scientists in different fields such as pharmaceuticals, chemistry, and materials engineering, are using a method of named combinatorial science. In this process, spatial composition gradient materials are fabricated at once, and then the composition dependent properties are mapped to correlate the structure-property in a continuous manner.

Certain PVD based materials fabrication techniques such as PLD, E-beam evaporation, thermal evaporation, and sputtering systems allow utilizing the combinatorial techniques efficiently. By synchronizing lasers with the moving shadow masks, it is possible to tune the deposition and create a gradient of materials.

2.1.3 Combinatorial PLD Setup

The PLD system used in this dissertation has a carousel to hold different targets which could be rotated with a computer controlled dc motor in accordance with the desired ratio of the elements during deposition (Figure 1). Another ac motor keeps the targets rotating in their own axis to make sure that the circumferential areas are utilized. The PLD targets are prepared in lab by conventional solid state reaction methods. This

multi-target system gives the opportunity to precisely control the ratios of elements in the single films, multi-layer and combinatorial film depositions. The laser pulse and the movement of the targets as well as the shutter are synchronized by a Labview based program created by the Neocera Company. The substrates are attached with silver glue for better thermal homogeneity on the heater surface and can be heated up to 900 ^{o}C. Oxygen gas is injected at a specific pressure from cylinders through controlled valves. To maintain high vacuum, a turbo-pump is used with a supporting roughing pump.

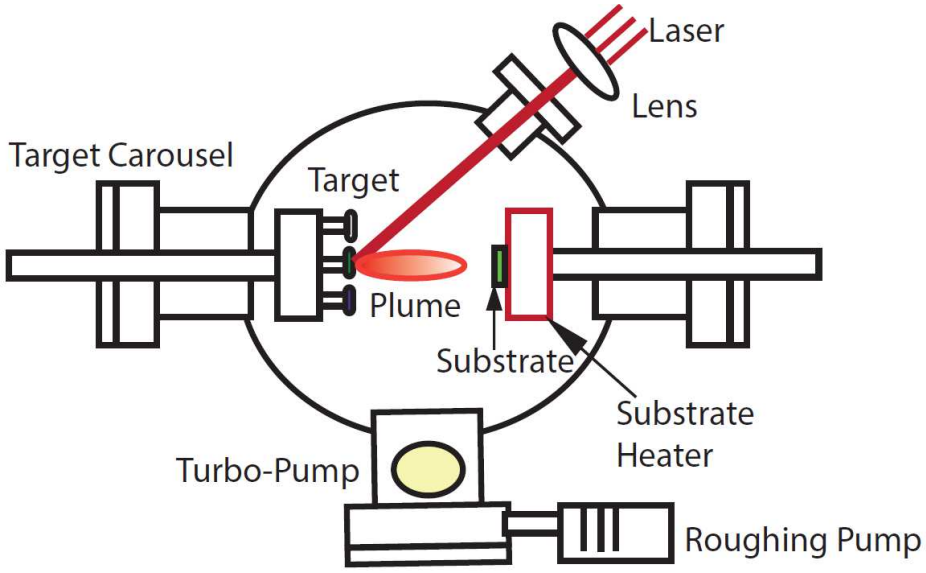

Figure 1: Schematics of a PLD system.

In combination of the two steps in one cycle shown in Figure 2, a flat film is deposited on the substrate with varying composition from end to end. The thickness in each cycle will be less than one unit cell. During the first step, the shutter opens up the substrate surface gradually while the laser is fired to deposit the film from one target. In the second step, the shutter opens up in the opposite direction to deposit a gradient film from another target in the opposite direction of the first step. This ensures that the film remains flat. The setup used in this dissertation is shown in Figure 3. Additional

photos in Figure 4 and Figure 5 show the inside of the PLD chamber, target holders, plume and shutter mask components.

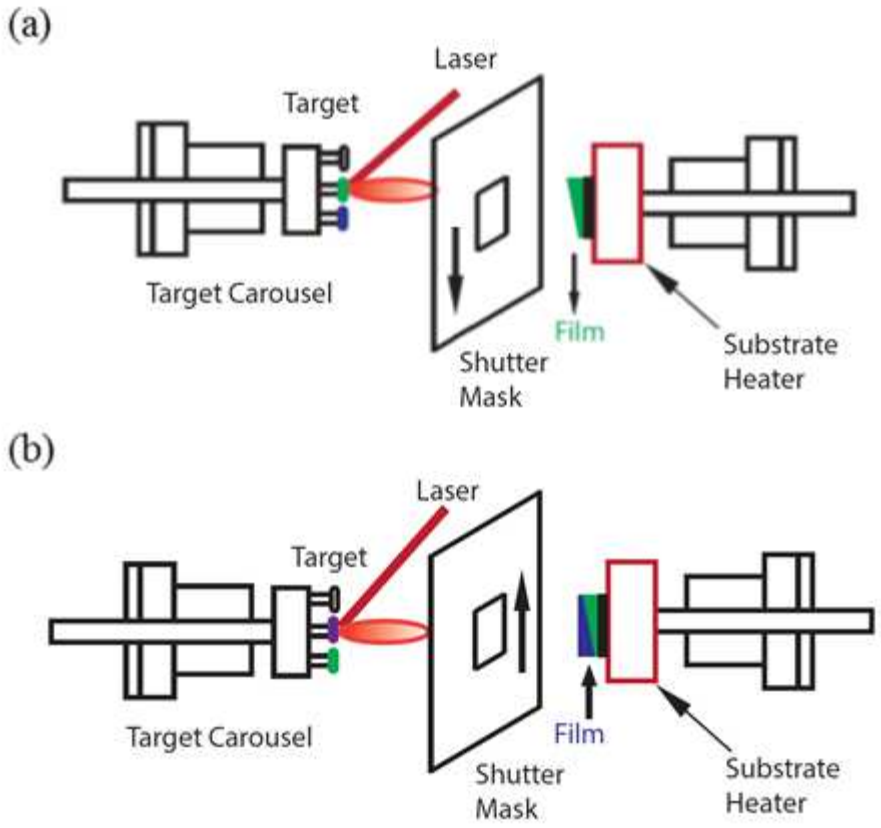

Figure 2: Combinatorial film synthesis. (a). During the deposition from the green colored target, the shutter mask with opening moves in an downward direction creating a gradient of thickness of the film. (b) During the second deposition from the purple target, the shutter mask moves in the upward direction with a gradient on the other end.

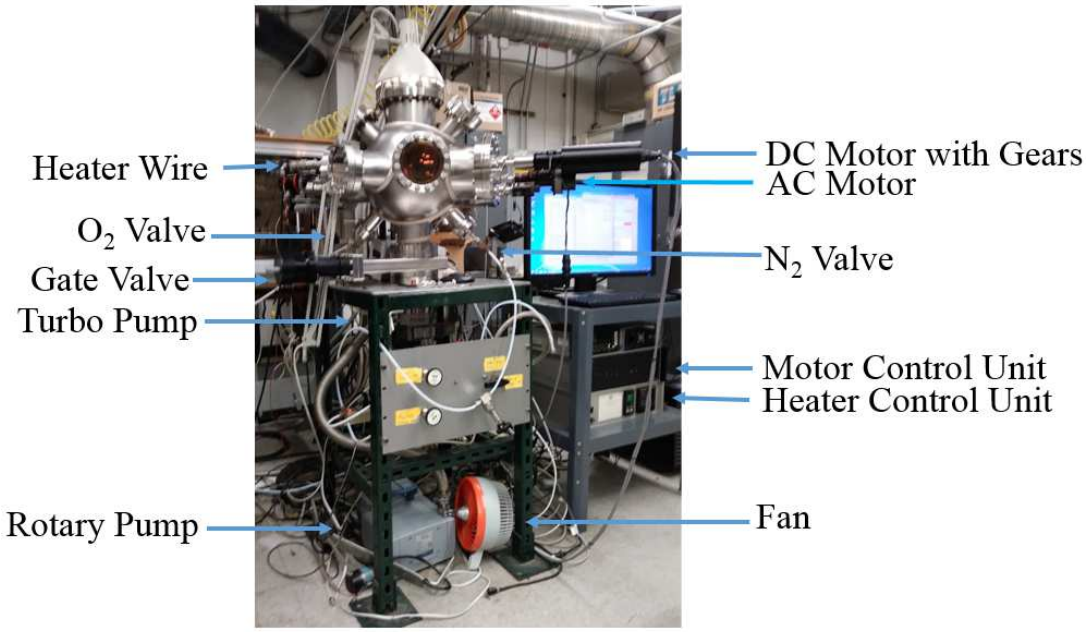

Figure 3: Combinatorial PLD setup at CNAM for the thin film fabrications.

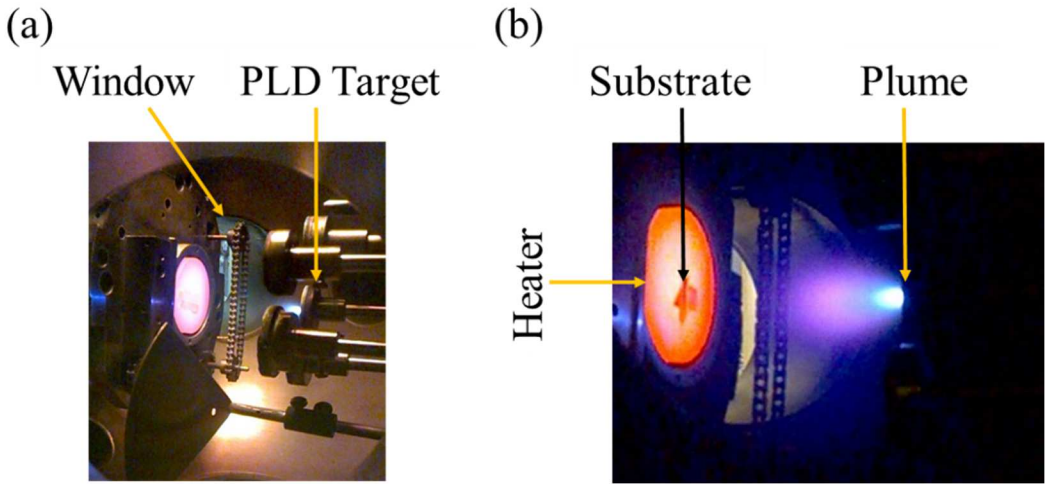

Figure 4: (a) Fabrication of a single composition film in the PLD chamber. Substrates are attached on the heating stage. (b) Zoomed figure of the plume expansion on the target once the laser hits.

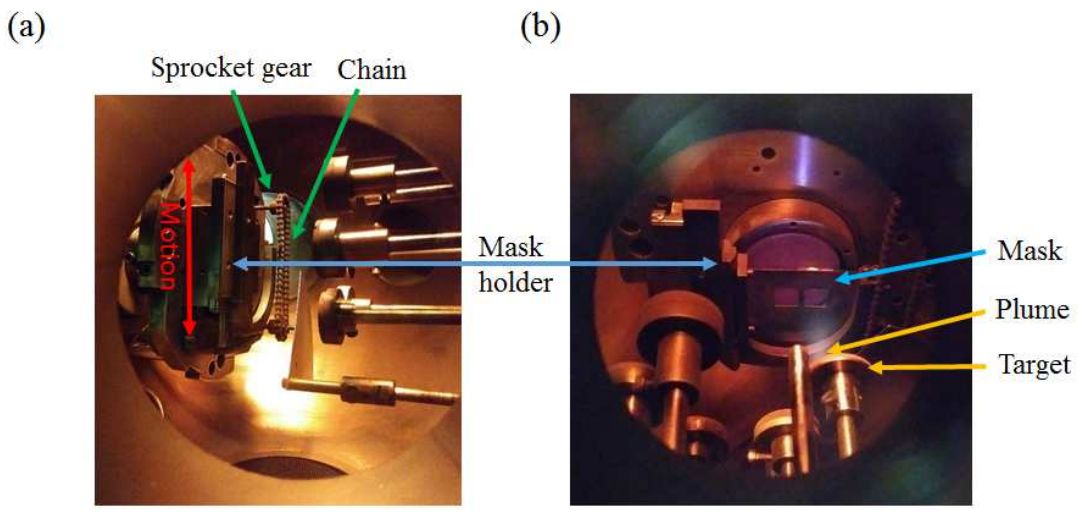

Figure 5: (a) Side-view of the combinatorial film fabrication setup with mask shutter and gears. (b) Photo taken from the top window when the laser was hitting the target creating the plume and the mask was moving accordingly.

2.2 Characterization Techniques

In this section, different techniques used for the characterization of the samples will be discussed. To study the structure of the fabricated thin films and Covetic alloys, XRD was used. Wavelength dispersive X-Ray spectroscopy (WDS) quantified the bulk composition of the elements. Surface characterization techniques such as XPS, AFM and Raman mapping were mostly used to find bonding details, surface topography and defect distributions, respectively. We will also discuss PPMS and TEM in detail.

2.2.1 Wavelength Dispersive X-Ray Spectroscopy (WDS)

WDS was used to find the composition ratio of the elements for both the single and combinatorial films. The instrument is calibrated with standards before acquiring data for each element in the sample composition. The system operates under high vacuum pressure. Visual positioning of the samples are done by scanning electron microscopy and optical camera. Detectors are made of PET and LiF crystals of specific

lattice parameters to count x-rays. The sampling zone was 30 μm for each measurement under 15 KeV. The X-ray penetrates the thin films and the substrates, and emits secondary electrons at a specific wavelength based on the elements and bonding. In WDS, the peaks are detected at different points of the Rowland circle which can be adjusted by the sample and detector positions. The high spectral resolution ranging from 1 eV to 10 eV ensures elimination of other close peaks or the contribution from the background arising from other elements. The WDS is accurate at a level of a fraction of a percent compared to other characterization techniques for quantification like EDS because of its ability to separate wavelength peaks positioned very closely.

A JEOL JXA-8900 electron probe microscopy analysis (EPMA) configured with 5 spectrometers was used for studying the samples for both quantitative and qualitative analysis with programmable position capability (Figure 6). The instrument also considers the effect of substrates on the films. The instrument has EDX capability to quickly scan the elements.

Figure 6: WDS Setup at IREAP

2.2.2 X-ray Diffraction (XRD)

XRD is a very common technique to study the crystal structure by coherent scattering of X-rays which gives constructive interference following the Bragg's condition,

$$n\lambda=2d\sin\theta \quad (1)$$

where, λ, d, n and θ are the x-ray wavelength, inter-planar spacing, an integer and incident angle, respectively. In every XRD instrument, there are 3 basic parts—X-ray tube, detector and sample holder. A target source Cu is bombarded with accelerating electrons from a heated filament to generate X-ray. A filter of Cu crystal mono-chromator is used to suppress the higher order components. For Cu single crystal, $\lambda=1.5418\ ^{0}A$.

In this dissertation, D8 from Bruker was used to find out-of-plane lattice parameter by θ-2θ scans. For finding the in-plane lattice parameter, reciprocal space mapping (RSM) have been done with scintillator detectors. RSM gives the in-plane strain and can confirm whether the film is relaxed or strained. It is a set of scans for getting 2D information with intensity variations and takes a much longer time than other scans. It also provides information about the layer quality of the thin film. Mismatch and threading dislocations in epitaxial layers can give rise to peak broadening which appear as dispersed colored area in the maps. We have used Topas XRD software to analyze the XRD data by fitting with the pseudo-Vogit method. The crystallinity of the films can be determined form the FWHM of the film peaks. The FWHM is calculated after subtracting the effects arising from the Cu K-α2 contribution (Figure 7).

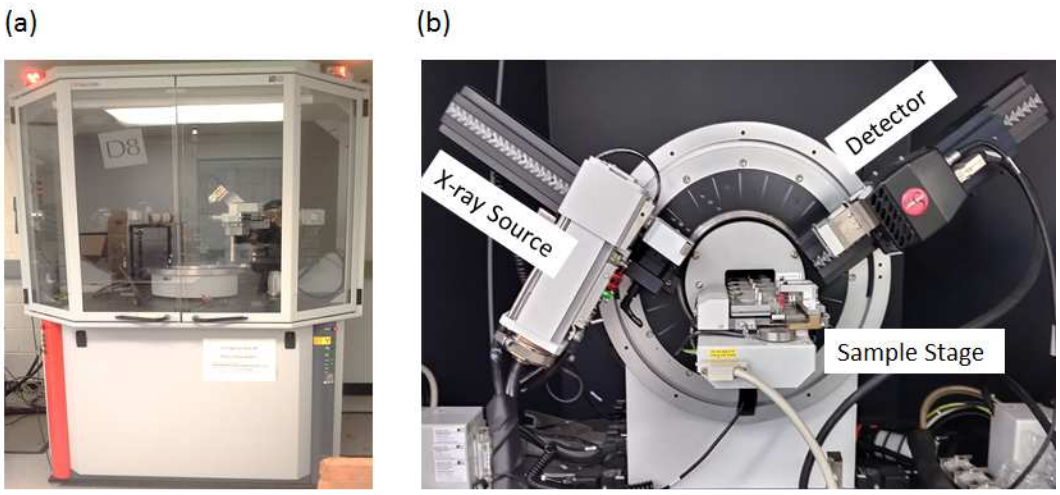

Figure 7: (a) D-8 Bruker XRD setup at CNAM for characterizing epitaxial combinatorial films. (b) D-8 Bruker at Chemistry Building for measuring single film compositions and bulk Covetic samples.

2.2.3 X-ray Photoelectron Spectroscopy (XPS)

XPS is a surface sensitive technique to find the atomic concentration, valence states and bonding information in different classes of materials such as polymers, nitrides [10], semiconductors and carbon based compositions. The mono-chromatic radiation from Al or Mg is used as a source to generate X-rays which irradiate a sample with soft x-rays of 1 keV to ionize atoms and release core-level photoelectrons. These emitted electrons are detected by the hemispherical analyzer and multi-channel electron detection system connected with the optical amplifier.

In our experiments, a high sensitivity Kratos AXIS 165 spectrometer was used with Al mono-chromator as a source. The chamber is maintained at ultra-high vacuum condition to detect electrons and avoid contaminations. The hemispherical analyzer has

a radius of 165 mm and eight channel electron detection with Al source gives a resolution of 0.7 eV (Figure 8).

Three energy parameters are important to interpret the XPS results. These are kinetic energy (K.E.), binding energy (B.E.), and photon energy (hν) of the source dependent upon the X-ray source. While the K.E. is an independent parameter, the B.E. depends upon the energy source and the work function (Φ_{sample}) related by the following equation:

$$K.E. = h\nu - B.E. - \Phi_{sample} \quad (2)$$

XPS can distinguish different elements by the position of the binding energy and spin orbital splitting of the elements. Peak area ratios are used to quantify relative presence of the certain elements considering the relative scattering factors.

Since XPS is a surface sensitive technique, the intensity with depth follow the Beer-Lambert Law.

$$I_s = I_o\, e^{-d/\lambda} \quad (3)$$

where, I_s is the attenuated intensity at the surface, I_o is the intensity of the electron at depth d from the surface, and λ is the inelastic mean free path of an electron inside the solid. Generally, the sampling depth for XPS is around 6-8 nm with exponential decay of the signal from the surface. To obtain data beyond the surface, Ar-sputter of the samples are often carried out. Therefore, it is possible to get depth profiles of the elements. Such experiments are useful to distinguish the surface states from the bulk states as well as to investigate multi-layer systems. However, in many cases, the selective sputtering rates of different elements limit such opportunities.

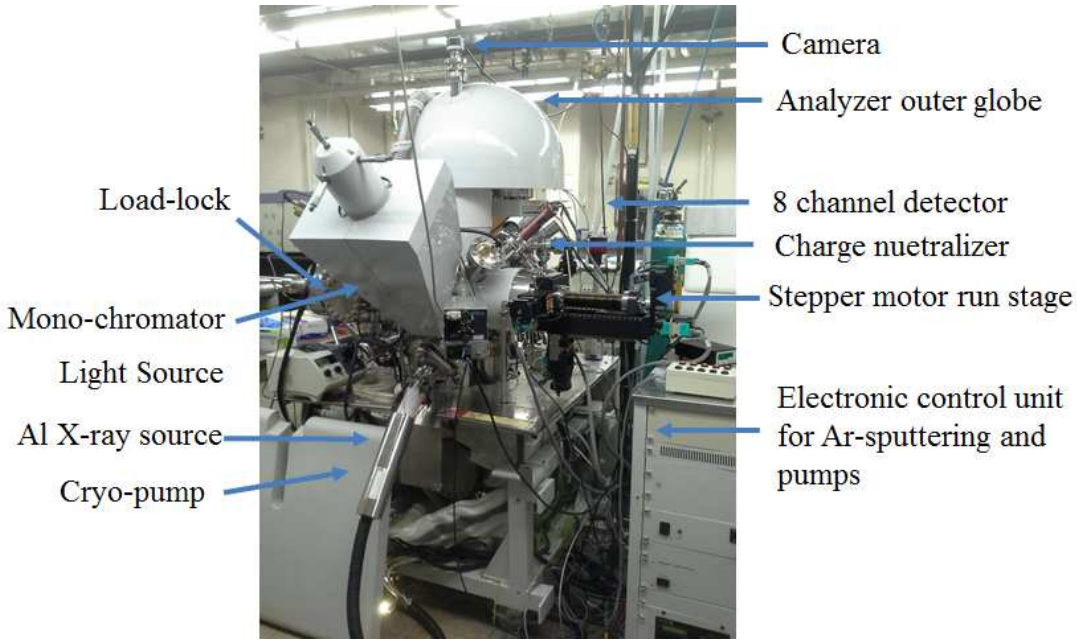

Figure 8: Kratos 165 XPS in Surface Analysis Center (SAC), UMD

The obtained peaks are background subtracted due to the inelastic scattering in the higher binding energy regions. Apart from identifying the elements, XPS also provides information about the chemical nature of the bonding. The shift in the binding energy suggests the change in electrostatic energy due to the adding/removing of chemical species. Once calibrated with the binding energy of adventitious carbon, the valence states can be confirmed for each element. Valence number is an important parameter which affects the oxidation, semiconductor behavior and optical properties.

2.2.4 Atomic Force Microscopy (AFM)

AFM is a surface morphology imaging technique at nano-scale. AFM gives information about the surface roughness, chemical nature and growth models of thin films, bulk materials and polymers. In the experimental setup, the sample is glued over an iron disc, and set on a piezoelectric base for controlling the movement precisely by external voltages. It combines a laser source with sensitive array of photodetectors to

sense the reflected beam from the top of a cantilever end. A stylus with around 8 nm diameter end is attached to a cantilever often coated with gold for sensing the force from the surface due to atomic interactions. The resulting displacements are read by the position of the laser on the photodiodes. The interaction of the surface and AFM tip is adjusted by a Proportional-Integral gain controller. The whole setup is on a floating table to avoid any vibration from external sources (Figure 9).

AFM height images show the roughness, grain boundary and the growth modes. The phase images are useful to distinguish between the different chemical boundaries or zones. The attractive or repulsive interaction force between the tip and surface changes depending upon the chemical nature during phase imaging. Based on the tips, the AFM cantilever tip vibrates at its resonant frequency to probe the sample. Although the positioning of the tip is done by using optical cameras initially, the fine tuning is done by automatic sensing.

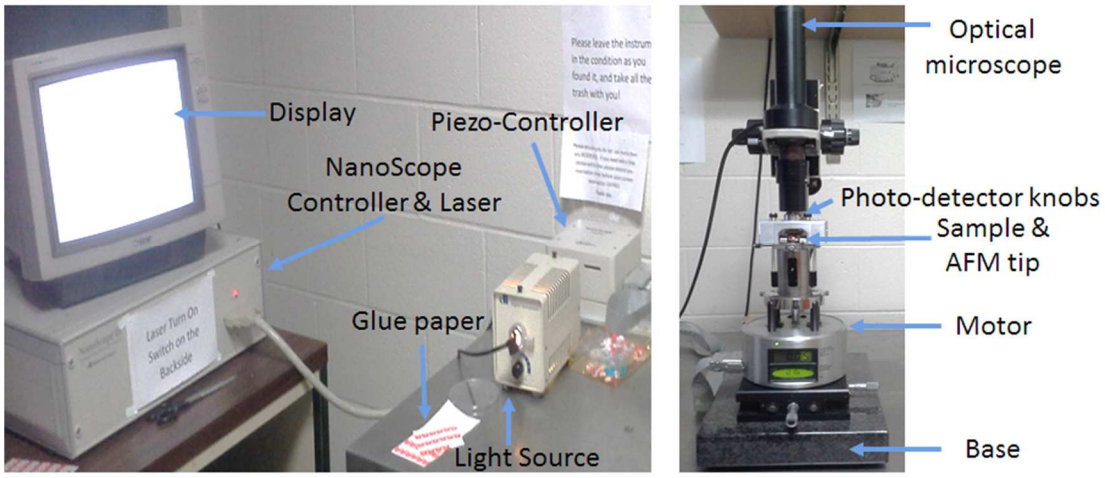

Figure 9: Different parts of the Veeco-Multimode AFM with a Nanoscope III controller located at SAC, UMD.

2.2.5 Kelvin Probe Force Microscopy (KPFM)

KPFM is very similar to AFM except that it has an external current circuit added with the tip to map voltage potential while taking regular AFM. In our study, a platinum silicide -coated tip (PtSi-FM, Nanosensors) with a radius of curvature of 25 nm is used. This image is coarser than the normal AFM because of the larger tip size. The resonance frequency and spring constant were 75 kHz and 5 Nm^{-1}, respectively. Under ac mode operation with a scan rate of 1 Hz, height, phase and KPFM maps were captured. The difference in work function between the tip and sample is transformed into relative surface potential maps. The advantage is based on differentiating elements and phases of dissimilar electronegativity which is not possible in normal AFM. Such images are useful to determine the nano-scale electronic properties as well as the distribution of the doping element in a matrix. In our experiments, we have used Cyper Asylum model KPFM as shown in Figure 10.

Figure 10: Cyper Asylum model was used for KPFM mapping.

2.2.6 Physical Property Measurement System (PPMS)

PPMS is widely used to characterize low temperature properties of the materials. It gives accurate values of temperature dependent resistivity and Hall effects from room temperature down to 1.8 K. This enables finding the conduction mechanisms, identifying the carrier types in semiconductors, and determining hall coefficient. By evaluating the temperature dependent resistivity, it is possible to determine the scattering mechanisms and localization effects in the materials. It can also observe spin flip temperatures and superconducting transitions. Data derived from the Hall measurements gives the carrier concentrations and mobility of the samples. Therefore, the use of PPMS is very wide in condensed matter physics. The closed cycle Helium circulation makes it easier to handle and quickly measure different properties at a single loading. In our research, Quantum Design PPMS SQUID has been used (Figure 11). Samples were loaded in a puck where 3 small samples can be accommodated at once. Samples loaded need to be pre-evaporated with Au-electrodes and wired with a wire bonder with Al to the puck in a standard four probe configuration. The outer electrodes supply current and the middle ones measure the voltage. The measurements were carried out in the constant current mode. So, the supplied current adjusted to the varying resistivity and polarization of the connections were reversed to average out the signal.

(a) (b)

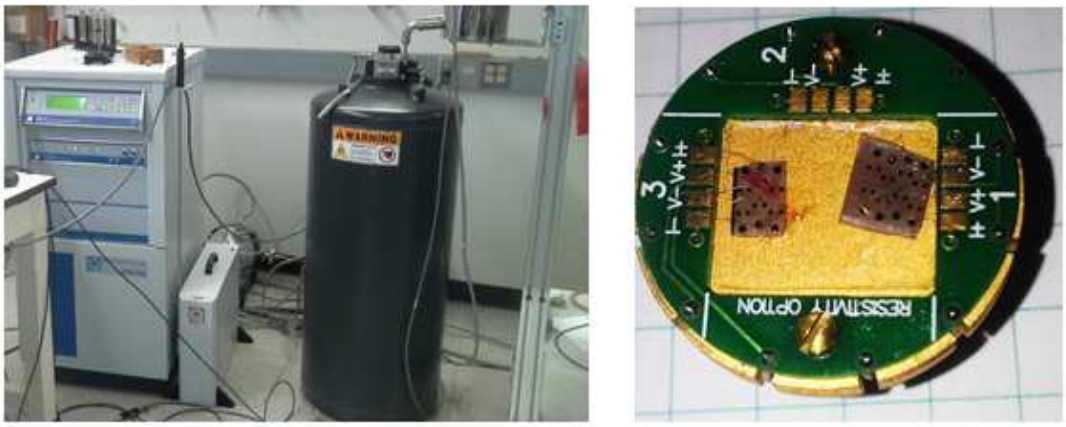

Figure 11: PPMS setup with holder design. (a) Quantum Design PPMS setup at CNAM. It has a magnetic field up to 9 Tesla. (b) PPMS sample holder with ion-milled, Au-coated and wire bonded BSO samples for four probe measurements.

2.2.7 Ultraviolet–Visible Spectroscopy (UV–vis Spectroscopy)

From the optical properties point of view, absorption coefficient in the desired visible range and bandgap are the most two important parameters for characterizing the transparency of the fabricated films. UV–vis spectroscopy is often used to characterize the absorption coefficient of the thin films or other materials with varying wavelength. This is particularly important to derive the bandgap by Tauc fitting of the absorption spectra. The absorption coefficient is calculated from the following formula:

$$\alpha = \frac{1}{t}\ln\left[(1-R)^2 / T\right] \quad (4)$$

where, t is the thickness, R is the reflectance, and T is the transmittance. The bandgap can be derived using the absorption coefficient data plots.

$$\alpha h\nu = (h\nu - E_g)^r \quad (5)$$

The value of r depends on the materials and specific measurements.

r = 1/2 for direct allowed transitions.

r = 3/2 for direct forbidden transitions.

r = 2 for indirect allowed transitions.

r = 3 for indirect forbidden transitions.

The band-gap in semiconductor materials can be widened by doping. Heavy doping causes the displacement of the Fermi energy level into the conduction band. Such shifts are known as the Burstein-Moss shift (ΔE_g). This can be correlated with the free carrier concentration (n) and effective mass (m^*) by the following equation:

$$\Delta E_g = \frac{\hbar^2}{2m*}(3\Pi^2 n)^{2/3} \quad (6)$$

In this thesis, we used the Cary 5000 UV-Vis spectrophotometer for optical characterizations. By using a sample holder consisting of 1 mm diameter aperture, it was possible to locally probe the combinatorial deposited films on LAO substrates.

2.2.8 Transmission Electron Microscopy (TEM)

TEM is considered as one of the most sophisticated materials characterization tools. Utilizing the wave-particle duality of electrons, images are captured at nano-scale resolution by the transmitted electron beam for very thin samples. An electron beam is generated from sources like LaB_6 which passes through different electromagnetic lenses to focus on the desired spot. By changing the voltages of the magnetic coils, it is possible to control the width and intensity of the electron beam to image different scanning areas and vary the contrast. The transmitted beam is detected in highly sensitive CCD. All these operations are done at high vacuum pressure to avoid contaminants and to ensure long mean free paths. TEM is very sensitive to the height

adjustment and uniformity of the samples below 100 nm. This makes the sample preparation quite challenging and requires very careful hands to polish, clean and set the sample on the TEM holders. To clean up the surface or make it thinner, low power ion millings are carried out at low energy. In case of thin films, it is better to prepare samples using focused ion beam (FIB).

There are certain types of imaging that gives TEM an advantage over other techniques. Bright field (BF) imaging is done by using the transmitted beam while the dark field (DF) imaging utilizes the diffracted beam for imaging. In BF imaging, weakly diffracting regions (thin and low atomic number elements) appear bright.

Modern day TEM instruments have additional components such as EDS and EELS. Therefore, it is possible to carry out EDS and ELLS from much smaller areas compared to the SEM and gain elemental information. In this case, TEM is operated under scanning transmission electron microscopy in contrast to a static beam. The incident beam interacts with the electrons from different shells from atoms in the sample and secondary electrons are ejected. The transitions of the electrons at different energy levels result in emission of photons. These x-rays are detected by a multichannel analyzer, and elemental maps are plotted in real time.

In this dissertation, a JEOL 2100F Field Emission TEM was used for obtaining BF and DF images. SADP and EELS to characterize the Covetic samples. In the following table the instrument operating parameters are listed.

Table 1: Operating parameters for TEM

Parameter	Values
Voltage	200 KV
Specimen chamber base pressure	10^{-6} Torr
Lattice resolution	0.10 nm

Spherical aberration coefficient	0.5 mm
Point-point resolution	0.19 nm
Pixel & spot size under STEM mode	1.5 nm

2.2.9 Electron Energy Loss Spectroscopy (EELS)

To obtain near atomic resolution of this elemental composition distribution imaging, another very useful tool often used is EELS. EELS is useful to determine the local bonding and electronic structures. Some of electrons in the transmitted beam loose energy while passing through the sample. This inelastic scattering gives rise to a loss which have characteristic values and pattern from each element and their corresponding transitions between shells. The EELS signal is collected at a spectrometer below the sample stage through a narrow window to filter out the high energy electrons. In the post processing of the data, it is important to consider the contributions from the zero peak loss (ZPL), and to subtract it from the raw data. This technique is extremely sensitive to vibrations and external electromagnetic interference. So, caution must be taken while capturing the EELS mapping. In our case, EELS was obtained using a Gatan GIF Tridiem post column energy filter in a JEOL 2100 Field emission TEM. The software system is capable of offsetting small movements by the image recognition techniques. It reduces the role of vibrations or sample displacements. We have used Gatan Digital Micrograph software for background subtraction using power laws and plotting the maps.

To mathematically analyze the EELS signal, we used a python based program Hyperspy 8.0 to apply blind source separation (BSS) of the most repetitive data by statistical analysis of the acquired signals. This allows replotting on the basis of the

most dominant signals that represent the EELS spectra. This is powerful tool to distinguish allotropes of carbon.

2.2.10 Raman Spectroscopy

Raman spectroscopy is a surface sensitive technique to explore the chemical bonding and defects in carbon nanostructure, oxides, semiconductors, polymer, liquids and bio-materials. Raman is a fast characterization and nondestructive technique. It offers mapping at micro-scale regions. Post processing of data with fittings are used to find the variations of peak position and FWHM. Raman is very useful to distinguish the localized behaviors in polymers [11] and carbon based compositions [12-14]. The instrument is calibrated with silicon substrate every time before data collection. Silicon has a characteristic Raman shift at 520.7 cm^{-1}. During our experiments, we have used LabRAM Aramis Horiba Jobin Yvon Confocal Raman Microscope as shown in Figure 12.

Table 2: Raman data acquisition parameter

Parameters	Values
Size of area scanned	20 μm × 20 μm
Laser wavelength	532 nm
Raman laser spot size	700 nm
Slit size	100 μm
Hole size	400 μm
Data average from each point	3
Time of acquisition for each point	0.4 s

During data acquisition using Raman, the parameters mentioned in Table 2 were set to get good signal to noise ratio, avoid damage to the sample and average the signals. There are options of using of lasers of different wavelengths. Filters are often used to reduce the intensity of the laser. If the signal is weak, generally the data

acquisition time is increased. Based on the samples, the inelastic scattering can be classified into two major categories: Stokes-Raman and Anti-stokes Raman.

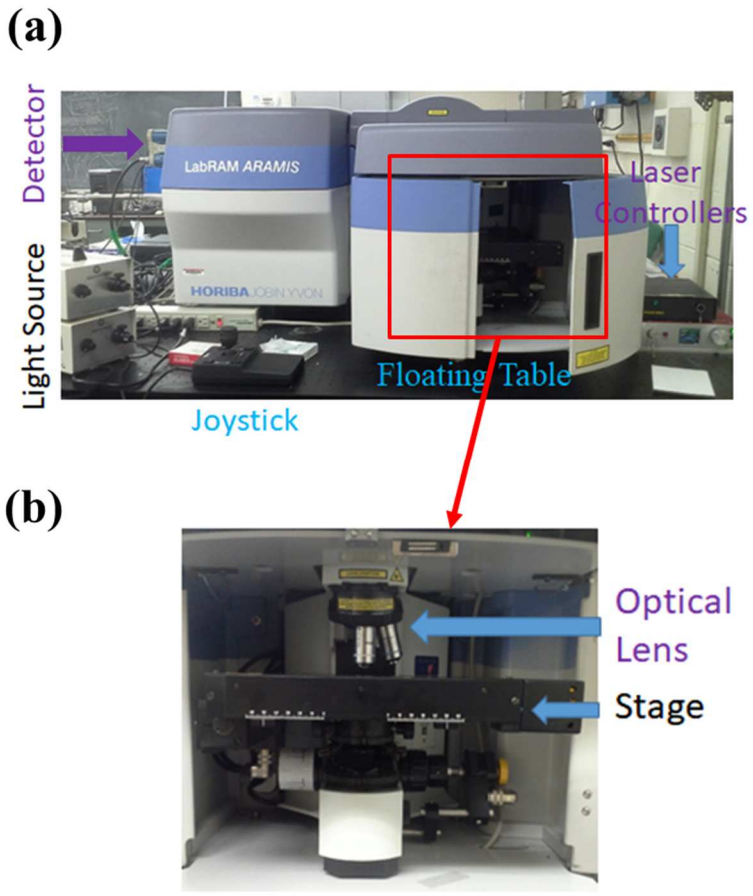

Figure 12: Setup for Raman measurement. (a) Raman from LabRAM ARAMIS setup at SAC, UMD. (b) Zoomed view of the sample stage and optical lens where samples come in close proximity to the lens.

Part I

Chapter 3: Introduction to Covetics

In this chapter, background of the importance of Al alloys and Ag metals, and the significance of the Covetic alloys will be focused. The process of making Covetic materials, and the observed superior properties for Al and Ag-Covetic systems are discussed. Relevant characterization techniques to identify the allotropes of carbon are briefly explained.

3.1 Original Metals & Limitation of Carbon Inclusion

3.1.1 Commercial Aluminum

Aluminum (Al) is one of the most widely used elements in modern civilization. Because of high reactivity with the atmosphere and many other elements, Al is generally used in alloy forms to reduce oxidation. Al alloys are very useful in lightweight structures because of their low density, high strength and ductility. Based on the processing conditions and heat treatments, Al is categorized in many different ASME grades. Al alloys have good thermal and electrical conductivities apart from their structural uses. That makes Al useful in power-grid lines and heat sink connectors. In everyday life, Al is used in kitchen pots and building constructions. The low melting point (660 ^{o}C) makes Al easy to forge. In addition, machining of Al is relatively easy, making it a great choice for the auto and aircrafts industries. There are two major types of Al alloys sold in the market. One class is known as the wrought Al as listed in Table 3 [15] and the other one is cast Al. Some of these alloys are heat treatable [16].

Table 3: The wrought Al-alloy designation codes

Al-Series	Dominant doping elements	Uses
1xxx	Iron and Silicon (<1% in total)	Very pure forms are used in chemical and electrical components, rivets
2xxx	Copper	Widely used in aircraft
3xxx	Manganese	Heat exchangers in vehicles and power plants, and kitchen utensils
4xxx	Silicon	Fusion welding and brazing
5xxx	Magnesium	Shipbuilding, pressure vessels, bridges, buildings, and transportation
6xxx	Magnesium and Silicon	Welding fabrication industry, extrusions, structural components, naval ships, power grids, and nuclear plants
7xxx	Zinc	Aircraft and competitive sporting equipment
8xxx	Other Elements like lithium	

In this thesis, Al-6061 and Al-7075 Covetic alloys were studied. The exact composition of these two alloys are listed below:

Table 4: Elemental composition list of Al-6061 and Al-7075

Element	Al-6061	Al-7075
Cr	0.04-0.45	0.18-0.28
Cu	0.15-0.4	1.2-2
Fe	0.7	0.5
Mg	0.8-1.2	2.1-2.9
Mn	0.15	0.3
Si	0.4-0.8	0.4
Ti	0.15	0.2
Zn	0.25	5.1-6.1
Al	Bal.	Bal.

From the table, it is obvious that Al-6061 has dopant metals below 4% of total atomic compositions whereas for the Al-7075, the doping is ~10%. Al-6061 is widely used in naval ship, bi-cycles, auto-industry, aviation parts, and nuclear power plants. Al-7075 alloys possess a strength comparable to many steels, and have been used in many planes. The original alloys have been designed to have good fatigue strength and

average machinability. Such properties are particularly important in the naval, automotive and aviation industry. However, these two alloys need to be improved because of the failures, corrosion, and limited lifetimes based on different operating conditions such as humidity, heat, sea water and corrosive environment. With the development of modern nanotechnology there have been many attempts to modify such traditional metal alloys to enhance the properties. One idea is to incorporate carbon nanostructure in these alloys.

3.1.2 Silver

Silver (Ag) is one of the most noble metals throughout the history. In ancient times and medieval periods, Ag was used in coins along with gold. Many luxurious products are made of Ag for decorative purposes, and the jewelry industry widely uses Ag. Ag nanoparticles are used as catalysts in chemical process [17] and microbiological applications [18].

In case of Ag, the practical use is limited due to its high cost and the fact that it tarnishes even under normal atmospheric conditions. Such limitations are the barriers to utilize its highest electrical conductivity (6.3×10^{-7} S m^{-1}) and thermal conductivity (420 W $m^{-1}K^{-1}$) in pure form in electronic industry. Therefore, anti-corrosion properties can help it to be applied in broader fields of applications specially electronics.

3.1.3 Carbon Nanostructure in Al & Ag

Since the discovery of graphene in 2004, a 2-dimensional form of carbon with the highest strength, electrical conductivity, elasticity, stretching and many other amazing properties [19], both academia and industry have strived to find ways to incorporate low dimensional carbons in metals [20, 21]. However, there are significant

challenges for such inclusion of carbon especially in bulk metals. Theoretical studies under equilibrium conditions limit the solubility of carbon in many metals such as copper (Cu), gold (Au) and Ag [22]. In bulk case, only 0.04% carbon is soluble in Ag as shown in Figure 13 [23]. Although there are some reports of embedding graphene in such metals such as Cu [24] and Ag [25], those were not in bulk, and only limited to thin films and in laboratory scale. Al forms a secondary phase of Al_4C_3 as shown in Figure 14. Al_4C_3 does not have sp^2 bonding. Therefore, investigations into the role of sp^2 carbon in these metals by traditional metallurgical methods had long been prevented.

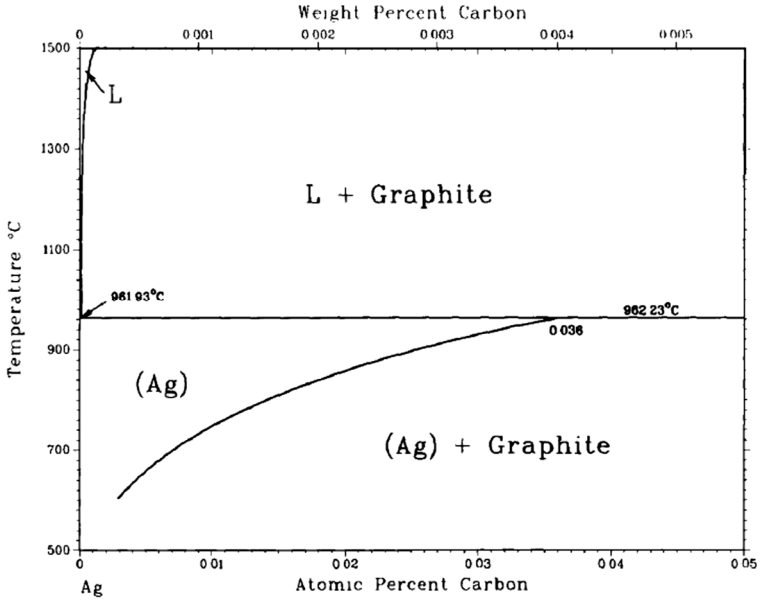

Figure 13: The Ag-C phase diagram showing the limited solubility of carbon up to 0.04% [23].

Recently, many modern processing techniques are seen in place of conventional ones to embed carbon networks into the Al-matrix with CNT and graphene by ball milling [26, 27], chemical vapor deposition (CVD) [28], friction stir [29], cold spraying [30] and plasma spraying [31, 32]. Cold spraying, plasma spraying and

friction stir using CNT produced Al_4C_3 phases to get improved mechanical properties such as higher elastic strength, Young's modulus and hardness. However, many of these metal processing techniques require multiple steps creating complexity and extra costs. Furthermore, the transformation of carbon into Al_4C_3 compromises high electrical and thermal conductivity possible by sp^2 carbon network. In case of ball milling, the drawbacks are high ball milling time, presence of high density defects, and producing mostly sp^3 carbon [26, 33]. Besides, CVD is not suitable for large scale production. Many of these techniques create weak bonding by van-der-Waals forces between carbon and metals. Therefore, a single step process involving strong bonding between the metal and carbon with enhanced mechanical and electro-thermal properties by maintaining high percentage of sp^2 bonding is an attractive goal for the industry which brings the focus on Covetic materials.

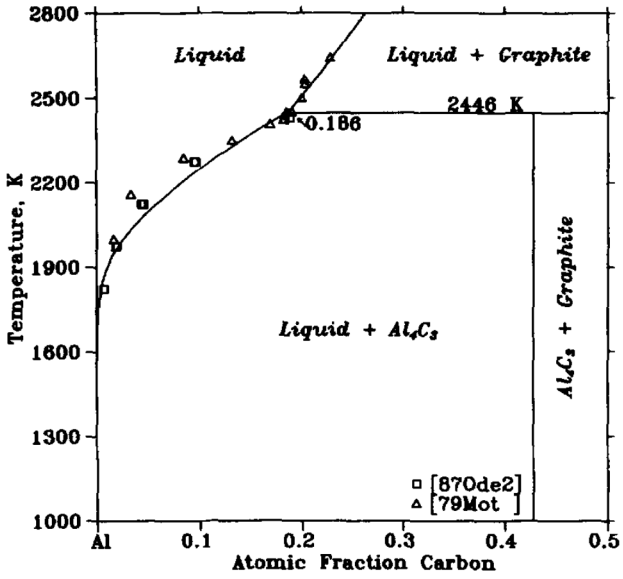

Figure 14: The Al-C phase diagram showing the limitation of solubility of carbon [34] comparing with experimental data [35].

3.2 Metal-Covetic

3.2.1 Covetic Process

Covetic process is unique in terms of fabrication methods. In the Covetic process, by applying external high current to a mixture of the molten metal and particles of activated carbon of 20-50 μm sizes, non-equilibrium conditions are created (Figure 15). Afterwards, the mixture is slowly cooled down to room temperature. The whole process is completed in an argon gas environment to prevent oxidation (Figure 15). It is assumed that such conditions create electro-charged carbon ions and a plasma like phenomenon which facilitates to embed carbon polymers in the metals. Third Millennium Materials, LLC (Ohio, USA) developed this process and incorporated carbon in different metals and their alloys including Al, Cu, Au, Ag, Zn, Sn, Pb and Fe. Previously, in the case of Ag and Cu-Covetic alloys and their thin films, much better mechanical, electrical and optical properties have been reported due to the presence of sp^2 carbon [36-38]. In this dissertation, Al-6061, Al-7075 and Ag-Covetic samples were characterized at nano-scale by various microscopic and surface analytical techniques. The Covetic samples were named according to the nominal carbon weight percentage mixed in the molten state. For example, if Al-6061 was mixed with 3% carbon, the sample is identified as Al-6061 cv-3%, where cv stands for Covetic. Similarly, Al-7075 cv-3 and 5%, with 3 and 5 wt%, respectively, and Ag cv-6% (with 6 wt% C) were studied, and the results were compared to the parent material.

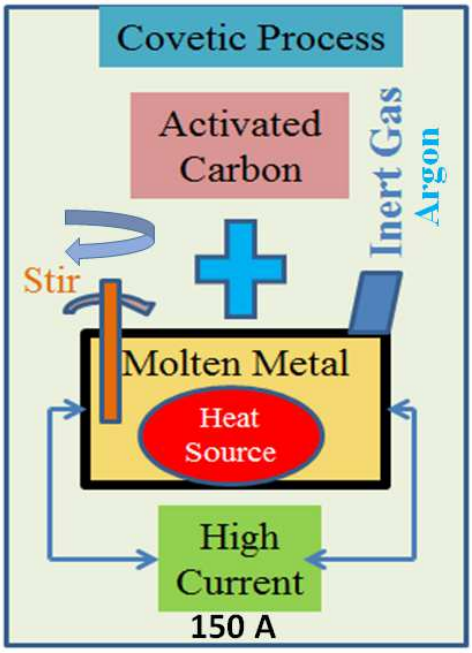

Figure 15: Covetic process diagram

3.2.2 Improved Properties of Al & Ag-Covetic

Both the Al-6061 and Al-7075 Covetic samples have shown significant improvements in terms of mechanical and electrical properties compared to their original alloys. Al-6061 cv-3% showed 30% higher ultimate tensile strength (UTS) and 23% higher hardness as shown in Figure 16 and Figure 17, respectively. The electrical conductivity improved by 42%. Less corrosion was also reported in Al-Covetic [39]. Comparable UTS results were also recorded for the Al-7075 Covetic alloys with different carbon doping levels of 3 and 5% (Figure 18). UTS increased over 30% for Al-7075 cv-5% compared to pure Al-7075.

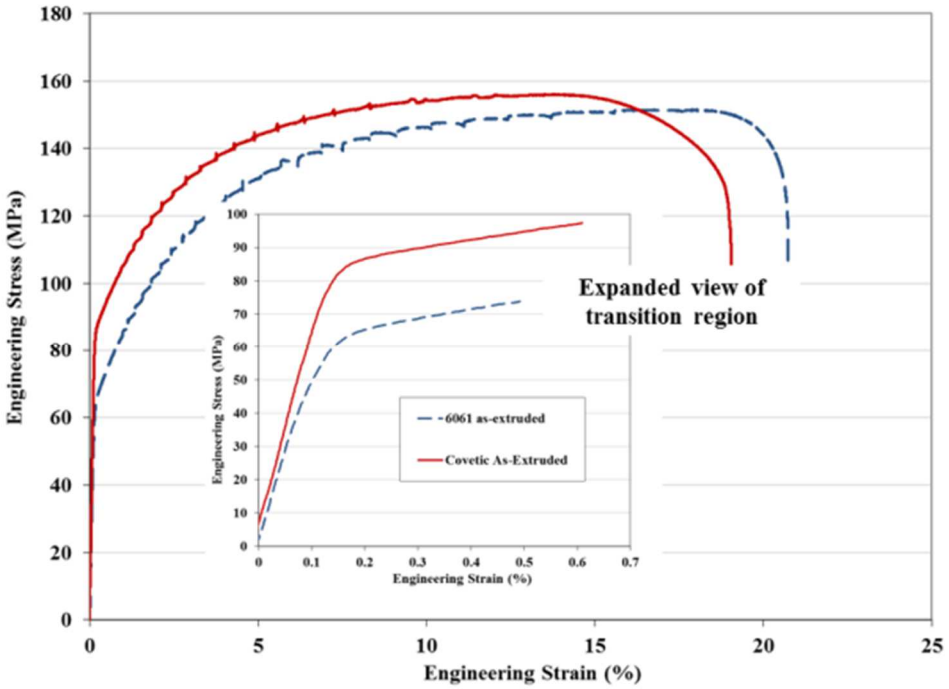

Figure 16: Increased tensile strength of Al-6061 cv-3% compared to pure Al-6061 [39]

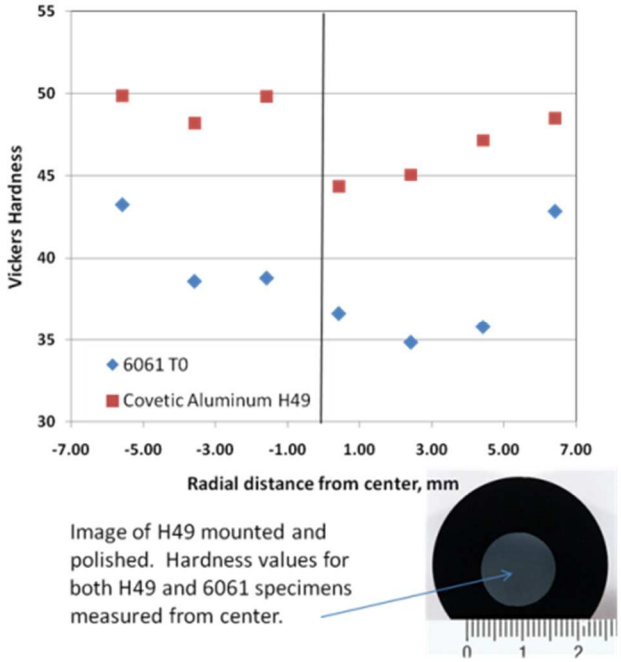

Figure 17: Improved Vickers micro-indentation hardness of Al-6061 cv-3% (■) compared to reference sample (♦) [39].

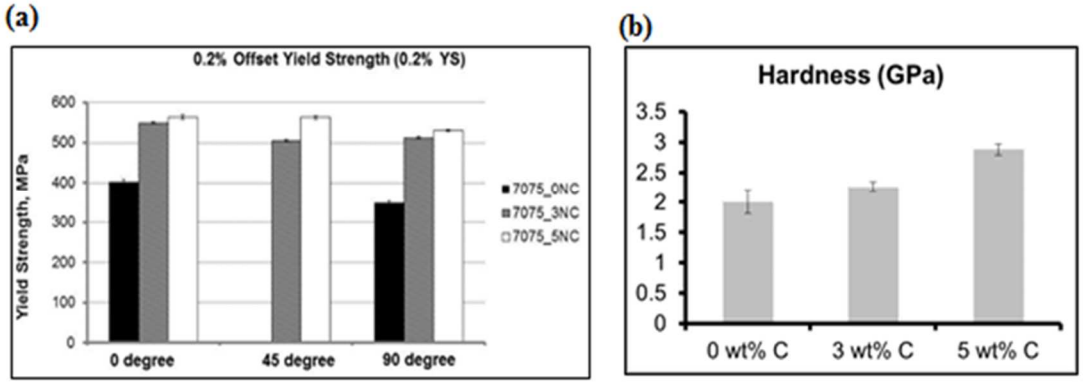

Figure 18: (a) Yield strength, and (b) Hardness of the pure Al-7075, Al-7075 cv-3%, and Al-7075 cv-5% [13].

Such enhancements give the strategic advantage of building lightweight ships and planes of superior agility with less fuel consumption, and reduces the cost in building. It also increases the flying range or navigating areas without the need for more fuel. Moreover, less corrosion might increase the vessel lifetime which will require less maintenance and replacements. In addition, the higher electrical conductivity can be utilized in the power grids where sagging of the lines due to self-weight is a problem and costs more in constructions.

In the case of Cu-Covetic, less oxidation was observed on the surface [36, 37]. Similarly, reduction in tarnishing of Ag-Covetic can result into longer life time in electronics and jewelry industry. However, the way the Covetic process gives rise to such enhanced properties in different metallic systems is not clearly understood. Here, in this thesis, these concerns are addressed by demonstrating the role of the carbon nanostructure embedded in the Covetic process.

3.3 Carbon Nanostructure Characterization

3.3.1 Raman Analysis of Carbon Nanostructure

In the case of carbon nanostructure, Raman plays a vital role to determine the specific carbon structures such as graphene, carbon nanotube, fullerene, diamond and other allotropes. Graphite carbon has two main characteristic peaks known as G-peak at ~1585 cm^{-1} and D- peak at ~1350 cm^{-1}. The G-peak is due to the single photon emission process known as first order Raman scattering due to tangential stretching mode of the graphite plane [40]. The G-peak position varies based on several factors including strain, intercalation of dopants and substrate interaction. D-peak position is related to the defects, and gives information on whether sp^2, sp^3 or mixed bonding are present. For a single layer graphene, a very sharp 2D peak at high wavenumbers of around 2700 cm^{-1} is observed while the D-peak intensity appears very low except at the edges of the graphene layer. This is the easiest way to determine if single layer graphene is obtained. Characteristic peaks of other forms of carbon are given in Table 5.

In-plane crystallite dimensions (L_a) of the graphitic regions are measured by using the integrated ratios under the G and D-peaks with the following equation:

$$L_a \text{ (nm)} = (2.4 \times 10^{-10})\, \lambda^4_{laser}\, (I_G/I_D)$$

Table 5: Raman modes of carbon nanostructure

Peak Location (cm^{-1})	Mode	Description
1585	G-peak	Doubly degenerate in-plane transverse optical phonon mode and longitudinal optical phonon mode (iTO and LO) at the Γ point [41]

1355	D-peak: sp^2	Inter-valley double resonance process from defects and iTO phonon
1331	D-peak: sp^3	Diamond peak
1740	M-band	C=O
1640		O-H
1851	iTALO	Combine modes of transverse acoustic and longitudinal optical modes
1955	iTOLA /LOLA	Combine modes of transverse optical and longitudinal acoustic modes
3250	2D′	the second order of the intra-valley $D^{/}$ peak
2960	D+D′	Sp^2 CH_x stretching mode
2765	2D	Due to crystalline Graphite. An inter-valley double resonance process involving two iTO phonons near the K points[1]

It is important to note that such modes listed in Table 5 [42] are basically for pure carbon based materials. Some higher wavenumber peaks might not appear due to interactions with substrates. The relative presence of sp^2 and sp^3 bonding can be determined by Raman. The quality or defect concentration of the nanostructure carbon can also be quantified by taking integrated area ratios under the characteristic peaks.

3.3.2 EELS Analysis of Carbon Nanostructure

EELS analysis of carbon nanostructure is very useful to distinguish different allotropes. By C-K edge spectrum, it is possible to identify sp^2, sp^3 and amorphous carbon. For sp^2 carbon, a sharp peak appears at 284 eV that corresponds to transitions of the 1s electron in graphite to the π^* antibonding unoccupied state [43, 44]. The ideal sp^3 signal comes from transition from the 1s occupied state to the σ^* antibonding unoccupied state at 290 eV in diamond and graphite. In the same materials, these allotropes might co-exist based on the localized behavior of the growth and materials kinetics. The volume fraction of these different bonding can be determined by peak fitting the data. A few examples of EELS variations are shown in Figure 19. In the case

of multiple signals overlapping in small areas, principal component analysis (PCA) based data processing can remap the area based on the dominant individual signals. In the Al and Ag-Covetic samples, sp^2 and amorphous enriched regions were distinguished by such a technique.

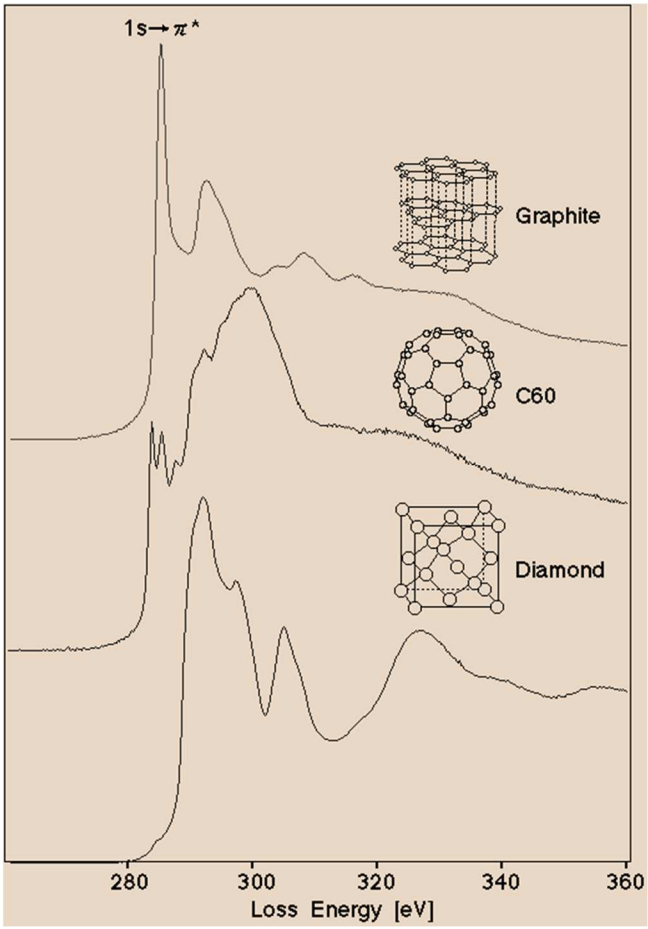

Figure 19: C-K edge of C 1s of different allotropes [45].

3.3.3 XPS Analysis of Carbon Nanostructure

XPS is helpful to find the specific type of bonding of carbon (sp^2/sp^3), and whether other elements are bonded with carbon. The positon of the binding energy can distinguish such features. The shape of the C 1s in HR XPS also indicates the electronic properties due to different density of states (DOS) near the Fermi level. The high

asymmetry of the C 1s spectrum is often related to sp^2 nature and the symmetric broad nature corresponds to sp^3 carbon (Figure 20). Generally, when the metal-carbon bonding is present a peak appears at ~282-283 eV [46].

The oxide states such as C-O, C=O and C-O-O-H are found at higher binding energy from 284 eV (Figure 21). Increasing bonding features gradually shift the peak positions to higher energies up to 290 eV. For highly conductive carbon samples, satellite peaks are observed above these energies. Moreover, if there is any indication of the oxidation of the carbon nanostructure, the type of bonding can be verified from the O 1s signal too.

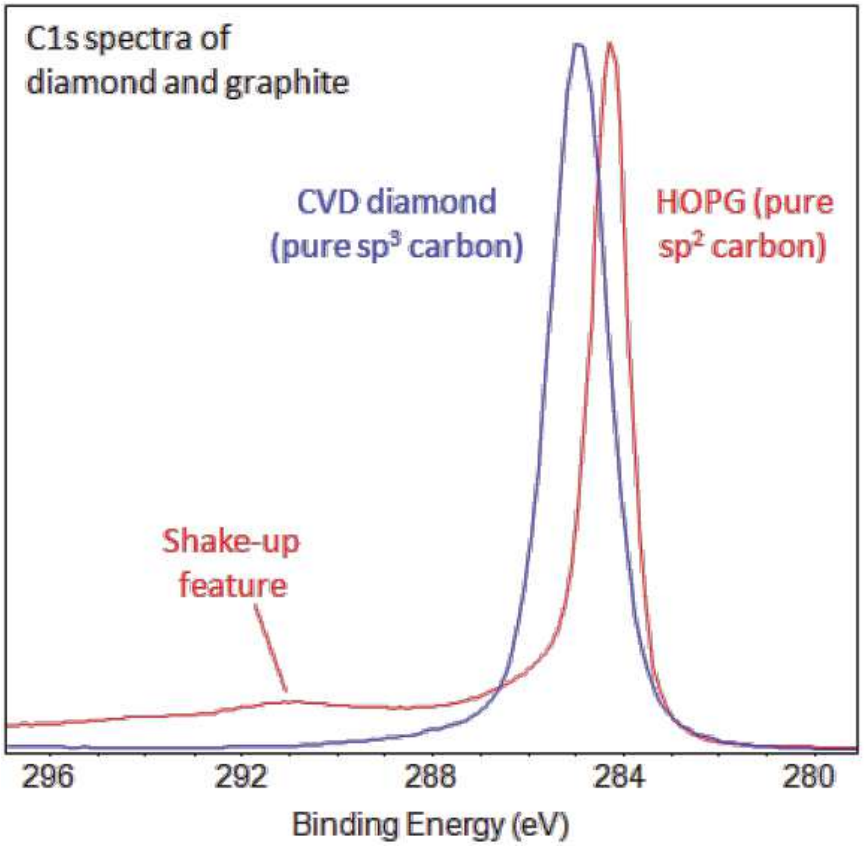

Figure 20: C 1s spectrum of diamond and graphite [46].

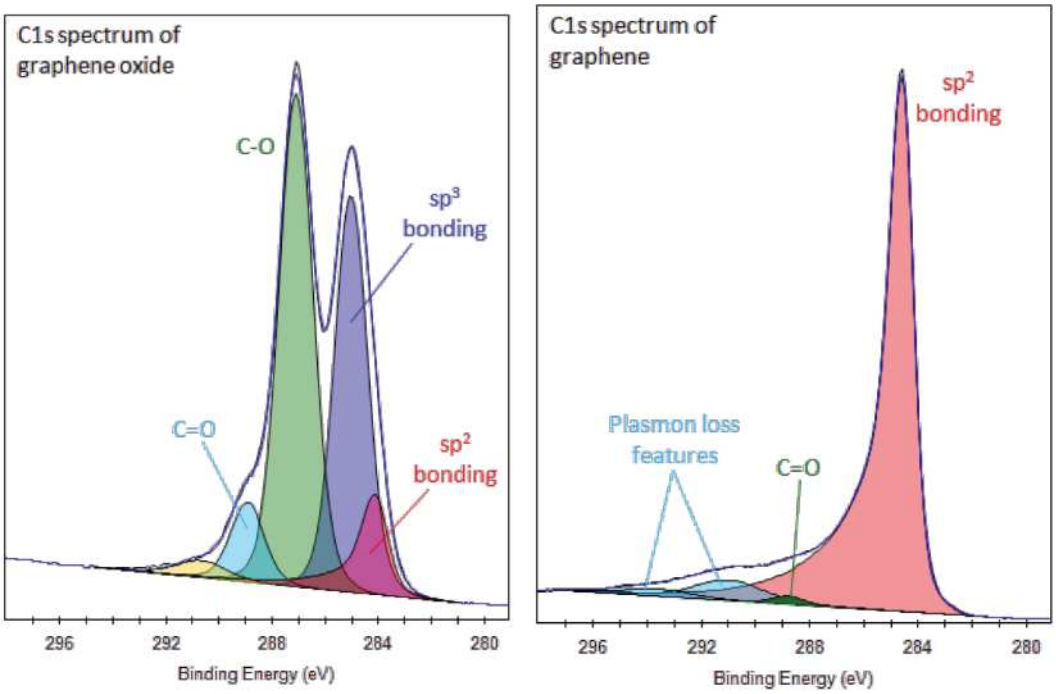

Figure 21: C 1s spectrum of (a) graphene oxide and (b) graphene [46].

3.3.4 KPFM of Carbon Nanostructure

KPFM is especially useful for carbon nanostructure embedded in the metal matrix. The electrostatic potential difference of carbon is much lower compared to the host metals. Therefore, by potential and current mapping, the distribution of the carbon nanostructure can be visualized. These maps are correlated with the typical AFM height and phase images.

Chapter 4: Characterization of Al-Covetic

The structure, bonding, surface chemistry and dispersion of carbon in the Al-Covetic samples are detailed in this chapter. Networks of graphene nanoribbons (GNR) with 3D epitaxy and preferred orientation along the ⟨110⟩ and ⟨112⟩ directions of Al (111) crystal planes were observed by TEM and EELS mapping. XPS and Raman mapping also found sp^2 carbon in Al-6061-Covetic, and hybrid sp^2-sp^3 in Al-7075-Covetic systems. KPFM supported the presence of GNR in the Al metal matrix. Overall, crystalline sp^2 GNR were detected which might have enhanced the mechanical and electrical properties of the Al-Covetic samples.

4.1 Sample Preparation

Small pieces of the Covetic and pure metal samples were cut, and polished with alumina paper starting from 12 μm, followed by 9, 6, 3, 1 and 0.3 μm particle sizes to get smooth surfaces from their original rough texture. The polished samples were sonicated in acetone and isopropanol to remove hydrocarbons and residue from the polishing paper. To keep consistency of different experiments, the same samples were characterized by Raman, KPFM and XPS. Similarly, TEM lamellas were prepared by mechanical polishing with diamond lapping paper with decreasing particle size from 9 to 3 μm until the thickness was ~15 μm. These samples were ion milled at low angle using Ar^+ ions at an angle of 15° with a voltage of 3 KV and current of 3 mA to reduce thickness and clean the surface.

4.2 Presence of Crystalline sp^2 GNR in Al-Covetic

4.2.1 TEM & EELS of Al-Covetic Samples

One of the major findings of the Al-Covetic materials is to observe the presence of crystalline GNR of varying widths along metal crystalline directions. Using high angle annular dark field (HAADF) in TEM in Figure 22 (a), folded ribbon-like structures were observed in Al-6061 cv-3%. These structures appeared similar to graphene nanoribbons and nanosheets [47, 48]. To confirm the elemental distributions, EDS maps were acquired for the Al, C, O, and alloying elements such as Mg and Si. In the folded regions as indicated by the arrows, high concentrations of oxygen and carbon were observed in Figure 22 (b) and (c), respectively. The alloying elements were dispersed randomly throughout the sample. To ensure the observed results, multiple maps were carried out along the folded regions, and similar results were observed. The dark regions in the vicinity of the ribbons were found to be the secondary phases such as Mg_2Si and CuO. However, it is not possible to image individual ribbons due to the resolution limit of EDS originating from the interaction volume compared to the spot size.

To find the crystalline nature of the carbon, multiple SADPs were taken at the carbon enriched regions in the BF TEM image (Figure 23 (b)). 3D epitaxy of carbon in Al was observed from the diffraction pattern in Figure 23 (a) from the left region of Figure 23 (b). In SADP (Figure 23 (a)), weak spots as marked by 1 and 2 were seen on Al (111) plane. The hexagonal bright spots originated from Al (111), and were confirmed by measuring the inter-planar distances between the spots. The inter-planar distance between the weak spots was 0.205 nm. This value did not correspond to Al

or Al_4C_3, rather, it was very close to the <10$\bar{1}$0> inter-planar distance of 0.2127 nm in the basal plane of graphite with ~3.3% compressive strain of the graphitic region. Such strain might be induced from the lattice mismatch between the Al-metal and graphite.

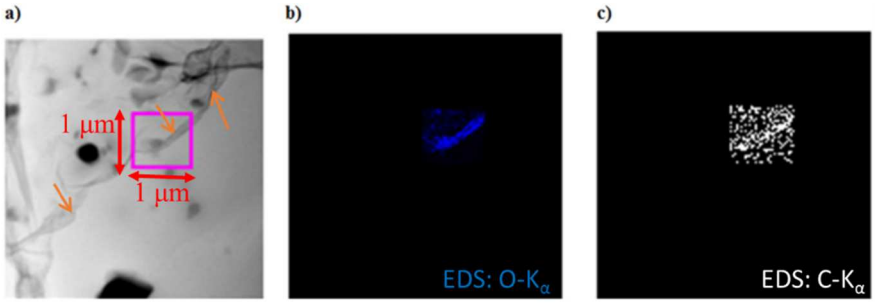

Figure 22: STEM images: (a) High angle annular dark field (HAADF) image of folded ribbon-like regions (arrows) in Al-6061 cv-3%. EDS maps of (b) O-K_α and (c) C-K_α [49].

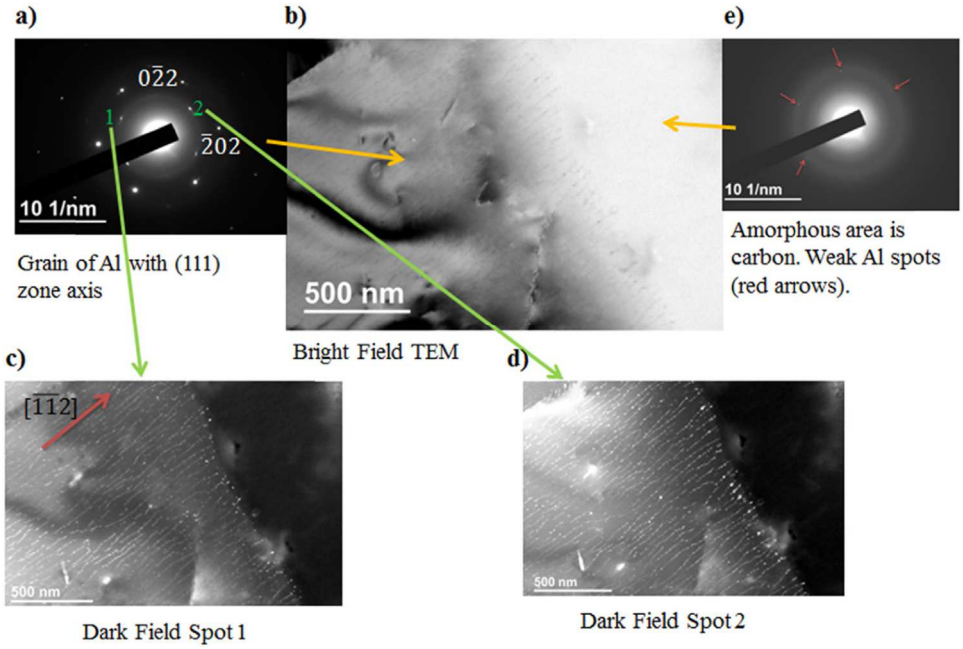

Figure 23: TEM images and selected area diffraction patterns of Al-6061. (a) (111) electron diffraction pattern of Al-6061 cv-3% from the left region in (b). The hexagonal bright spots correspond to the Al ⟨220⟩ spots. The weak spots, labeled 1 and 2, in the

inner circle are due to the <10$\bar{1}$0> reflections on the (0001) plane of crystalline graphite. (b) Bright field TEM image of the sample. (c) and (d) dark field TEM images using weak spots 1 and 2 in a), respectively. (e) Diffraction pattern from the upper right area in (b) showing a broad ring corresponding to amorphous carbon [49].

To further clarify the observed SADP in Figure 23 (a), the schematic in Figure 24 is shown where carbon atoms are epitaxially embedded in Al (111) plane. There is a 13% mismatch between Al low potential sites and C-C distance in graphene.

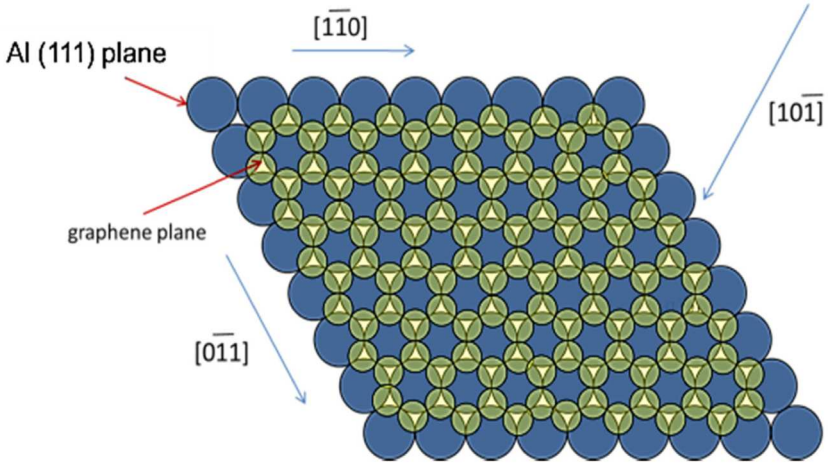

Figure 24: Schematic of epitaxy of C in Al. Schematic showing the epitaxial relation between graphite and the (111) plane of Al corresponding to the pattern observed in Figure 23 (a) [49].

By using the weak spots labeled 1 and 2 of graphite in Figure 23 (a), DF images were taken as shown in Figure 23 (c) and (d). In these images, small crystalline graphite regions were seen to be aligned along a preferred <$\bar{1}\bar{1}$2> direction in the Al-lattice. Interestingly, these ribbon like features originated from the interface between the Al-grain and a region of amorphous carbon identified by SADP in the Figure 23 (e) and indicate that the application of the current in the Covetics process turns amorphous

carbon into crystalline carbon. Furthermore, the GNR spread out in the preferred crystalline directions from the source carbon in the Covetic process. To confirm the nature of the bonding of these GNRs, EELS mappings were carried out in multiple regions in Figure 25 and Figure 27. In the both DF images, ribbon structures of 20-40 nm widths appeared with high carbon concentration. In HAADF images, the lighter element carbon (atomic mass: 12.011) appears dark in comparison to the heavier element Al (atomic mass: 26.98) due to less scattering of electrons. Such contrast was helpful to distinguish the nano-scale features of carbon distribution. After background subtraction, the C-K edge profile clearly showed sharp 1s to π^* transition at 284 eV indicating the presence of sp^2 carbon (Figure 26 (a) and Figure 27 (e)) which differed from the source carbon signal showing amorphous nature in Figure 26 (b). Therefore, it is convincing to assume that in the Covetic process when the high current was applied, carbon atoms from the activated carbon particles became ionized, bonds were created to between the carbon ions forming chains, and further distributed the formed layers along preferential directions of the host Al-metal after cooling down. The coefficient of thermal expansion of the graphene is negative while all the metals including Al have positive values. Therefore, during the cooling and solidification, such opposite behavior can result in the compressive strain in the graphene nanoribbons.

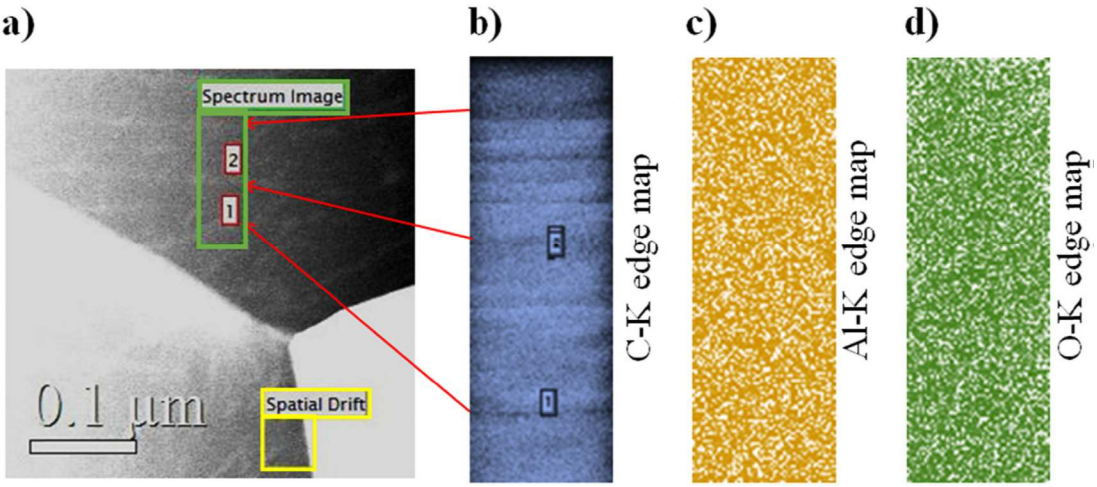

Figure 25: EELS mapping of GNR. (a) HAADF image of Al-6061 cv-3% TEM sample. EELS spectrum image was acquired from the green rectangle region labeled as Spectrum Image. The yellow rectangle labeled Spatial Drift was used to correct for any drift of the sample during the data acquisition. (b) False color map of the C-K edge showing preferential distribution of carbon in ribbon geometry. The bright regions have higher concentration of carbon compared to the dark regions. The dark regions in (a) appear whitish in the C-K edge profile for carbon enriched regions. False color maps of the (c) Al-K edge and (d) O-K edge where both Al and O present uniform distribution [49].

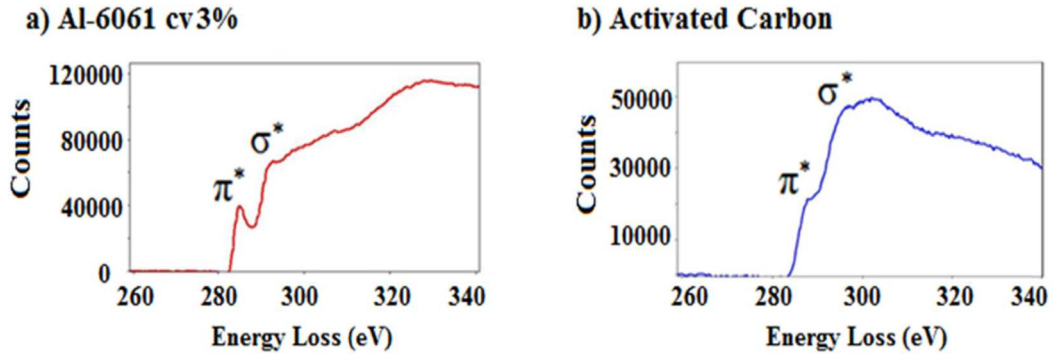

Figure 26: EELS spectra of Carbon. C-K edge profile after background subtraction presenting the sp^2 character of a) Al-6061 cv-3% and b) the activated carbon used as source [49].

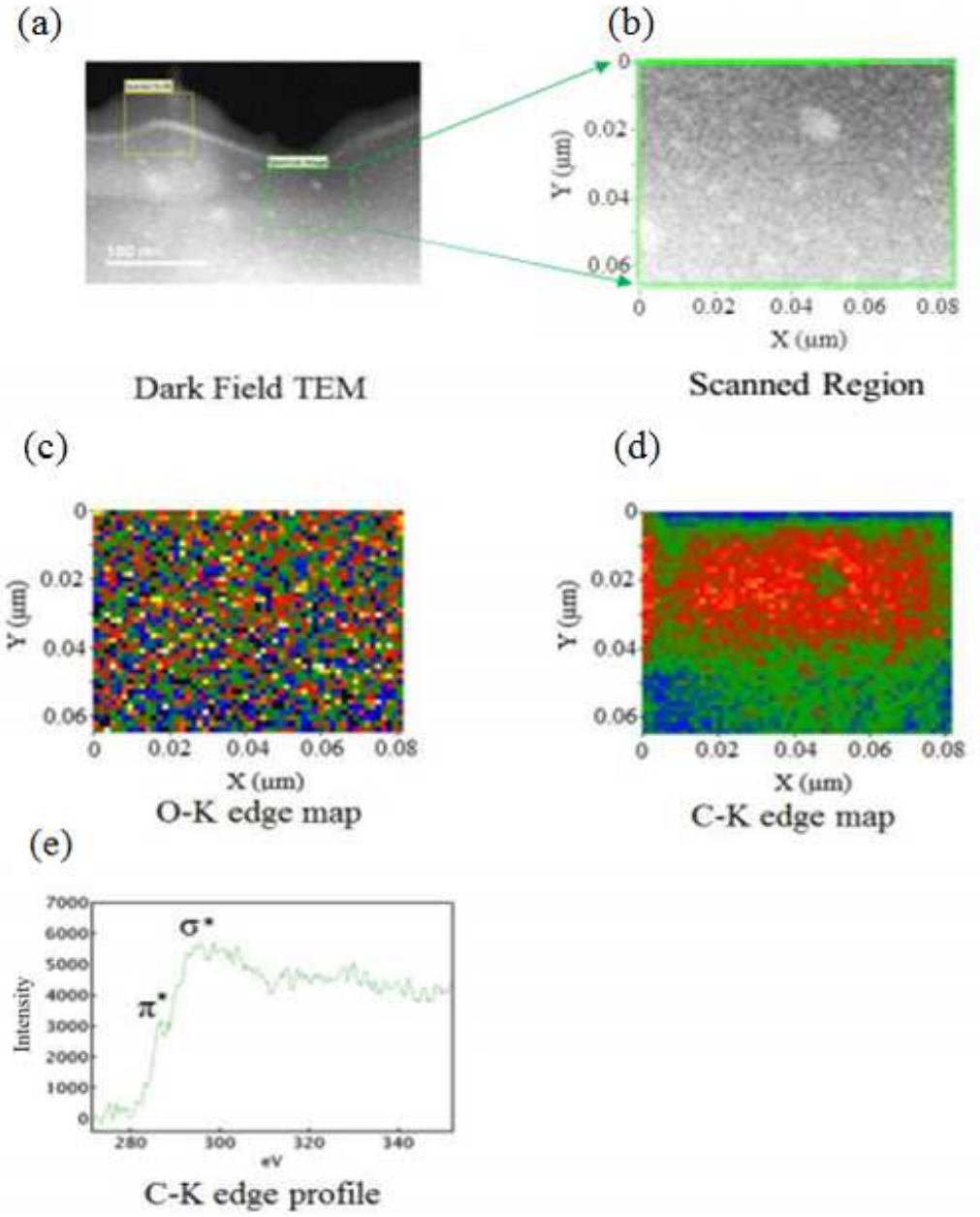

Figure 27: (a) HAADF image of Al-6061 cv-3%. The green rectangular area labeled Spectrum Image delineates the region selected to acquire EELS spectrum imaging in the energy range for the C-K edge. (b) Magnified area of the green rectangle in (a). (c) O-K edge map. (d) C-K edge area map of the scanned region showing a ribbon type feature (e) C-K edge profile after background subtraction from one of the points in the scanned region showing sp^2 attributes [50].

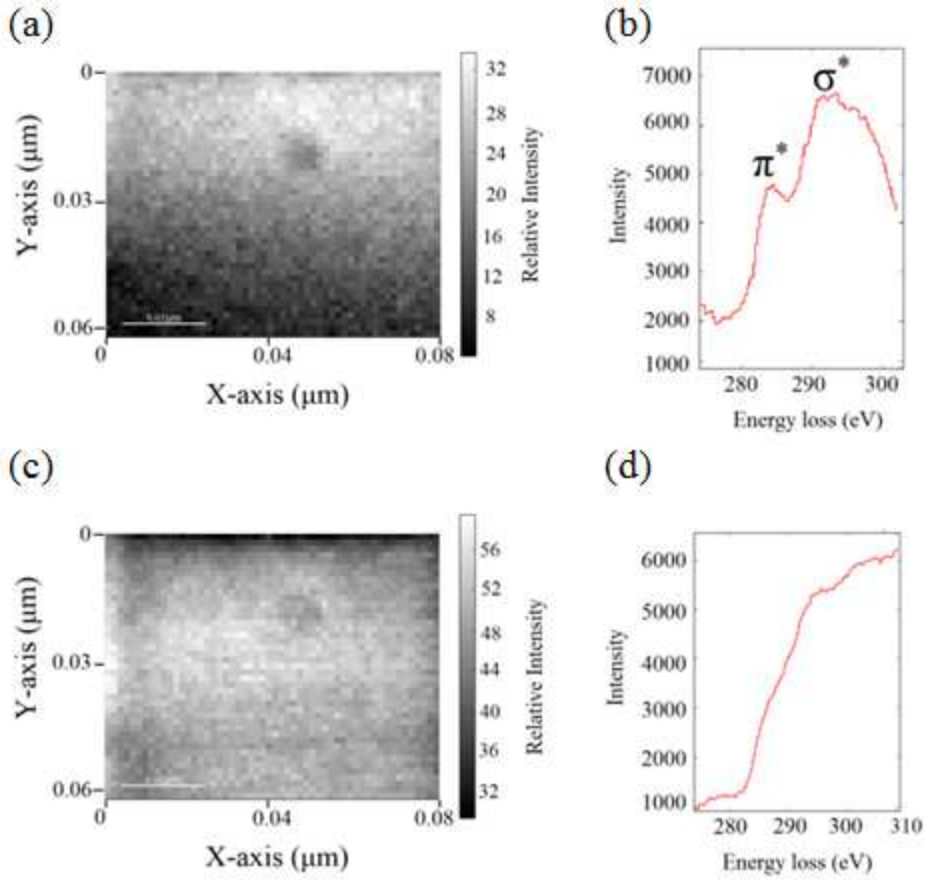

Figure 28: Spectral decomposition of the EELS mapping shown in Figure 27 by BSS. The first two primary signals and their corresponding maps are shown in the two sets. (a) Map of the first signal corresponding to sp^2 carbon (b) showing regions of higher intensity in ribbon form (whitish region). (c) Map of the second component in the BSS analysis showing similar signal to amorphous carbon (d) [50].

In some cases, sp^3 carbon signal was also observed in carbon enriched region. To find the distribution of the individual allotropes, blind source separation (BSS) algorithm was applied using HyperSpy 8.0 program to deconvolute the EELS image shown in Figure 27 (d). The program at first finds the dominant signals, and based on that remaps the EELS plot showing the relative intensity of the individual signals. In this Al-Covetic sample, the dominant signal was sp^2, and it was remapped in Figure 28

(a). The second dominant signal was sp^3 remapped in Figure 28 (c). The bright regions indicate high concentration of the allotropes. By comparing these images it is observed that sp^2 carbon content was much higher in the ribbon like regions. The sp^3 carbon did not show any such preferential pattern. It is possible that sp^2 GNRs are terminated by the sp^3 carbon from the source or the environment.

4.2.2 XPS of Al-Covetic Samples

XPS of the pure Al alloys and Al-Covetic samples were carried out to detail the bonding of the carbon and oxidation states. Elemental quantification from the surface and Ar-sputtered levels showed the percentage of carbon in the alloys was smaller than their nominal values. Figure 29 shows the atomic concentrations of Al, C and O vs. sputtering time in Al-6061 cv-3%.

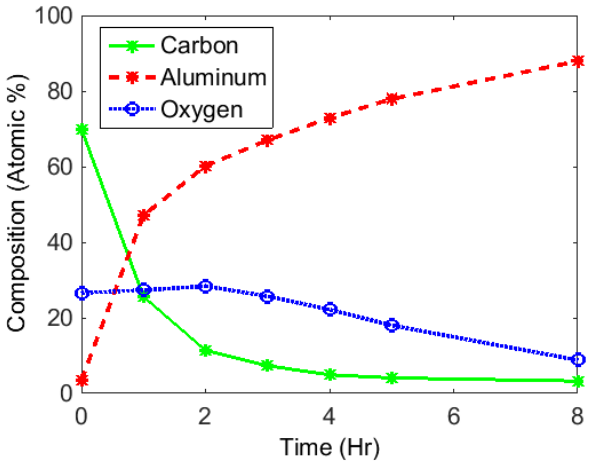

Figure 29: XPS depth profile of the Al-6061 cv-3%. Atomic percentage of the Al, C and O depth profile is plotted as a function of sputtering time. On the surface, high percentage of carbon was observed due to hydrocarbon contamination. Ar-sputtering of the samples for extended period gave stable values of around 3 at. % carbon.

In the first scan of the samples, due to hydrocarbon contaminants accumulated on the surface, large amount of sp^3 carbon was observed. The percentages of the carbon

decrease with increasing sputtering time becoming stable at around 3 at.% after 8 hour sputtering in Al-6061 cv-3%, while in the Al-7075 cv-3% and cv-5% the concentration was around 1.5 at.%. The pure Al-6061 and Al-7075 did not show any presence of carbon after the hydrocarbon contamination from the surface was removed. After sputtering for 1 hour, the HR XPS spectra of C 1s of Al-6061 cv-3% showed an asymmetric peak with a tail towards higher binding energy shown in Figure 30 (b). Such asymmetry is a signature of the sp^2 bonding. Analysis of the C 1s peak in Al-6061 cv-3% sample indicated that around 3 % of the carbon created Al-C bonding giving rise to a peak centered at 282.7 eV [51].

In the Al-7075 Covetic samples along with the sp^2 bonding, the presence of sp^3, Al-C bonding and other oxides formed with carbon atoms were detected. This caused the broadening of the C 1s peak, and the maximum intensity appeared at 284 eV due to the mixed states of sp^2 and sp^3 (Figure 30 (a)). The noisy nature of the signal indicated lower C concentration, and made it difficult to peak fit to get the relative concentrations of the carbon allotropes. The broad tail at higher binding energies was the result of the presence of different oxidation states of the carbon most probably from the C-O, carbonyl groups (C=O) and carboxylic groups (C-O-O-H). These results were supported by the O 1s HR XPS. Two Gaussian peaks fit the O 1s experimental data with binding energies corresponding to C=O at 532.3 eV and C-O at 533.3 eV (Figure 31).

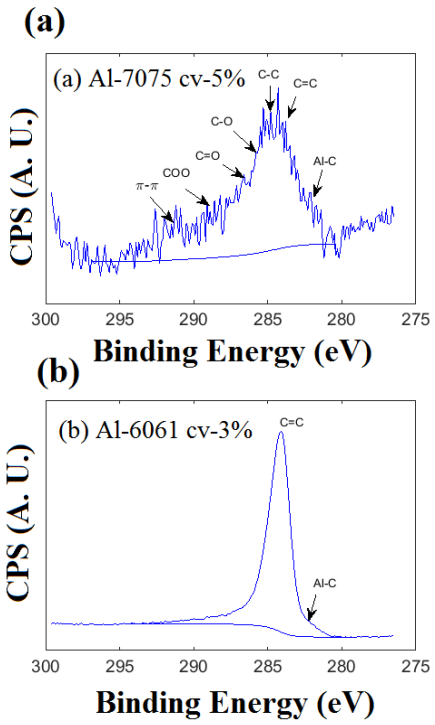

Figure 30: C 1s spectra after 1 hour sputtering of (a) Al-7075 cv-3% showing the presence of hybrid sp^2 and sp^3 bonding, the oxidized group and Al-C bonding. Al-7075 cv-5% also showed similar characteristics. (b) Al-6061 cv-3% had mostly sp^2 carbon presence with minor Al-C bonding at lower binding energy region [49].

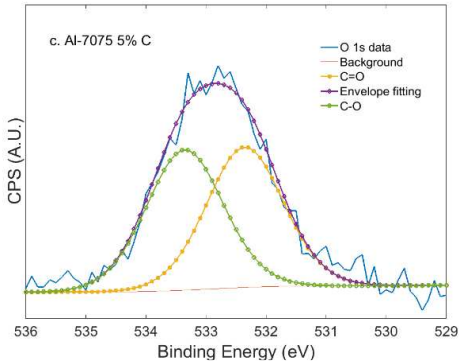

Figure 31: O 1s from the Al-7075 cv-5% sample clearly showing the presence of two different types of C-O bonding with a broad doublet in the data after 4 sputtering cycles. The data were fitted with C=O (532.3 eV) and C-O (533.3 eV) separated by 1 eV, and

the envelope fitting combines the contributions from these two components in good agreement with the experimental data.

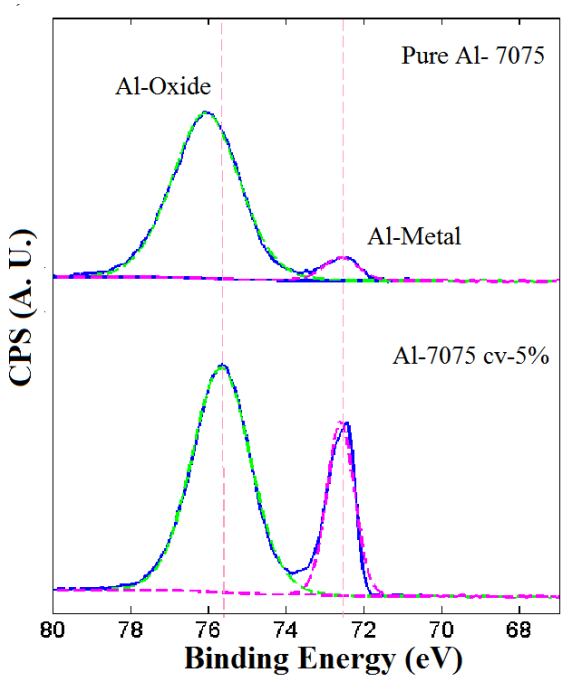

Figure 32: Al-2p XPS surface spectrum of pure Al-7075 (top) and Al-7075 cv-5% (bottom). Aluminum oxide (--) and Al-metal (--) are separately peak fitted with mixed Gaussian-Lorentzian- fittings to quantify the relative percentage of each.

Oxide thickness, an important parameter in corrosion studies, can be derived from the XPS data. In case of Al-7075 cv-5%, less oxidation on the surface was observed compared to the parent alloy (Figure 32). Al-6061 cv-3% also showed slightly less oxidation on the surface compared to the pure alloy without carbon. Aluminum oxide thickness (t) was estimated with the following formula:

$$t\ (nm) = 2.8\ \ln((1.4(I_o/I_m))+1) \qquad (7)$$

where, I_o and I_m are the peak area percentages of the oxide and metal photoelectron signal, respectively. The results are presented in Table 6 and show that the Al-7075 cv-5% sample with highest carbon content has the thinnest oxide layer.

Table 6: Thickness of oxides of Al-6061 and Al-7075 samples

Alloy	I_O (%)	I_M (%)	t (nm)
Al-6061	89.5	10.5	7.1
Al-6061 3% C	88	12	6.78
Al-7075	94.43	5.57	8.98
Al-7075 3% C	93.51	6.28	8.64
Al-7075 5% C	73.64	26.36	4.46

4.2.3. XRD of Al-Covetic Samples

In all of the Covetic and pure samples, XRD showed no carbon based phases such as Al_4C_3 or any allotrope of carbon. The sizes of GNRs and other nanostructures were too small to detect by XRD. Overall, the samples were polycrystalline in nature. Variations in the intensity of the (hkl) reflections indicated some preferred orientation of the grains of the Al samples. Secondary phases such as Fe-Si, Mg-Zn and Al_2CuMg_7 were present in Al-7075, and, Mg_2Si and Fe-Si were found in the Al-6061 samples.

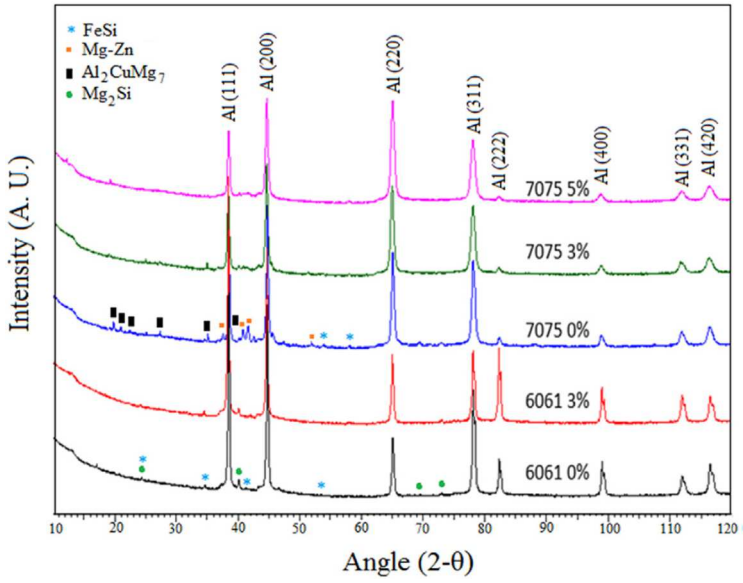

Figure 33 : XRD of pure Al-6061, Al-6061 cv-3%, pure Al-7075, Al-7075 cv-3 and cv-5%, respectively. Mg_2Si, and $Al_{71}Zn_{29}$ phases were observed in Al-7075, and $MgSi_2$, $Cu_{0.025}Zn_{0.975}$ and Fe-Si in Al-6061 FWHM of the Al-peaks varied with carbon content [49].

Table 7: Lattice parameter, grain size and strain of Al-Covetics calculated from the XRD.

Samples	Lattice Parameter (nm)	Crystallite Size (nm)	Strain (%)
Al-6061 (0% C)	0.405233(2)	146.1(8)	0
Al-6061 (3% C)	0.405121(2)	184.5(12)	-0.0276
Al-7075 (0% C)	0.405518(4)	107.4 (11)	0
Al-7075 (3 %C)	0.405461(7)	82.2(8)	-0.0141
Al-7075 (5 %C)	0.405281 (5)	67.1	-0.0584

Lattice parameter, grain size and strain were calculated from the XRD data (Table 7). The lattice parameter showed a gradual decrease with increasing carbon percentage suggesting the chemical bonding of carbon in the Al lattice is smaller than in the pure alloy, and compressive strain was observed in the Al lattice. The grain sizes

gradually decreased with carbon addition in Al-7075 series but not in the case of Al-6061.

4.2.4. Raman Mapping of Al-Covetic Samples

In the initial stage of the study, Raman spectra were collected at random spots of the Covetic and pure samples (Figure 34). The pure Al-6061 and Al-7075 did not show any signature of carbon. However, all of the Al-Covetic samples showed G and D-peaks of carbon with varying degrees of changes in peak position and FWHM from spot to spot. Therefore, Raman mappings were acquired for these Covetic samples to distinguish the variations of the G, D-peak positions, and corresponding intensity and FWHM. Moreover, the peaks were deconvoluted at different spots to distinguish sp^2, sp^3, amorphous carbons and oxidized carbons to correlate with the EELS, TEM images, and XPS data.

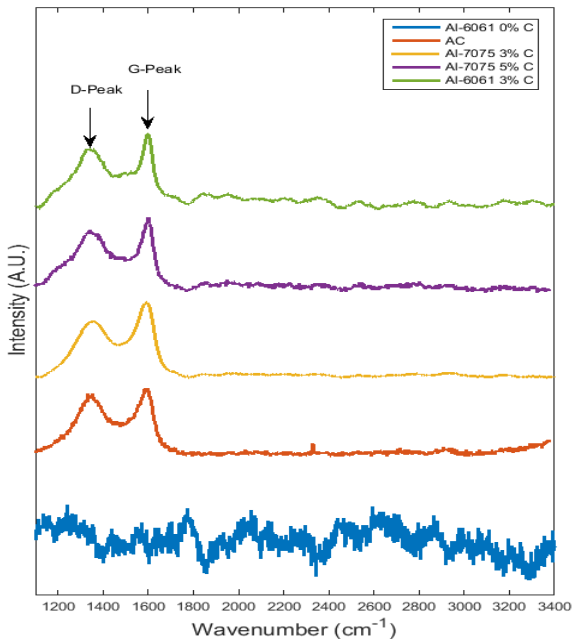

Figure 34: Raman spectra from the pure Al-6061, activated carbon (AC), Al-7075 cv-3%, Al-7075 cv-5% and Al-6061 cv-3%. G and D-peak positions are shown by arrows.

Intermediate modes and high wave number modes are not clearly visible with only weak signal in Al-6061 cv-3% and Al-7075 cv-5% in this range of wave numbers [49].

Raman maps were acquired in 20 µm ×20 µm area enclosed by a red rectangle on Al-6061 cv-3% sample as shown in an optical image in Figure 35 (a). The red dots were the spots denote where data was acquired. Figure 35 (b) shows one spectrum from one of the spots with G and D-peaks. In Figure 35 (c) the G and D-peak regions were peak fitted with Breit-Wigner-Fano (BWF) and Lorentzian curves located at 1594 and 1348 cm^{-1}, respectively. The Gaussian peak in-between the G and D-peaks at 1518 cm^{-1} was due to the unreacted residual source amorphous carbon, possibly originated from the hydrogenated process of production [52]. Intensity variations were observed for the G and D-peaks (Figure 36 (a) and (b)) in the region scanned shown in Figure 35 (a).

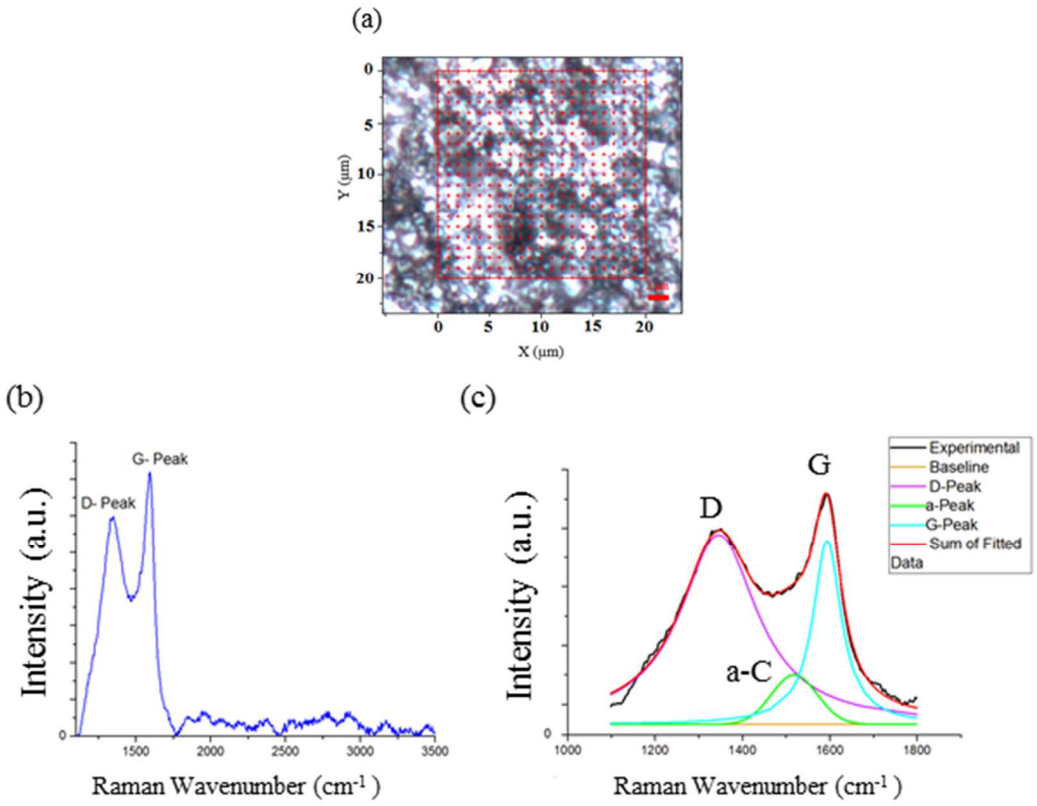

Figure 35: (a) Optical image of the scanned area of 20 μm × 20 μm outlined by the red square. (b) Raman spectrum of a point showing G and D peaks at 1594 cm^{-1} and 1348 cm^{-1}, respectively. (c) Peak fitting of the experimental data in the G and D regions with BWF for G-peak, Gaussian for amorphous peak and Lorentzian for D-peak [50].

The overlapping of the G and D-peaks suggested the presence of graphene oxide supporting the EELS results that consistently showed the presence of excess oxygen in the carbon rich regions. In the high wavenumber regions in the Raman spectra, there was no appreciable peak at the positions of the 2D and 2D/ peaks typical of single layer graphene and graphite. A broad hump like feature appeared in such regions suggesting the presence of GNR in agreement with previous observations [53, 54]. Moreover, when graphene and/or multilayer graphite interact with the substrate and metals, such high wavenumber peaks may disappear due to interaction of the electron-photon coupling with host atoms. Such behavior was observed in graphene incorporated in Ti and Cr [55]. These Raman results also supported EELS results where mixture of sp^2 and sp^3 carbons were observed.

In the Raman maps of Al-6061 cv-3%, both the G and D-peak intensities varied from region to region in almost similar ratios (Figure 36 (a) and (b)). The intensity and FWHM of the G-peak often depend upon the number of carbon layers, widths of GNR, angle of bonds, and crystallinity [40], whereas, the D-peak is correlated with the concentration of defects and disorders in graphitic layers [42]. Figure 36 (c) shows little variations of the G-peak positions from 1585 cm^{-1} except at some localized regions, the characteristic position of the unstrained carbon (dark blue region). The

FWHM of these regions were also very similar ~80-85 cm^{-1}. The D-peak positions ranged from 1367 cm^{-1} to 1341 cm^{-1}, indicating the presence of sp^2 carbon. The low intensity regions (bluish) created very small island like features in the G and D-peak position maps (reddish) where the G and D-peaks with narrower FWHM (Figure 36 (e) and (f)) had blue and red shifts by 10 cm^{-1}, respectively. The lowest D-peak in these regions observed was 1341 cm^{-1}, a position that matched with edges of monolayer graphene on the Si substrate [56-58].

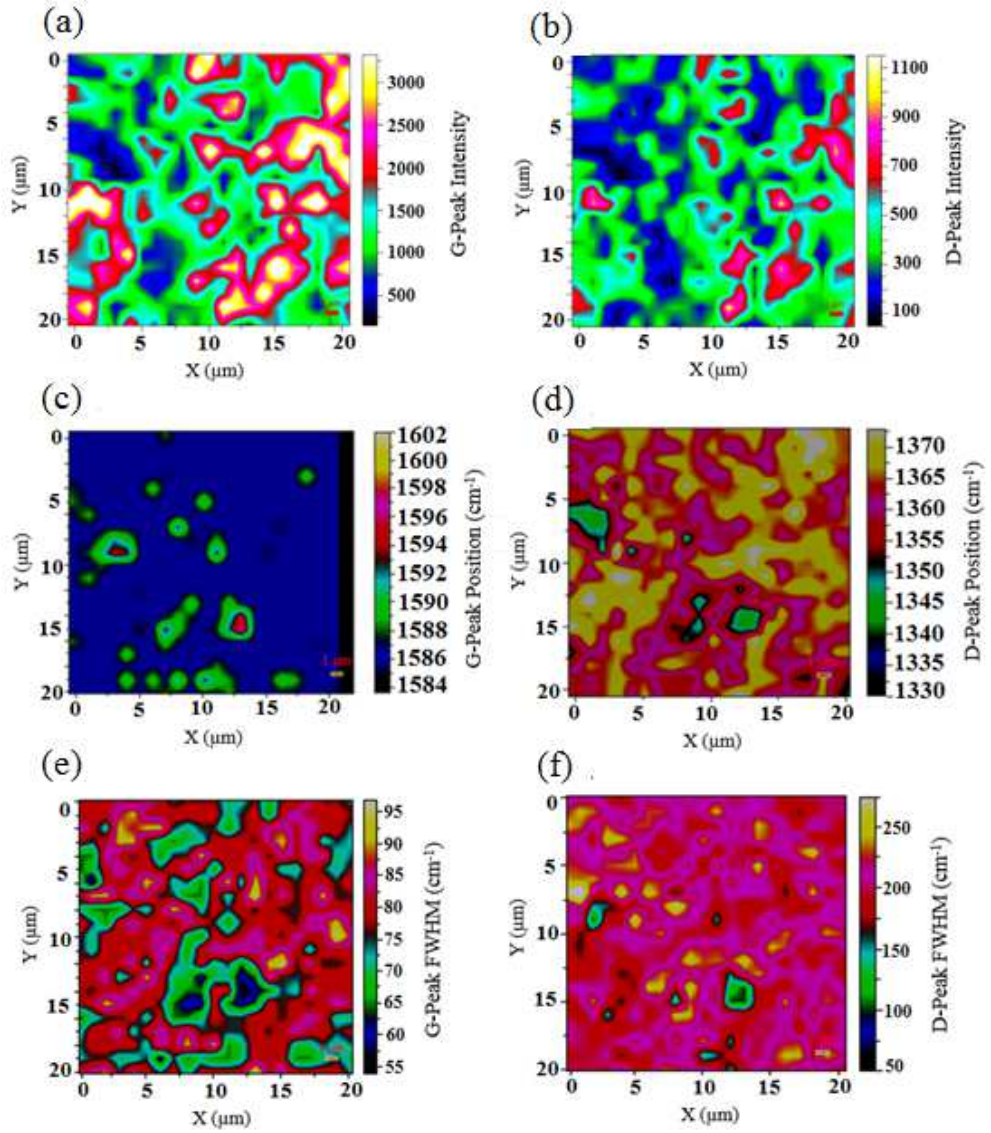

Figure 36: Raman mapping of 20 μm × 20 μm area of the Al-6061 cv-3% (a) G-peak intensity, (b) D-peak intensity, (c) G-peak position, (d) D-peak position, (e) G-peak FWHM, and (f) D-peak FWHM [50].

The blue shifts are indications of compressive strains as observed in TEM results due to thin layers of graphite bonding with the Al-metal [59]. The change of the G-peak positions resulted from the anti-harmonic induced modes in the regular hexagonal carbon structures, and subsequent changes in the stiffness of carbon bonding. Changes in D-peak positions might be attributed to the folding or multilayer stacking of graphene nanoribbons [60].

Statistical analysis was carried out from the raw Raman data. It was found that with increasing G and D-peak positions, the FWHM reduces and increases, respectively, supporting the mapping results. The average crystalline sizes of carbon measured by Raman were around 8-11 nm for the samples, closely matching the TEM results of GNR widths. The quality of carbon, quantified by the integrated intensity ratio of the D and G peak, I_D/I_G ratio varied from 2.1 to 2.5 for Al -Covetic samples which means that the carbon nanostructures were highly defective.

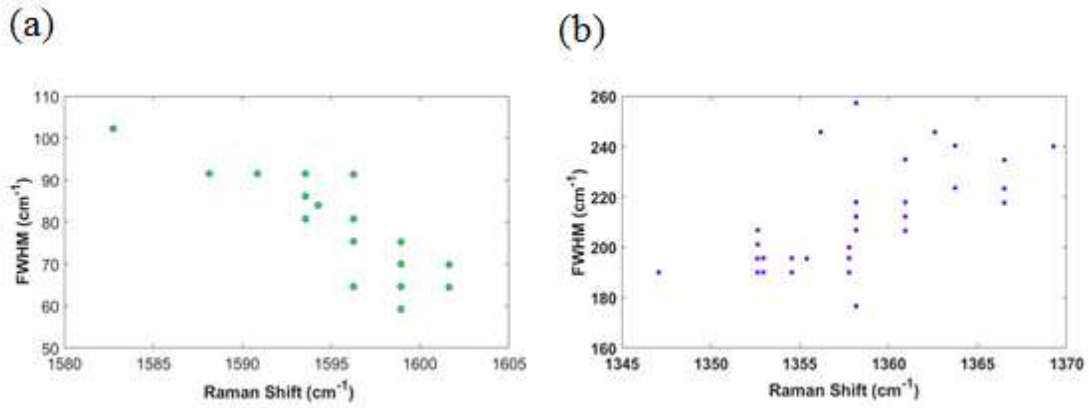

Figure 37: (a) FWHM (cm^{-1}) vs. G-peak position. (b) FWHM (cm^{-1}) vs. D-peak position of Al-6061 cv-3% sample.

In case of the Al-7075 cv-3% and 5%, more variations in intensity and peak positions were observed in the Raman maps (Figure 38). However, compared to the Al-6061 cv-3%, the G-peak positions ((Figure 38 (c)) were at relatively higher wavenumbers up to 1606 cm^{-1}. The D-peak maps ((Figure 38 (d)) showed mostly sp^2 carbon with clusters of sp^3 carbon. The FWHM of these peaks ((Figure 38 (e) and (f)) were also broader indicating higher defect concentrations, more oxidations, and lack of crystallization which were not surprising as the XPS showed noisy signal of C1s (Figure 30 (a)) with different oxidation states (Figure 31).

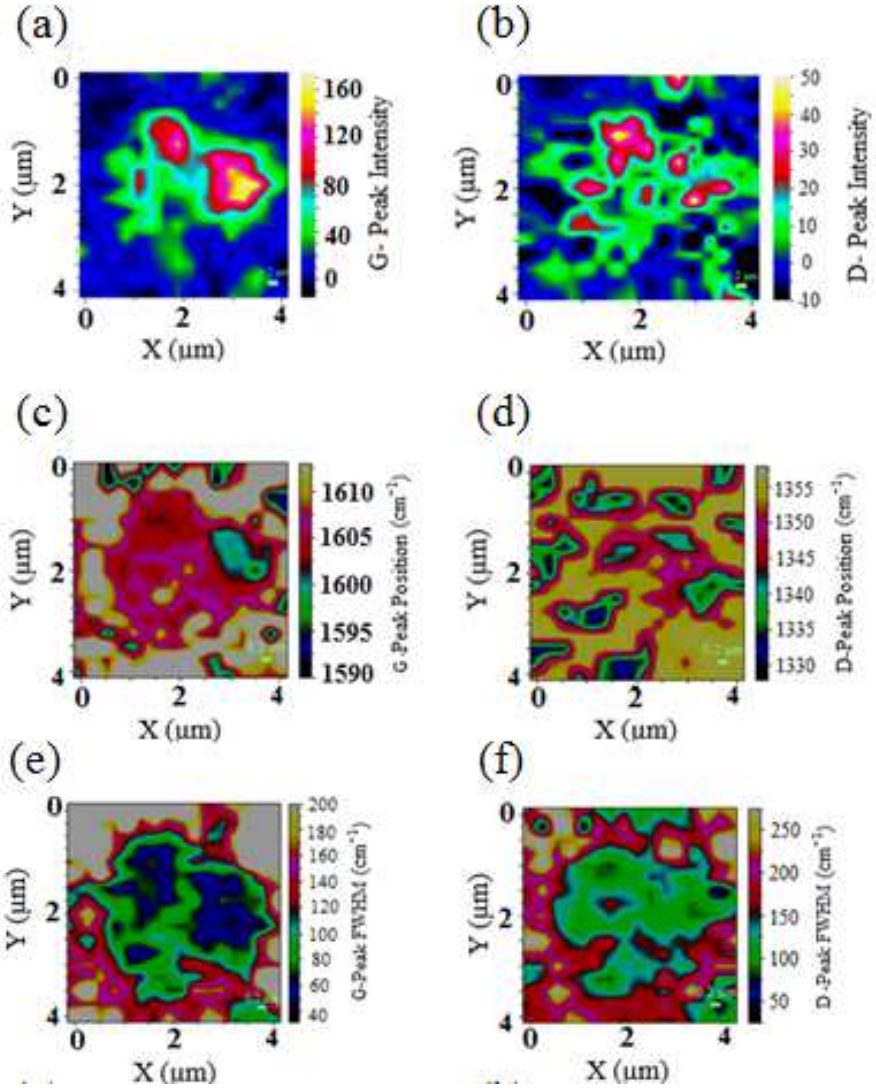

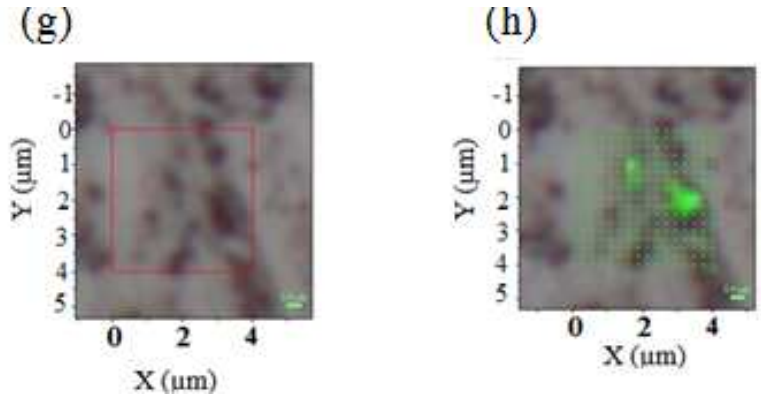

Figure 38: Raman mapping of 4 µm × 4 µm area of the Al-7075 cv-5% (a) G-peak intensity, (b) D-peak intensity, (c) G-peak position, (d) D-peak position, (e) G-peak FWHM, (f) D-peak FWHM, (g) optical image of the scanned region inside the red square, and (h) G-peak intensity overlapped on optical image.

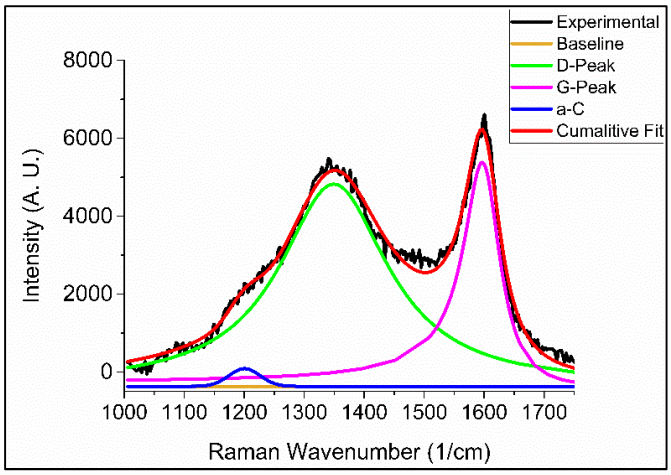

Figure 39. Raman spectrum and peak deconvolution from one of the points of Al-7075 cv-5%. G-peak at 1600 cm^{-1}, D-peak at 1350 cm^{-1}, with I_D/I_G= 2 and an additional peak at 1200 cm^{-1}.

Peak deconvolution in one of the spots of Al-7075 cv-5% revealed the G, D and amorphous peaks at 1600, 1350 and 1200 cm^{-1}, respectively (Figure 39). Crystalline sizes of the graphitic structure in Al-7075 cv-3% and 5% were 7-10 nm, very similar to Al-6061 cv 3%.

4.2.5. KPFM Mapping of Al-Covetic Samples

AFM height and phase maps, and KPFM potential maps were obtained from regions of 5 μm x 5 μm for the Al-Covetic and pure samples. KPFM results showed the presence of carbon nanostructures by utilizing the potential contrast of the carbon with the host Al and other alloying metal elements such as Zn, Mg and Cu. Clear difference was observed between the pure and Covetic samples of Al-6061 series in Figure 40 and Figure 41. The dark regions in both the phase and potential maps in Figure 40 (b) and (c), respectively, corresponded to carbons in the Covetic samples. The phase image contrast in the Covetic sample suggested different chemical nature from the host Al, and the potential maps supported the expected lower potential values arising from the presence of carbon.

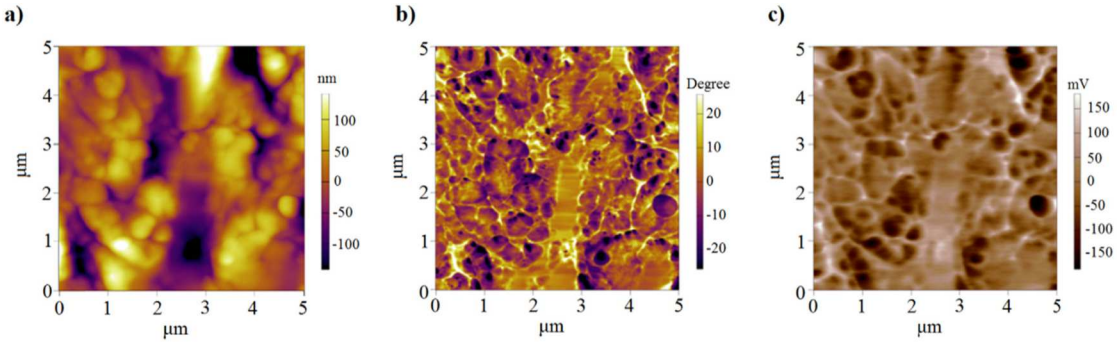

Figure 40: (a) AFM height, (b) AFM phase, and (c) KPFM potential mapping of Al-6061 cv-3% sample. There is a correlation between the dark regions in (b) and (c) suggesting that these regions contain carbon because of the lower work function between the AFM tip and carbon compared to that of the tip and the Al-matrix [49].

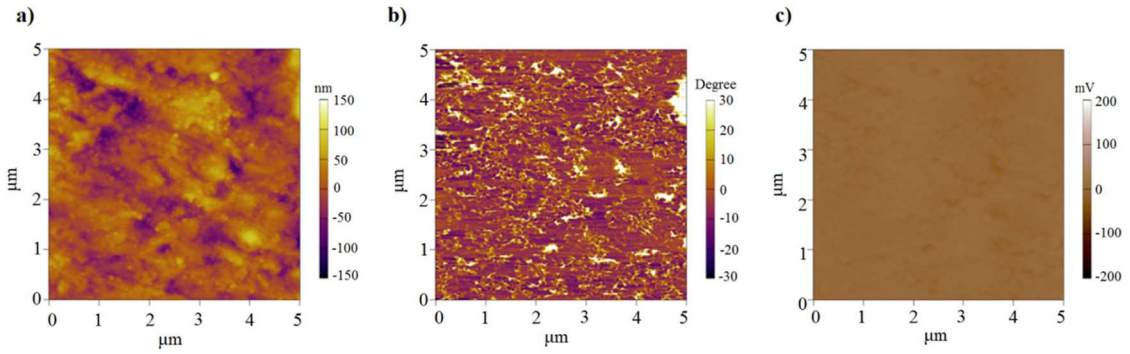

Figure 41: a) AFM height, b) AFM phase, and c) KPFM potential mapping of pure Al-6061 sample of the same region. The phase and KPFM images show clear differences compared to the Al-6061 cv-3% in Figure 40. Potential mapping is uniform in the whole scanned region unlike the Covetic sample [49].

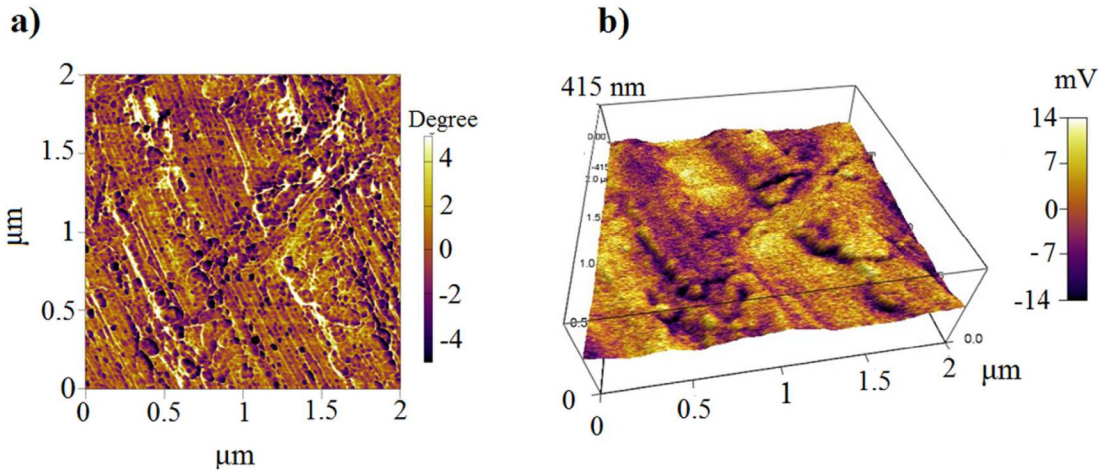

Figure 42: (a) AFM phase and (b) KPFM potential mapping overlaid on the topographic image of the Al-7075 cv-5% sample showing correspondence of the dark regions in both figures which suggest formation of carbon ribbons. In (b) the lower potential regions indicate a phase of higher conductivity. Also, the KPFM map shows a directional preference of lower potential regions which agrees with the phase image [49].

Similar to the Al-6061 cv-3%, Al-7075 Covetic samples also showed the presence of carbon in phase and KPFM images (Figure 42). The KPFM images have

limitations in terms of resolution due to the larger AFM tip radius and the height of scans maintaining 10 nm. Although KPFM did not distinguish individual GNRs as seen in TEM, clusters of these GNR like features were observed in these images.

4.3 Future Studies

Although it is obvious that sp^2 carbon is embedded by the Covetic process, and enhancement of mechanical and electrical properties are observed with carbon doping in Al alloys, the exact mechanism of higher electrical and thermal conductivity is still unknown. Moreover, the thin film properties are unknown for these alloys. Based on these, few ideas for the future experiments are described below:

One possibility is that the Al being a metal donates electrons to the embedded graphene or thin layers of graphite which contributes to the higher electrical and thermal conductivity. The electronic structure modification of a single or multiple graphene layer intercalated by Al might result into changes in the bandgaps of carbon allotropes as well as the density of states of Al. Any exchange of electrons from the metal to graphene/graphite will result in n-type. Therefore, it is important to investigate in detail the role of carbon nanostructures on the Al alloys. Previously, angle-resolved photoemission spectroscopy (ARPES) studies of Al/graphene/Ni and graphene/Ni [61], and a single graphene layer on Ru(0001) upon gold intercalation [62] have shown that depending upon the substrate, intercalation, and number of layers, the electronic properties of the metal change by distorting the symmetry of graphene which sometimes opens up a gap in the Dirac-cone.

In case of Al-Covetic materials, identifying the exact mechanism of conduction can provide more controlled growth to optimize electronic properties. However, such

experiments to probe band-structure are quite difficult as carbon was embedded in a 3D epitaxial nature in Al. One limitation of ARPES comes from the requirement of getting atomically smooth surfaces for band structure and Fermi surface determination. One possible way to overcome such limitation might be to create thin films at very slow deposition rates by PLD or sputtering, and then probe the region using ARPES. In the previous works of Cu-Covetic, PLD successfully transferred Cu-C on Si and sapphire, and showed crystallinity of the films with some texture [36, 37]. Therefore, it might be possible to do the similar deposition for Al-Covetics. Such thin films might have sp^2 and sp^3 contents based on the deposition parameters such as pressure and temperatures. These allotropes in smooth thin films could be correlated with the ARPES results to better understand the electronic nature of Al-Covetic.

Another technique might be to use the current Covetic materials for to make very thin TEM samples by FIB to acquire EELS data at atomic resolution. The C-K and Al-K edge profile might indicate the presence of hole/electron doping by the variations from the relative peak intensity and widths which reflects the change of the DOS of the Fermi level. Comparing these signals from sp^2, sp^3 and amorphous regions with such features can give in depth knowledge of Al-C electron transfers along different crystallographic directions.

In addition, the thin film properties of the Al-Covetic alloys are still not investigated. Thin film deposition by PLD, sputtering or other techniques might be examined to find the electrical and thermal properties. Al is widely used in electronics as conducting channel. The presence of different alloying elements might be interesting to investigate since Al-Covetic have shown anti-corrosion properties.

4.4 Conclusion

The formation of crystalline sp^2 carbon has been confirmed in Covetics throughout the Covetic samples of Al-6061 and Al-7075 using different characterization techniques such as TEM, XPS, KPFM, Raman and EELS mapping. TEM images revealed that the incorporated carbon in the Al-matrix created networks of GNR embedded parallel to the <112> directions of Al metal on the (111) plane. The SADP showed the epitaxial orientation of (111) Al // (0001) graphite and $<1\bar{1}0>$ Al // $<11\bar{2}0>$ graphite with a compressive strain of ~ 3.3% of the graphitic layers. Oxidations of the GNR and carbon-metal bonding were revealed in XPS. Raman mapping supported the dominant presence of sp^2 carbon seen by XPS in Al-6061 cv-3%. In terms of atomic percentages, the Al-6061 cv-3% had higher carbon concentration with less oxidation and defects compared to Al-7075 Covetic samples. The carbon network observed in this study is believed to be the main factor behind the increase in ultimate tensile strength in Al-Covetic alloys as well as previously reported increase in electrical conductivity. These characterization results provide insight into the role of the Covetic process to develop hybrid metal-carbon materials having great implications in different defense, aerospace, civil, and electronics applications. Other similar thermodynamically limited alloy systems might use similar Covetic technique to fabricate novel materials.

Chapter 5: Characterization of Ag-Covetic

In this chapter, Ag-Covetic bulk samples are studied using TEM, EELS, Raman and KPFM mapping. Both strained and unstrained sp^2 carbons along with sp^3 bond were found in these samples. Besides, some residual amorphous carbon was detected in Raman and EELS maps. KPFM showed GNR like structures similar to the TEM results.

5.1.1 Previous Results of Ag-Covetic

Previous studies of Ag-Covetic samples showed the 3D epitaxial nature of graphitic-like sheets or GNR with Ag (111) crystal planes similar to Al-Covetic (Figure 43 (a)) [38]. The thermal stability of these Covetic systems indicated strong bonding

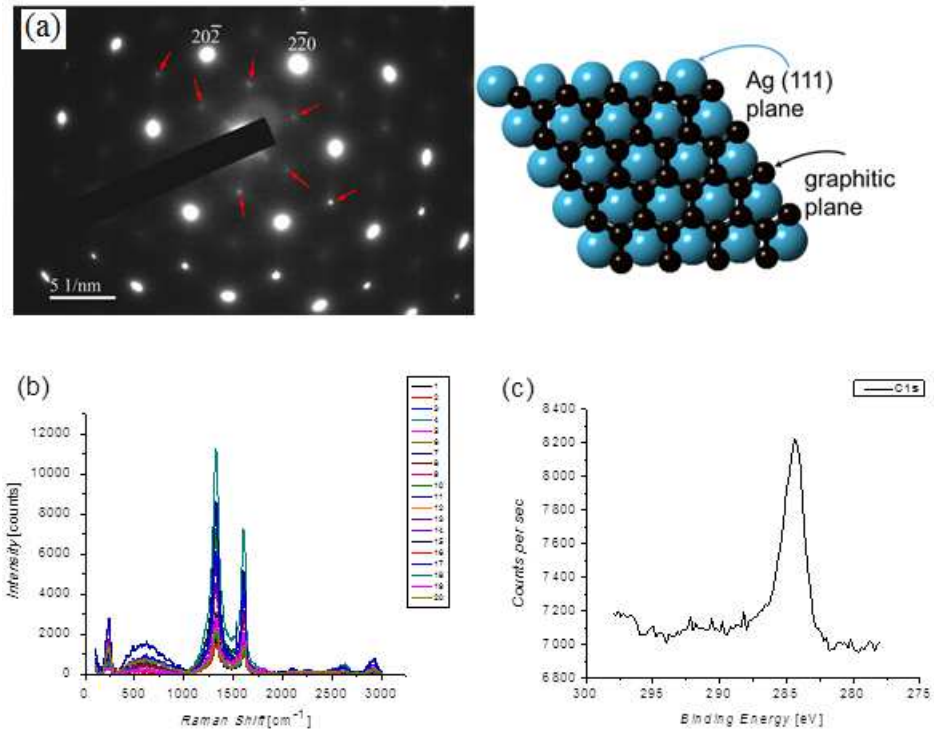

Figure 43: (a) (111) electron diffraction pattern from Ag cv-3% (strong spots are <220> Ag) with (0001) graphite-like diffraction pattern (weak spots marked with red arrows)

showing 3D epitaxy between Ag and graphitic-like sheets. The schematic on the right presents the epitaxial orientation between the (111) atomic plane of Ag (blue) and the (0001) plane of graphite (black). (b) Raman spectra along a line (c) C 1s spectrum from an Ag cv-6% sample after sputtering for 360 secs with asymmetric shape with sp^2 bonding [38].

between the carbons and host Ag-metal. Although there was evidence of high concentration of sp^2 carbon by Raman and XPS (Figure 43 (b) and (c)), more research was required to detail the characteristics of the present carbon. Therefore, in this chapter, TEM, EELS and Raman mapping of the Ag cv-6% are studied.

5.1.2 TEM & EELS of Ag-Covetic

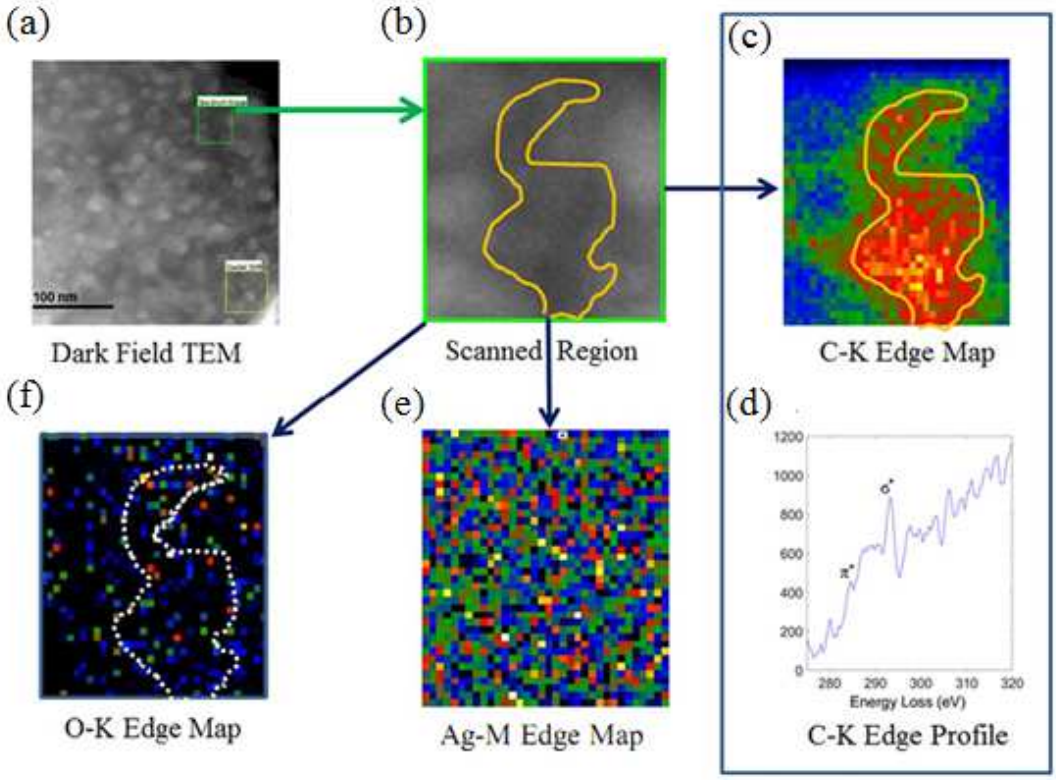

Figure 44: (a) HAADF image of Ag-cv 6%. (b) Magnified region where EELS spectrum imaging corresponding to the green rectangular area on the top right region

in (a) was obtained. (c) C-K edge map in temperature gradient color. The curve encloses the region highly rich in carbon. (d) C-K edge profile from one of the points in the scanned region after background subtraction showing sp^2 characteristics. (e) Ag-M edge map. (f) O-K edge map.

EELS map was taken for the region within the green rectangle shown in Figure 44 (a) and (b), and C-K edge map was plotted in Figure 44 (c). The dark region in the DF images was carbon enriched as the light elements in DF imaging appears darker. The individual signals from the different spots showed the presence of 1s to π^* and σ^* transitions at 284 and 290 eV, respectively in Figure 44 (d), the characteristic edges of the graphitic carbon with sp^2 bonding. The Ag-M edge map showed no preferential nature of the Ag in Figure 44 (f). A minute presence of oxygen was detected in the scanned region and did not show any correlation with the carbon enriched regions Figure 44 (f).

To visualize the relative presence of sp^2 and sp^3 enriched regions, the BSS technique was applied, and individual images were obtained showing the relative concentration of the allotropes in the scanned regions of Figure 44 (a). The remapping in Figure 45 (a) showed that the bottom region which was highly carbon rich had high sp^2 content. The dominant signal also resembled the essential features of the sp^2 carbon in Figure 45 (b). It appeared that sp^2 carbon was terminated by sp^3 carbon which went further into the host Ag-metal in the Figure 45 (c) with a characteristic signal of amorphous carbon shown in Figure 45 (d).

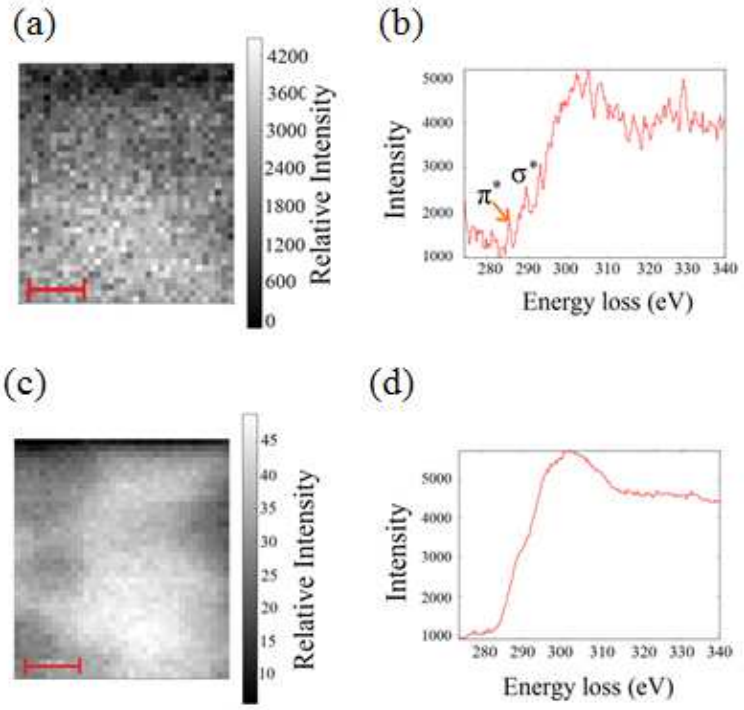

Figure 45: Spectral decomposition of the EELS mapping shown in Figure 44 by BSS method. (a) A dominant signal resembling sp^2 carbon shown in (b). is mapped where the high concentration is observed in the lower middle region as seen in the highly rich carbon region in Figure 44 (c) Another dominant signal resembling amorphous carbon signal shown in (d) used for mapping. Maps of the two components in (a) and (c) coincide with the enriched carbon region in Figure 44 (c). The red scale bars in (a) and (c) correspond to100 nm.

5.1.3. Raman Mapping of Ag-Covetic Samples

The Raman signals and maps acquired from Ag cv-6% showed more variation in terms of the G and D-peak positons, and clustering and networking of sp^2 bonds in sp^3 enveloped regions compared to Al-Covetics.

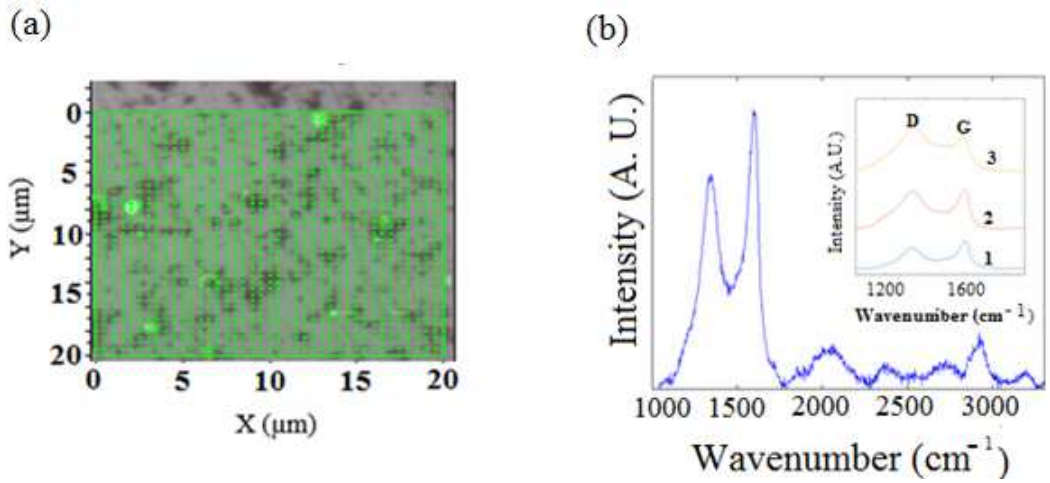

Figure 46: (a) Optical image of the scanned area of Ag-cv 6% sample. The green points show where spectra were obtained. The regions with high G- peak intensity were superimposed on the optical image and show very high carbon content in those areas. (b) Individual Raman spectrum of a point showing intermediate Raman modes. The inset presents the variations in intensity and widths of the G and D-peaks at three different locations.

The optical image of the scanned region was overlapped with the G-peak intensity in Figure 46 (a). One individual spectrum shown in Figure 46 (b) showed intermediate Raman modes, and in the inset the variations in the I_D/I_G is shown at three different spots. Therefore, to investigate the details, peak fittings of the Raman signal were done at different spots. Figure 47 shows two such cases where amorphous carbon peaks were detected at different wavenumbers along with the G and D-peaks with counts around ~10% of the total carbon. The amorphous carbon peak at ~1510 cm^{-1} region in these deconvoluted spectra possibly originated from the hydrogenated process of production [52]. The high values of I_D/I_G and D-peak FWHM of these spots indicated high concentration of defects. Besides, the high intensity of the D-peak might arise from the large spot size of the Raman (700 nm) interacting with the much narrower

GNR picking up signals from the broken bonds and edges of GNR, and oxidation of carbon.

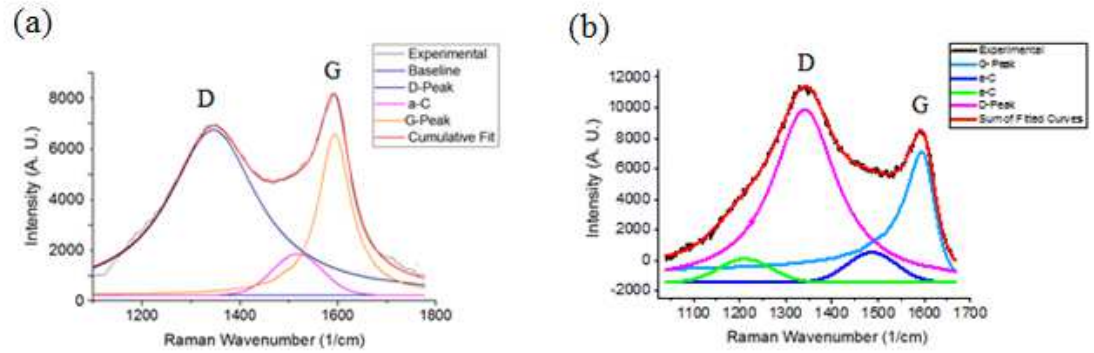

Figure 47: Deconvolution of the experimental Raman signal at two different points on Ag-cv 6%. (a) Spectrum from one point showing G peak at 1599 cm^{-1}, D peak at 1343 cm^{-1}, and a weak additional peak at ~1534 cm^{-1}. The I_D/I_G for this fitting was 2.3. (b) Spectrum from another point with G peak at 1596 cm^{-1}, D peak at 1346 $cm^{-1}$and two weak additional peaks at 1211 and 1486 cm^{-1}. The I_D/I_G was 2.4 for this fitting. The amorphous regions correspond to ~10% of the integrated areas.

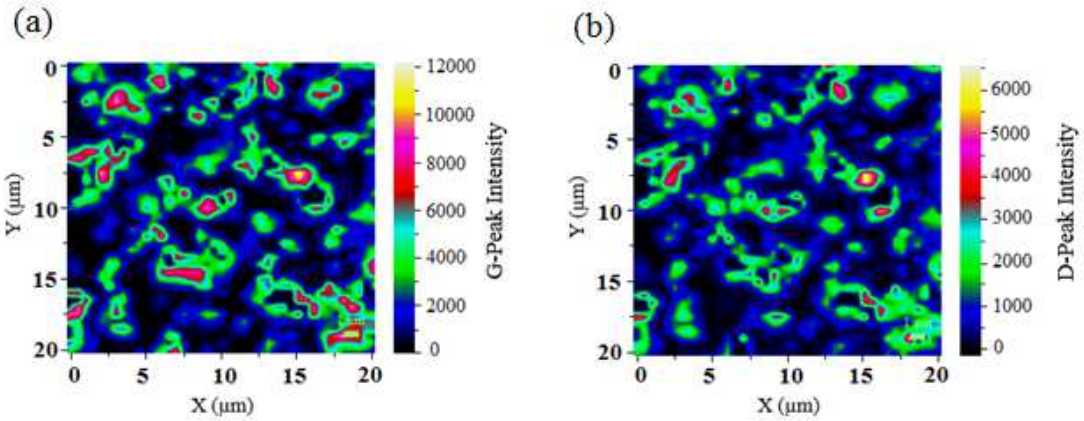

Figure 48: Raman intensity map of Ag cv-6%. (a) G-peak intensity, (b) D-peak intensity.

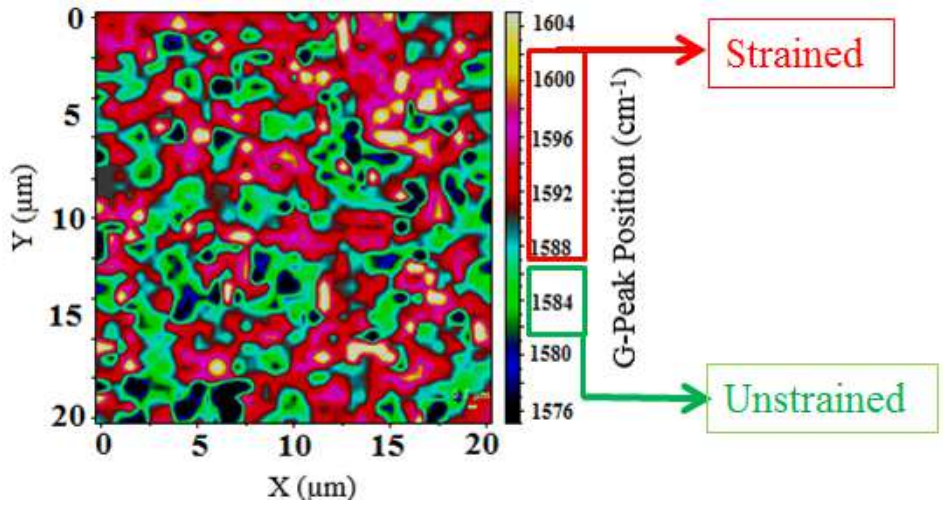

Figure 49: G-peak position map showing variation of Ag-cv 6% ranging from 1576 cm^{-1} to 1606 cm^{-1}. The greenish regions at 1585 cm^{-1} correspond to unstrained areas. Strain variations appear in cluster like pattern with the lower strained areas surrounding the highly strained areas.

The non-uniformity of the G and D-peak intensity maps (Figure 48) along with the G-peak positon (Figure 49) map showed that the low intensity regions in Ag cv-6% were mostly unstrained. Connected clusters of gradually increasing high wavenumber G-peak regions were observed. The shift of G-peak is strongly correlated with the strain. Lattice mismatch induced strain between Ag and graphene was found to shift the G-peak position [38, 63]. Moreover, there are several other factors such as reduction in crystallite size (nano-crystalline carbon) and increase of sp^3 bonding that might be behind such blue shifts [64]. There are also some examples of shifts of the G-peak based on the substrate. Graphene with 1% compressive strain deposited on SiC substrates and PET substrates had blue shifts by 10 cm^{-1} [65] and 14.2 cm^{-1} [66], respectively. From the above discussions, it is clear that the shift of the G-peak might be complicated due to different factors, and comparing it is also challenging as in the

Ag cv-6% both sp^2 and sp^3 carbons created networks throughout the sample (Figure 50). The position of the D-peak varied from 1331 to 1354 cm^{-1}. The sp^3 carbon might be due to the amorphous carbon or the terminating species for the sp^2 carbon. Such sp^3 networks might be the reason for slightly reduced conductivity in the Ag sample reported earlier [38].

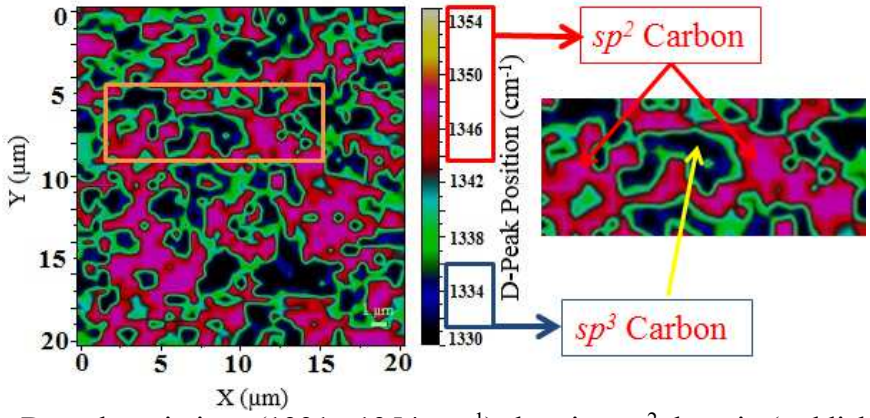

Figure 50: D-peak variations (1331 - 1354 cm^{-1}) showing sp^2 domain (reddish regions) network enveloped by clusters of sp^3 domain (greenish regions) creating mixed bonding at the boundaries. The small rectangle area on the left is enlarged on the right [50].

5.1.4. KPFM Mapping of Ag-Covetic Samples

AFM and KPFM were carried out in 2 μm× 2 μm area for the pure Ag and Ag cv-6%. The results are presented in Figure 51. The KPFM images showed relatively low potential areas in several regions in the Ag cv-6% maps, some of which appeared like narrow width ribbons in Figure 51 (c) and (d). The dark potential contrast is believed to be due to carbon enriched regions. This might be due to varying degrees of defect concentrations, and the high presence of sp^3 carbon with sp^2 carbon. These results were supported by the Raman and EELS mapping.

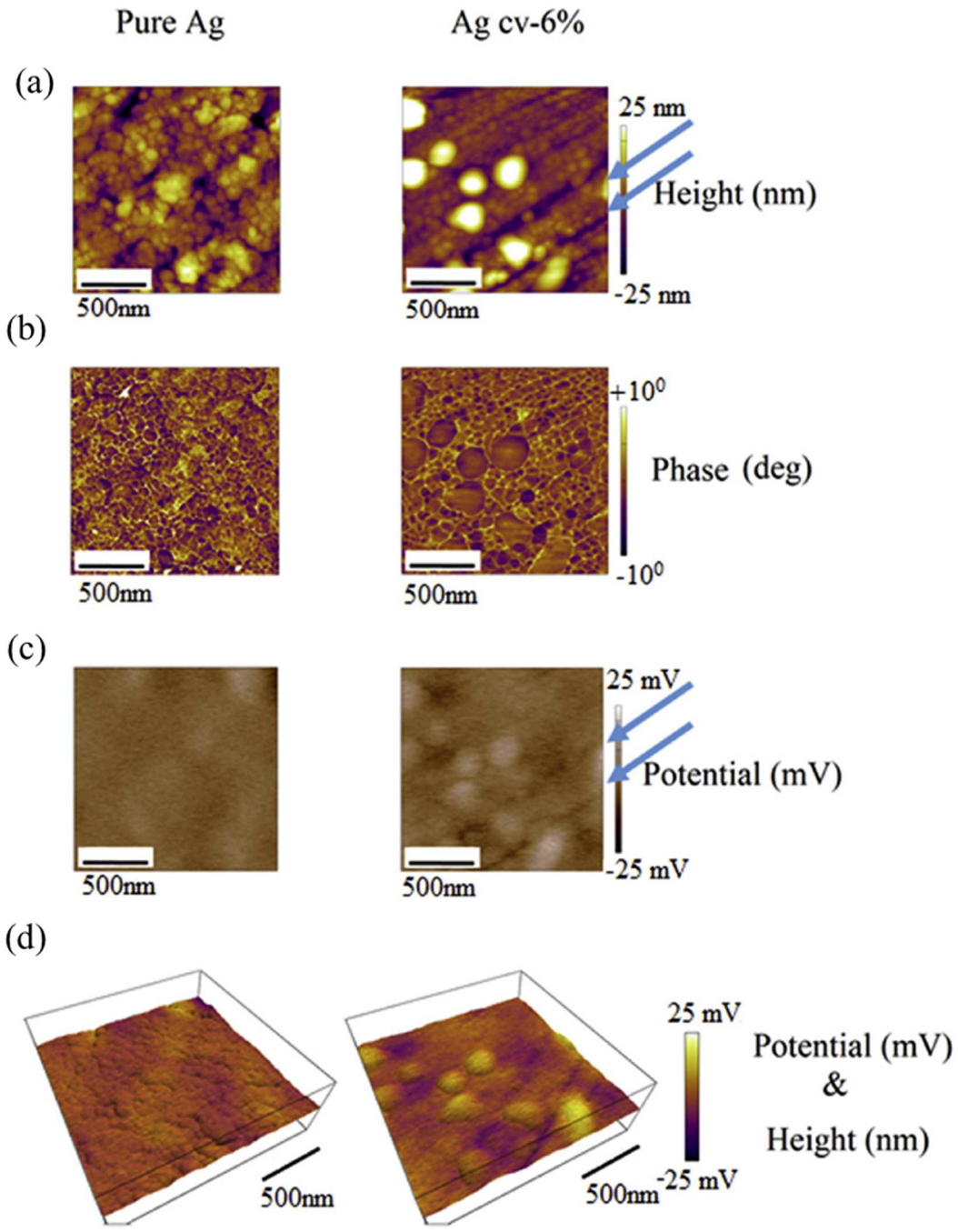

Figure 51: Comparative AFM (height and phase) and KPFM images of pure Ag (left) and Ag cv-6% (right). (a) Height maps. (b) Phase maps. (c) Potential maps using KPFM (scale: -25 mV to 25 mV). (d) Height maps with potential overlay. Lower potential

regions with phase and height contrast appear to show ribbon-type features on the bottom right regions of the Covetic sample marked by blue arrows.

5.2 Future Studies

Further studies might be conducted to investigate how to reduce the sp^3 carbon in the Ag-Covetic for improving the electrical properties. This will require proper understanding of the role of specific current, heat treatment procedures and other processing parameters. It is important to identify if such allotrope distribution is due to the crystal structure of Ag, or due to the thermodynamic conditions during the Covetic process.

In addition, thin films of the Ag-Covetic can be studied for investigating the corrosion properties under different gaseous conditions. It might be possible to tune the orientation of the Ag-C bonding by choosing suitable substrates, and enhance the electronic and mechanical properties.

5.3 Conclusion

In this chapter, we have found by EELS and Raman that in Ag-Covetic samples, both sp^2 and sp^3 carbon along with amorphous carbon were present. The sp^2 carbon created a network like structure and was surrounded by sp^3 carbon. Higher degrees of strain were observed by Raman spectroscopy. KPFM mapping showed localized low potential behavior of the carbon allotropes. While inclusion of carbon is strictly limited in bulk Ag under normal materials processing techniques, by applying the Covetic process a significant amount of carbon was embedded in the noble Ag-metal. This also opens up the possibility to rethink applying Covetic process to other elements to incorporate in Ag, and utilize its high electrical and thermal conductivity.

Part II

Chapter 6: Introduction to $BaSnO_3$ Perovskite

In this chapter, we will briefly introduce the history, development and wide variety of uses of the perovskite materials. Then, we will focus on the current research on the oxide electronics and their technological importance as well as economic benefits. The last few sections will review BSO fabrication methods, properties, applications and limitations. Here, we will detail the current challenges in advancing this field, and how our current research might impact overcoming these limitations.

6.1 Perovskite

Perovskite is a large class of materials having a composition of ABX_3. The A and B are the larger and smaller cations, respectively, and X is the anion. The discovery of the first perovskite $CaTiO_3$ happened almost two hundred years ago in 1839 in the Prussian empire. Later on, $BaTiO_3$ came in focus due to its wide applications in the electronic industry in the 1940s [67]. This promoted a wide range of research studies in this field. With the advent of new technologies in thin film fabrications and materials characterizations, from time to time since 1950s, new types of perovskite with novel properties have been discovered. The fascinating properties in-terms of structure, transport and magnetic behavior make perovskite an active field of study in high temperature superconductors [68, 69], multi-ferroic [70, 71], photovoltaic applications [72], photonic sources [73], solar cells [74-76], fuel cells [77, 78], nano-catalysis [79, 80] and multilayer functionalized materials [81, 82]. Based on the fabrication conditions and post processing, many different allotropes are observed in the known perovskites. The advent of high temperature superconductors such as YBCO renewed interest in these materials in the mid-eighties [83]. Multi-ferroic perovskite based

devices have applications in tunable magnetic devices [84], fabricating hetro-structure by nano-patterning [85], and combining ferrimagnet and ferroelectric multilayers[86].

The most known perovskites are cubic ($SrTiO_3$, $LaAlO_3$), orthorhombic ($CaTiO_3$, $CdTiO_3$) [87], rhombohedral ($PrA1O_3$), and hexagonal ($BaSiO_3$) [88]. Many of these A and B sites are doped with transition metals. Based on the doping element and processing, the property of the original composition can be greatly varied which makes this perovskite field rich in multi-functional properties. Generally, these materials show more of ionic natures.

Many of the perovskites exist in different phases under different conditions. These phase transitions can be controlled by oxygen vacancy [89], temperature [90], thickness [91], voltage [92, 93] and pressure [94]. Apart from the physical structure changes, electronic reconstruction can also appear due to the structural changes and electron/hole doping. In these materials, the band-structure is affected by any change of the bonding angle between A-O and B-O sites. Therefore, complex oxide systems give a plethora of opportunities to fabricate electronic and functional materials with the desired properties.

6.2 Oxide Electronics

Oxide electronics has been an active field of research for its enormous potentials in the industry parallel to the silicon based devices. Perovskite oxides often show strongly correlated nature [95], and have active d and f orbitals originating from the rare earth elements. It is possible to tune band-gaps, and induce magnetic, ferroelectric, thermos-electric effects and optical properties with electron and hole doping in oxide electronics. There are certain characteristics of the oxide materials that

took the attention of the scientific community several decades ago. One of them is metal-insulator transition based on the external pressure [96-98], temperature [99] and oxygen vacancy [100]. Unlike metals, the electron conduction mechanisms in the oxides are quite complex because of many body election-electron and/or electron-phonon interactions [101]. Such interactions combined with the strong Coulomb interactions in the d-orbitals often show non-linear temperature dependence (T^{α}) of the resistivity with different exponents (α) based on the conduction mechanisms such as variable range hopping (VRH), electron-electron scattering, electron-phonon scattering or dislocation dominated scattering at different ranges instead of simple $T^{\alpha=1}$ dependence observed in the metals.

Among different types of oxides, wide bandgap perovskite oxides are getting attention for their multi-functional characteristics, applications in memory resistors [102] and spintronic devices [103]. Novel features were observed at the interfaces of the different insulating perovskites at ultrathin scales in 2 dimensional electron gases (2-DEG) such as ($LaAlO_3/SrTiO_3$) [104] and ($BaSnO_3/SrTiO_3$) [105] devices. Surface termination of these oxides can create desired polarization on the surface. In the case of magnetic perovskites, the control of the oxygen vacancy and their distribution can be used for high density memory devices [106]. Recent interests on all perovskite based electronics such as field effect transistor (FET) and solar cells are driving the field to find new materials for gate dielectric, conduction channels and contacts [107].

6.3 Transparent Conducting Oxide (TCO)

For transparent conducting oxide (TCO) materials, both the high electronic conductivity and optical transmission over 90% are required. This becomes challenging as the conductivity equation has reciprocal relationship between the two parameters.

$$\sigma = Ne\mu \quad (8)$$

where, e is the electron charge, N is the number of the carriers, and μ is the mobility. Generally, by doping or oxygen vacancy excess electrons are created in the system for n-type semiconductors. Theoretically, to maximize the conductivity both the mobility and number of carriers will be maximized. Lower mobility degrades the performance of the device and consumes more power. But in reality, the excess carrier concentration in materials can create carrier-carrier scattering limiting the maximum conductivity. Therefore, when a new material is designed, it is important to optimize these two parameters based on these applications.

TCO materials are generally transparent only in the visible and near-infrared regions of the light spectrum (λ= 400-700 nm). In the shorter wavelengths (λ<400 nm) and long wavelengths (λ>700 nm), absorption and high reflection occur due to the fundamental energy gap and plasma absorption edge, respectively.

Applications of TCO films are listed below:

- Display devices
- Touch panels
- Photovoltaic devices: Dye-sensitize solar cells
- Transparent logic device
- Light emitting diode (LED)

Previously, In_2O_3, ZnO and SnO_2 have been the focus of research in this field. Later on, Sn doped In_2O_3 (ITO) became the industry favorite because of its high conductance (~10^4 S cm^{-1}) and mobility. For TCO materials certain characteristics are required by the industry.

(a) Availability: The low price and the abundance of the future TCO materials are very important to meet the growing demand in the electronics industry.

(b) Stability: The materials will be stable for long term applications, and will not be prone to damage once they have been exposed in the natural atmospheric conditions. Electronics often operate at higher temperatures than their surroundings. This brings a fundamental challenge for oxide materials compared to their many lab based performances.

(c) Integration: The materials must be well-integrated with wide variety of industry standard devices and fabrication processes will be compatible.

6.4 Economic Potentials of Perovskites and $BaSnO_3$

The active research in the field of perovskites are fueled largely by economic interests. Colossal Magneto-Resistance (CMR) in different perovskites such as $La_{1-x}M_xMnO_3$ where M=Ca, Sr and Ba inspired research for the high density data storage industry [108]. Many energy applications are now related to the development of the perovskite industry. Formamidinium-lead-halide–based perovskite layers acting as solar cells achieved an efficiency of 22.1% [109], a new milestone for perovskite materials. Additionally, perovskite based fuel cell research is showing potentials for its economic benefits and to reduce the green house effects [78], similar to the solar cells. Other fields of significant perovskite applications are photo-catalysis [110] and

Hydrogen storage [111]. Both of them are important for future developments to meet the energy challenges for mass scale and customized systems.

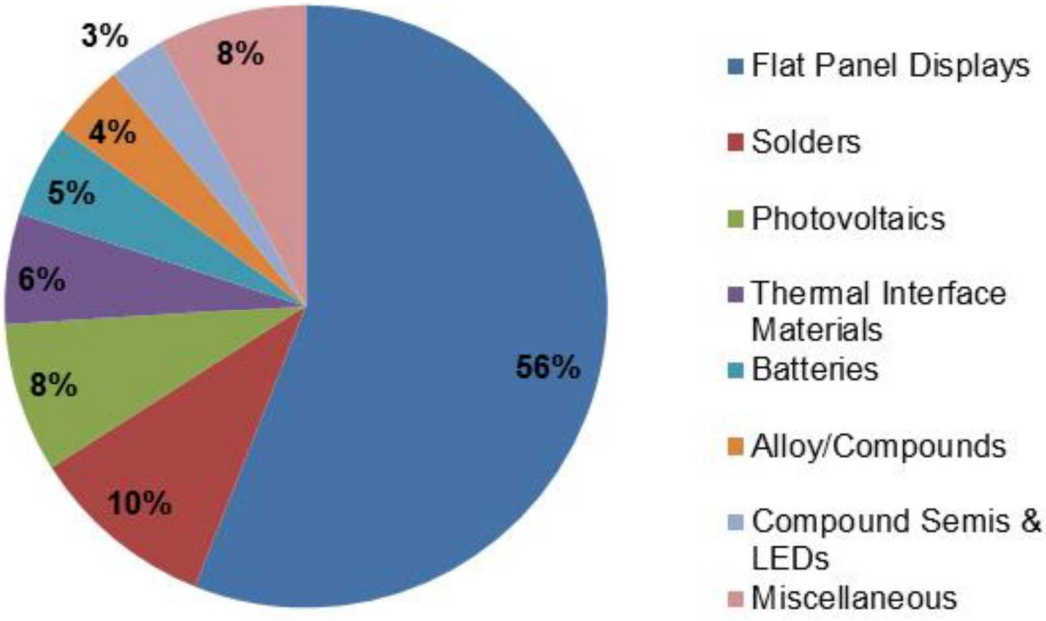

Figure 52: Use of Indium in different industry. This pie chart is plotted based on 2012 industrial uses by NREL [112].

Many perovskites are future candidates for replacing rare earth based materials which are largely imported from China and other countries. For example, Indium based ITO is largely used as transparent conducting oxide in touch-screen, solar panels, display panels and oxide electronics as shown in Figure 52. Currently, the market values of indium is over $5 billion [113]. ITO is very expensive, toxic and imported from China. Currently, the DOE is trying to make US critical industries independent of imports due to national interest, environmental concerns and reduce trade deficits by producing most of the components at home.

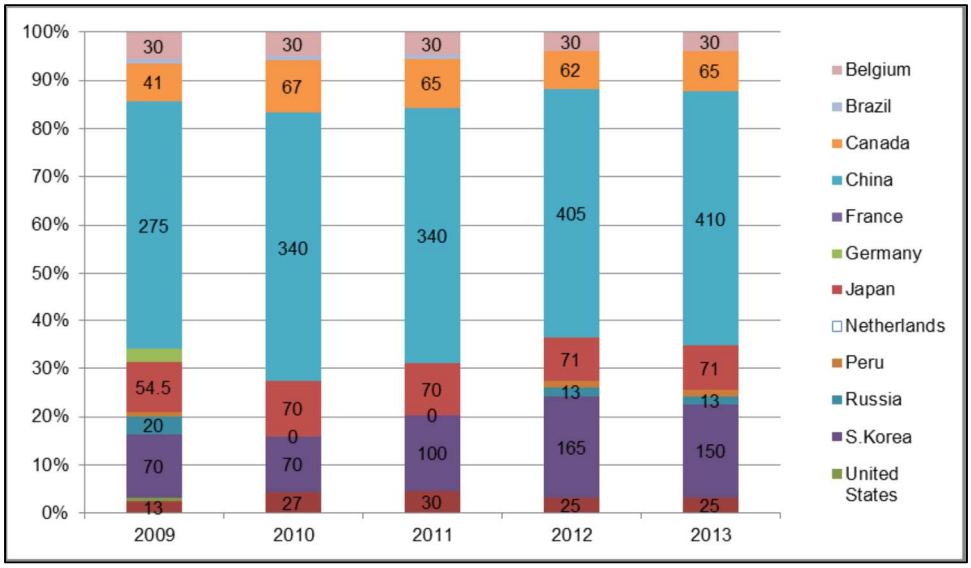

Figure 53: Country-wise distribution of primary Indium production [112]. Data plotted by NREL using US Geological Survey primary data.

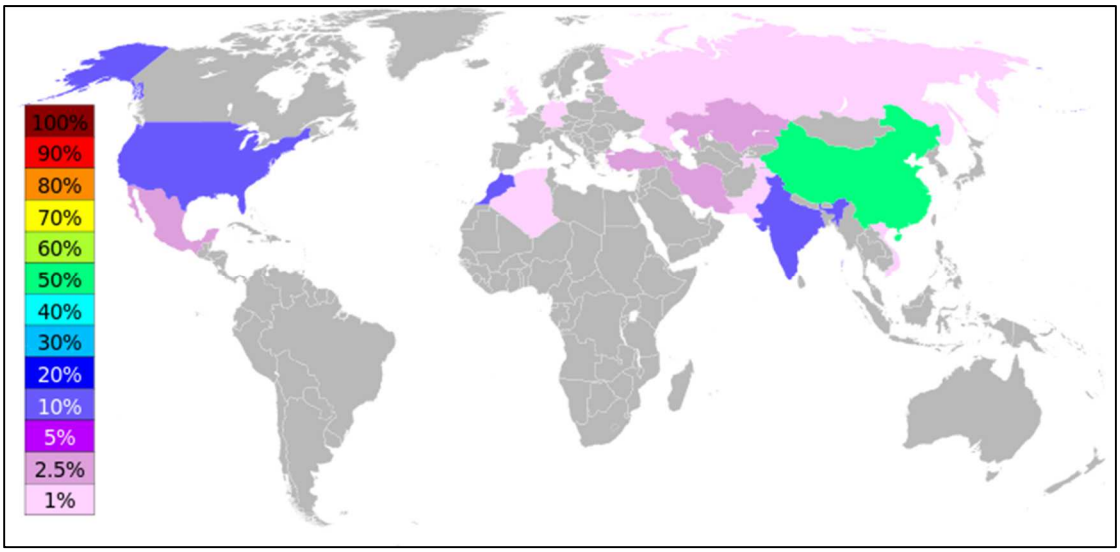

Figure 54: Map of the barite production in 2010 based on the United States Geology Survey mineral commodity survey. USA produces almost 20% of the world production of the main ingredient of Barium as a primary product.

In contrary, Barium is extracted from the Barite minerals, much cheaper and also available in USA. In 2015, about 700,000 tons of Barite valued at an estimated $91 million were domestically produced [114]. The world production distribution of

the primary source of Barium ores is shown in Figure 54. Compared to indium which is not produced in USA at all, Barium is domestically produced and also some portions are imported. According to USGS 2017 data, almost 25% tin is also produced domestically in the USA.

6.5 Crystal Structure and Band Structure of $BaSnO_3$

$BaSnO_3$ is a cubic perovskite with a lattice parameter of 4.116 Å in bulk. It belongs to the space group of ($Pm\bar{3}m$). The Ba^{2+} ion lies at the corners of the BSO unit cell whereas the smaller cation Sn^{4+} centers inside the unit cell creating octahedron consisting of O^{2-} atoms. In an ideal case, the O-Sn-O bond is linear.

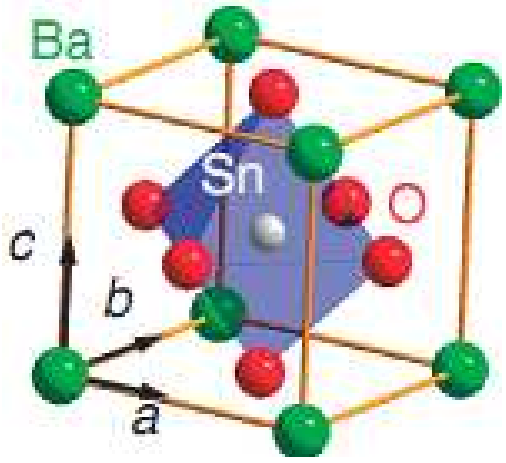

Figure 55: Ideal BSO cubic crystal structure [115].

The BSO can be doped both at A and B site with La [116], Sr [117], Eu [118],Sb [119], Pb, Bi [120], and Fe [121]. Such doping distorts the cubic structure based on the dissimilar ionic radius and bends the O-Sn-O bonding.

In the band structure of the BSO, Sn 5s is the conduction band with little contributions from d bands, and O 2p is the valence band orbital. Having an s-band conduction orbital gives more dispersion than other d-orbital based perovskites

resulting in higher mobility. The measured indirect bandgap of BSO by optical spectroscopy (OS) and hard x-ray photoemission spectroscopy (HAXPES) is in the range of 3.1-3.55 eV [122]. The band-structure of BSO has been calculated by many different techniques with a wide range of bandgap values from 0.74 to 3.3 eV as listed in Table 8 [123]. However, all these methods agree on the presence of the indirect bandgaps between the $R(1/2,1/2,1/2)$ point of the Brillouin zone (maximum of valence band) and the $\Gamma(0,0,0)$ point (minimum of the conduction band).

Table 8: Band gap values and VBM/CBM locations in k-space predicted from the theoretical and experimental method.

Method (Theory)	E_g (eV)
LDA [124]	1.51
GGA [124]	0.74
PBE [125]	2.83
PBE0 [126]	3.22
HSE1 [127]	2.48
HSE2 [127]	3.0
LAPW [128]	3.3

Stanislavchuk et al. applied generalized-gradient approximation (GGA) with Perdew-Burke-Ernzerhof (PBE) local functional using the CASTEP code [125]. Although they reached 4% deviations for the lattice parameter calculations, this method largely underestimated the indirect-band between the $R(1/2,1/2,1/2)$ point of the Brillouin zone (the maximum of valence band) and the $\Gamma(0,0,0)$ point (the minimum of the conduction band). The calculated value of the bandgap was 2.83 eV as shown in Figure 56. Much lower values of 1.51 and 0.74 eV were reported by local density approximation (LDA) and GGA, respectively [124]. Significant improvements were observed by applying hybrid methods such as Perdew–Burke–Ernzerh of exchange-

correlation functional augmented with 25% Hartree–Fock exchange (PBE0) [126] and linearized augmented-plane-wave (LAPW) [128]. The band gap values reached 3.2-3.3 eV as shown in Figure 57, much more realistic compared to other techniques. Such techniques are computationally expensive and time consuming.

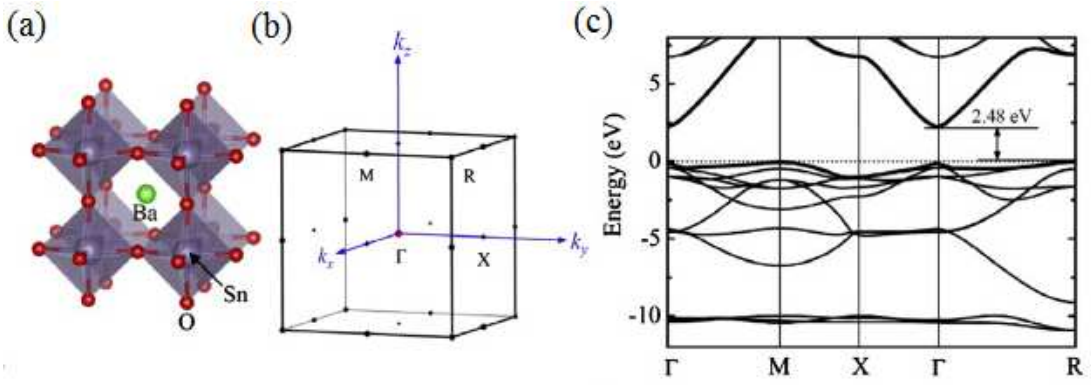

Figure 56: (a) Crystal structure of the $BaSnO_3$. (b) Brillouin zone of cubic $BaSnO_3$. (c) Electronic band structure along the high symmetry point in the Brillouin zone calculated by hybrid density functional theory based on the HSE06 functional [127].

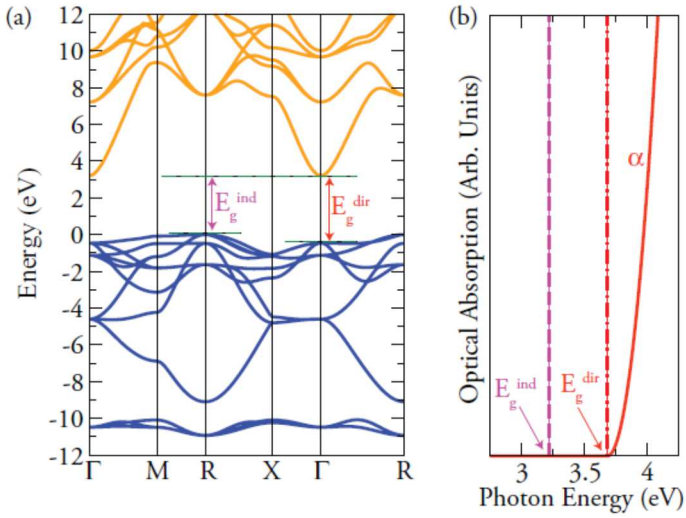

Figure 57: The PBE0 calculated (a) band structure for $BaSnO_3$, and (b) theoretical optical absorption onset of $BaSnO_3$ [126].

The effective mass of the BSO is not well understood. First principal calculations based on different exchange correlation parameters give a wide range of values [129]. It varies from 0.03 to 0.6 m_o values based on the computational and experimental observations [130].

6.6 Applications of BSO

BSO is an attractive option in the family of perovskites for a number of reasons. Most of the perovskite materials are d-band dominated in transport, magnetic and optical properties. This brings diversity in the properties but at the same time these systems are more complicated. From the electronic point of view, BSO is an s-band material. Linear O-Sn-O bonding configuration supports increased electron hopping between neighboring Sn sites. This results into high dispersion in the conduction bands having much higher mobility of the electrons compared to other perovskites.

The potentials of the BSO and doped BSO have been recently explored for the applications in the s-band electronics and hetero-structures [5, 131, 132] with promising results. With the increasing need of flexible electronics, solar cells [133] and other perovskite electronics, an idea of all perovskite based electronics is emerging. Also, the multifunctional nature of the perovskites makes it necessary to find a single platform to integrate different perovskites. The crystal structure of BSO is similar to LAO and STO which makes it more attractive than other perovskite materials.

Other known fields of application of BSO are gas sensors [134, 135] to detect CO and NO_x. Studies have been conducted to find applicability of Ni doped BSO as humidity sensor [136]. Moreover, 2-DEG interface is an active field of research for BSO [137]. BSO has significant advantages over perovskites in such applications. Both

structurally and electronically La doped BSO (BLSO) is stable at high temperatures up to 530 ^{o}C at normal atmosphere and other gases [138]. This makes BLSO an attractive option where many other perovskite oxides show oxygen sensitivity at high temperatures. One example is ZnO often used in TCO applications. The resistivity of ZnO increases by 10^4 times after annealing at 400 ^{o}C [139] limiting its applications at high temperature. Moreover, STO thin films are also sensitive to temperature. Magnetic properties are observed in these films due to the creation of the oxygen vacancies at elevated temperature [140]. Using BSO nanoparticles, highly efficient dye-sensitized solar cells have been fabricated [141]. Strong near-infrared luminescence in BSO has also been reported previously [142].

6.7 Fabrication of BSO

6.7.1 Fabrication of Bulk BSO

There are several studies on the solid state sintered bulk BSO and doped bulk BSO. These samples were polycrystalline and prepared from the SnO and BaO/$BaCO_3$ powders by annealing over 1250 K. Thermal and mechanical properties of these samples were studied by Tekawa et al [143]. Temperature dependent ac properties were revealed by Upadhayay et al [144]. Role of doping by Ca [144], Sb[145] and Zr [146] in the bulk crystal structure, microstructure and electronic properties were reported previously. Bulk BSO has been used to doped Y-Ba-Cu-O to create additional pinning center [147].

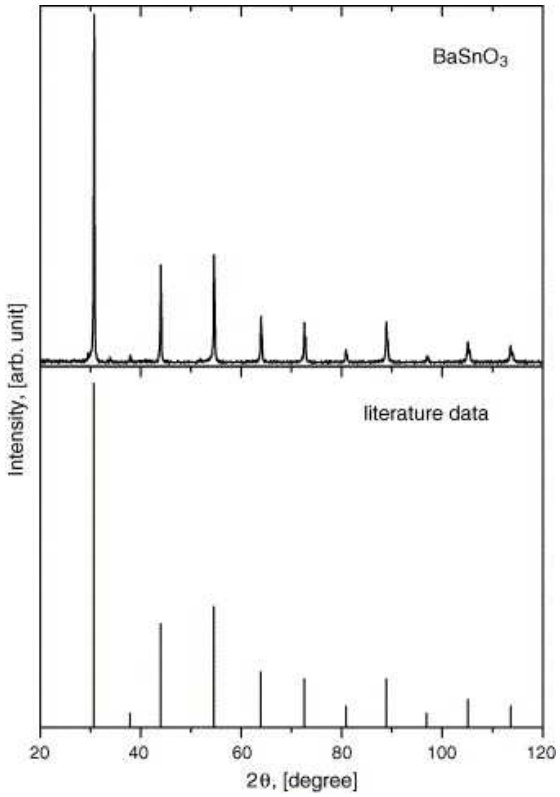

Figure 58: Powder X-ray diffraction pattern of $BaSnO_3$ at room temperature together with literature data (JCPDS card, 15-780 ($BaSnO_3$)) [143]

6.7.2 Fabrication of Single Crystal BSO

There are some reports of growing single crystal BSO by different flux methods [8]. It is observed that flux methods by PbO gives out impurity and changes the chemical nature of the BSO [148]. To eliminate such effects, $CuO+Cu_2O$ had been used by air flux method. In the case of La doped BSO single crystal melted at 1855 C±25 K, electron concentration of 3.3×10^{19} cm^{-3} and mobility of 219 $cm^2V^{-1}s^{-1}$ were reported [149]. In 2012, slightly higher mobility of 320 $cm^2V^{-1}s^{-1}$ was observed by Kim et al [115].

6.7.3 Fabrication of Thin Films of BSO: Processes and Substrates

BSO and doped BSO such as $Ba_{1-x}La_xSnO_3$ thin films are deposited in many different techniques. Among them molecular beam epitaxy (MBE) [150, 151], PLD [8, 152, 153], sol-gel [154], solution processing [155], sputtering [156], etc. are reported. Each technique comes with its own advantages and limitations. MBE is a relatively slow process and controlling the stoichiometry is quite challenging due to evaporation of tin at elevated temperatures in ultra-high vacuum environment. However, by tuning the pressure and evaporation rates, high room temperature mobility as high as 150 $cm^2 V^{-1}$ was reported [150]. Recently, colloidal synthesis of BLSO at low temperature (below 300 ^oC) showed high stability for photo-voltaic applications [157].

PLD is often used by different research groups for BSO and doped BSO fabrications. By varying the laser energy, oxygen pressure, substrate temperature and substrate, it is possible to tune crystallization, growth mode and transport properties. However, the size of the homogenous regions in the film is smaller than other processes.

Both BSO and doped BSO are fabricated on different single crystal substrates such as MgO, STO and LAO. Bulk BSO has a lattice parameter of 4.116 Å (PDF# 15-0780). MgO (a=4.212Å), STO (a=3.905 Å), $PrScO_3$ (a=4.026 Å) and LAO (a=3.82 Å) substrates have a lattice mismatch of 2.3% tensile, 2.1, 5.1 and 7.9% compressive, respectively. Film relaxation depends upon the thickness of the deposited film. The dislocation density increases by increasing lattice mismatch and reduces the mobility. In one case, to reduce the lattice mismatch with the substrate, BSO is used as a buffer layer during BLSO film fabrications [158]. Such techniques are useful to enhance the

mobility of the film as dislocation density and interfacial defects reduce. However, there are other considerations for choosing the substrate such as band-gap of the substrate. In many optical studies, MgO is chosen because of the wide band-gap (7.8 eV) compared to others and transmittance measurements are easier.

6.8 Conclusion

In this chapter, we briefly reviewed the history of perovskites and the importance of the oxide electronics. The crystal structure, band structure, applications and fabrication processes of BSO are described. The role of the deposition processes and choices of substrates to tune the properties of the BSO thin films were detailed.

Chapter 7: Stability of the Oxygen Vacancy in Conducting $BaSnO_3$ Thin films

In this chapter, the fabrication technique of the oxygen deficient BSO and corresponding results will be discussed. Five BSO films were fabricated by gradually reducing the deposition oxygen pressure from 1×10^{-1} Torr to 5×10^{-3} Torr. The BSO films showed gradual transition from an insulating state observed in the sample fabricated at 1×10^{-1} Torr to highly conducting ones with decreasing oxygen pressure. The lowest room temperature resistivity measured was 1.9 mΩ-cm for the sample fabricated at 5×10^{-3}T. Such differences from the original insulating state is contrary to the theoretical predictions. Here, we have explained this phenomenon by showing the presence of the excess oxygen vacancy concentration in the low oxygen pressure deposited samples using XPS. We assume that in-gap states have been created by the oxygen vacancy and excess electrons were contributing in conductivity. Correlations were drawn in-between the oxygen vacancy and the gradual structural changes apart from the electronic properties at low temperatures. Additionally, the stability of these films under high temperature and oxygen pressure were also examined.

7.1 Oxygen Vacancy in BSO: Review of the Computational and Experimental Results

In perovskite materials, the role of oxygen is well recognized due to its impact on the structure and charge balance. Oxygen vacancies in perovskite oxides are known to tune the transport, magnetic and ferroelectric properties of both bulk materials and thin films. In particular, metal-insulator transitions (MIT) have been observed for some

perovskites. Although stoichiometric $CaVO_3$ [159] and $La_{0.66}Sr_{0.33}VO_3$ [160] show insulating behavior, oxygen deficiency induces MIT in these oxides. In case of insulating $SrTiO_3$ (STO), the oxygen deficient $SrTiO_{2.5}$ shows conductivity and semiconducting nature [161]. In another case, metallic $LaNiO_3$ becomes insulator under oxygen deficient conditions [100]. In ferroelectric perovskites, structural phase transitions occur due to oxygen vacancy ordering [162].

The role of the oxygen vacancies is controversial in the field of BSO. Oxygen was considered as a deep donor state for a long time by the computational community. Based on the density functional theory calculations, deep donor states arise from high formation energies [126]. Stoichiometric BSO in both bulk [122] and thin films [151] forms is reported to be an insulator. ARPES has been applied for characterizing the band-structure of oxygen deficient insulating BSO films. An in-gap state at 1.6 eV below the conduction band minimum has been detected in these films. It is assumed that the oxygen vacancy is the source of such in-gap states [123].

In contrast, there are few recent experimental reports about the conducting BSO after post annealing in high vacuum. In one study for gas sensors using bulk BSO, low conductivity is found after heating above 500 ºC. This study used the weight loss to calculate assumed oxygen deficiency. Since these were bulk samples, many other factors such as moisture, water content during sintering, density variations and grain boundary contributions were involved. Moreover, these BSO pellets showed the reversible insulating nature after being cooled down [163]. Although the influence of oxygen deficiency resulting in low conductive nature was not clearly identified, this study necessitates exploring the role of oxygen vacancies in a more controlled

environment. In case of post-annealed BSO thin films fabricated by sputtering on MgO substrate at around 1000 ºC under high vacuum conditions, the samples showed resistivity as low as 5 mΩ-cm from their original insulating state [156]. It was assumed that the conductive nature might arise from the oxygen defects without presenting any explicit evidence.

One established technique to characterize oxygen vacancy is to employ HR XPS of O 1s. Based on the position of the fitted peaks in different binding energies, it is possible to find the signal coming from the stoichiometric region and oxygen vacancy enriched regions. Comparing the integrated area ratios under the components indicate the changes in oxygen vacancy concentration. Such techniques have been used to characterize photocatalytic activity of $SrTiO_3$ [164], resistance switching in amorphous $YFe_{0.5}Cr_{0.5}O_{3-\delta}$ films [165], and thermally stable transparent resistive random access memory based oxide hetrostructure [166]. Here, in BSO studies, similar techniques to systematically study the oxygen deficiency in the BSO films have been applied.

7.2 Oxygen Deficient BSO Film Fabrication

7.2.1 PLD Target Preparation

PLD targets were prepared by mixing a stoichiometric amount of the constituent oxide powders (from Sigma-Aldrich), mortared multiple times, and annealed at high temperature afterwards. The powders were mechanically pressed at high pressures and then the PLD target of 1 inch diameter is prepared by annealing. In the following table, the target powders, and the final processing temperatures are listed. The list also added some compositions that will be discussed in the next chapter.

Table 9: PLD target powders and final processing temperature

Target	Constituent Powder	Final Temperature (ºC)
$BaSnO_3$	BaO & SnO_2	1050
$BaPbO_3$	BaO & Pb_2O_3	700
$SrSnO_3$	SrO & SnO_2	1050
$BaPb_{0.08}Sn_{0.092}O_3$	$BaCO_3$, Pb_2O_3 & SnO_2	750
$La_{0.5}Ba_{0.5}Pb_{0.08}Sn_{0.092}O_3$	La_2O_3, $BaCO_3$, Pb_2O_3 & SnO_2	750
$BaBi_{0.5}Sn_{0.5}O_3$	$BaCO_3$, Bi_2O_3 & SnO_2	750
$LaBi_{0.5}Sn_{0.5}O_3$	La_2O_3, Bi_2O_3 & SnO_2	750

There are some challenges regarding the volatile element based targets such Pb and Bi based ones, and often it takes multiple attempts to reach the exact ratio. In these cases, some extra Pb_2O_3 and Bi_2O_3 powders were used to compensate the evaporation loss. In case of $LaBi_{0.5}Sn_{0.5}O_3$ target, an air tight system made of steel was used to avoid loss due to evaporation. These compositions are sensitive to the target annealing and film deposition temperature.

7.2.2 PLD Deposition Conditions and Post Processing

The BSO films were deposited mostly on the (001)-oriented STO single crystal substrates, and in few cases on (001)-oriented LAO substrates at different oxygen pressures by a 248 nm KrF excimer laser. These substrates (10 mm× 5 mm) were glued to the heater surface with conductive thick silver glue (SPI). For better crystallinity, the samples were deposited at 760 ºC. The substrate holding heater temperature was measured by both the K-type thermocouple and a pyrometer. Every time before the deposition, each PLD target was set for at least 5 minutes pre-deposition to remove contaminants from the target surface. The chamber and connecting gas lines were flushed regularly to minimize the effect of contaminant gases. The PLD chamber was kept at a base pressure of 1×10^{-6} Torr using a turbo-pump. An ac motor regulated

mechanism controlled by a computer was used for target rotation during the deposition. The laser fluence was calculated by dividing the laser energy by the spot size taken on a thermal paper. It was kept at 2 J/cm^2 during fabrication. To ensure a smooth surface of the films and optimum growth, the laser frequency was set at 5 Hz. The distance between the target and the film surface was maintained at 65 mm.

The fabricated sample thickness of the individual films was around 200 nm. It is important to maintain similar thickness in a set of samples during the experiments since the purpose of the study is to compare structural properties and corresponding electronic properties with surface analysis.

The thermal and electronic stability of the BSO films under extreme conditions such as annealing under high oxygen pressures of 5 Torr at 700,760 and 825 ºC were studied. These post-annealed samples were characterized after each annealing and the observed results will be discussed in this chapter. To avoid the repetition of mentioning the samples fabricated at a specific pressure, the samples are designated based on the oxygen pressure used during the deposition and post-processing.

Table 10: BSO sample designation based on oxygen pressure and temperature.

Oxygen pressure (Torr)	Sample Name
1×10^{-1}	S_1×10^{-1}T
5×10^{-2}	S_5×10^{-2}T
2.5×10^{-2}	S_2.5×10^{-2}T
1×10^{-2}	S_1×10^{-2}T
5×10^{-3}	S_5×10^{-3}T
S_5×10^{-3}T annealed at 825 ºC	$Sample_{825C}$

7.3 Characterization of BSO

7.3.1 Structural Analysis

The structure of the BSO thin films were studied by multiple XRD analysis techniques. XRD confirmed that there is no other secondary phase by running θ-2θ scans from 20° to 110° for the S_1×10^{-1}T, S_5×10^{-2}T, S_2.5×10^{-2}T, S_1×10^{-2}T and S_5×10^{-3}T. We observed that the film was growing in the out-of-plane (002) direction only as shown in Figure 58. With decreasing deposition oxygen pressure, the (002) peak shifted toward lower 2θ angles (Figure 59). This indicated that there was a slight increase in the out-of-plane lattice parameter (a_{oop}) with decreasing oxygen pressure. The ideal lattice parameter for cubic BSO is 4.116 Å (PDF# 15-0780). For the highest oxygen pressure deposited sample S_1×10^{-1}T, the a_{oop} was 4.118 Å, very close to the expected value. This value of a_{oop} increased to around 4.122 Å for the S_5×10^{-2} T and S_2.5×10^{-2} T, and finally reached close to 4.137Å for the S_1×10^{-2}T and S_5×10^{-3}T. The science behind such increase in lattice parameter can be explained in terms of the presence of oxygen vacancy. In ABO_3 perovskite structures, strong electrostatic repulsion exists between the cations at A and B sites. Such Columbic repulsion is enhanced by oxygen vacancy sites between the constituent Ba and Sn sites in the BSO [167]. This caused the lattice parameter expansion observed in our experiments. All these films showed a high crystalline nature as we have observed in the FWHM of the film (002) peak. The range of FWHM was confined to 0.05-0.09°. The S_5×10^{-3}T films were annealed at 700 and 760 ºC at 5 Torr oxygen pressure for 1.5 hours, and did not show any change in the peak positon or FWHM. However, $Sample_{825C}$ had slight

increase in the 2θ angle by 0.03º. It resulted in a decrease of the lattice parameter from 4.138 Å to 4.135 Å as shown in Figure 60 (b).

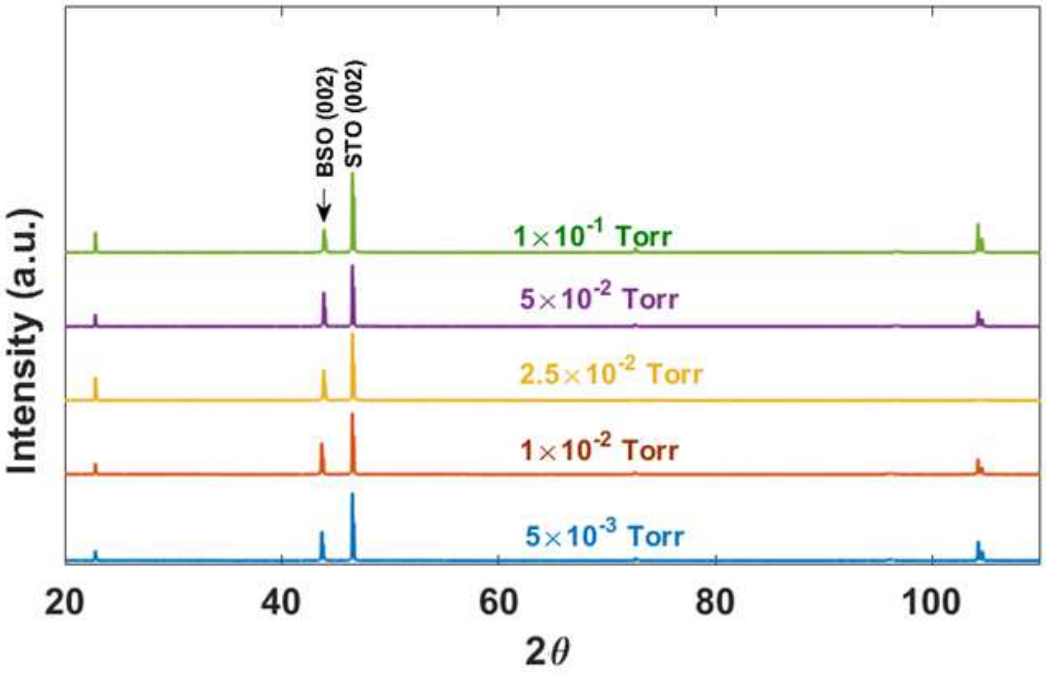

Figure 59: XRD results by the θ-2θ scans of the BSO films deposited on STO substrates at five different oxygen pressures of 5×10^{-3}, 1×10^{-2}, 2.5×10^{-2}, 5×10^{-2} and 1×10^{-1} Torr (from bottom to top) in the range of 20-110°. Each plot is calibrated with respect to the STO peak position.

This result might have come from the oxygen inclusion at some vacant sites inside the original oxygen deficient sample. To make sure the structural stability of other oxygen deficient samples, S_1×10^{-2}T was also post-annealed at 760 ºC. This sample also showed no structural change.

BSO films fabricated at different oxygen pressures were studied by RSM to find in-plane lattice parameters. All the films showed a relaxed nature regardless of the oxygen pressure. The in-plane lattice parameter (a_{ip}) was observed at around 4.106 Å.

Comparing these values, we have concluded that there was a minor increase in the overall lattice volume with the decreasing oxygen pressure as the a_{oop}/a_{ip} increased from 1.001 (S_1×10^{-1}T) to 1.006 (S_5×10^{-3}T).

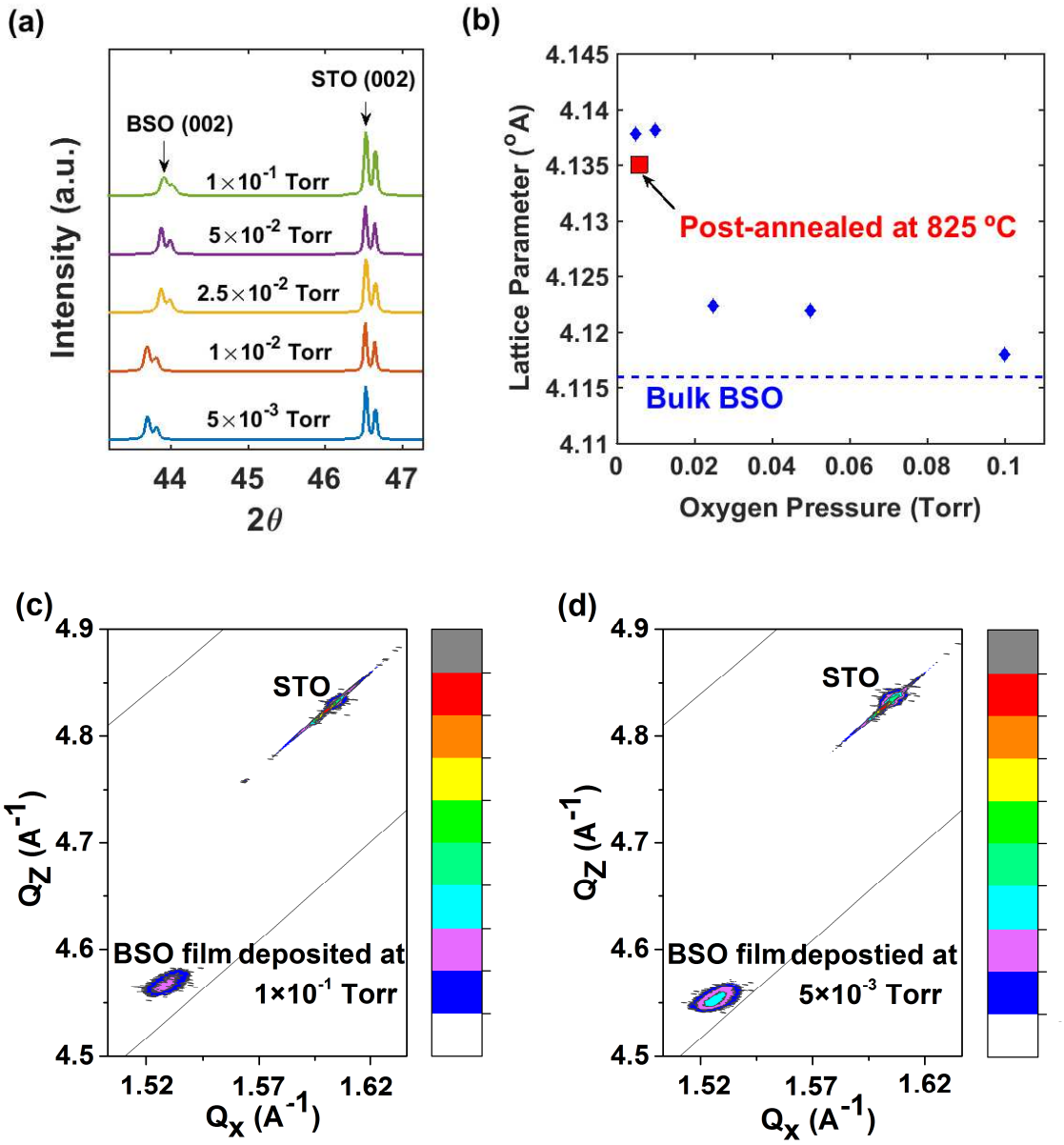

Figure 60: (a) Zoomed region of the XRD consisting of STO (002) and film (002) peaks of the oxygen deposition pressure varying five BSO samples. The oxygen pressure increases in the up-ward directions of the plots [168]. (b) The out-of-plane lattice

parameter of the five BSO films and $Sample_{825C}$ vs. oxygen pressure are plotted after peak fitting the data by the pseudo-Vogit method shown in (a). The heights of the data points resemble the error bar. RSM results of the (103) plane BSO samples deposited at oxygen pressures of (c) 1×10^{-1} Torr and (d) 5×10^{-3} Torr [168].

7.3.2 XPS Analysis

XPS analysis was carried out for all the BSO samples under the same condition and in a single loading to avoid any artefact due to minute changes in the setup. Since we have used Al-source for X-ray generation, the resolution of the data was 0.7 eV. The collected spectrum was calibrated by surface carbon at 284.8 eV. The survey scans did not show any other element other than Ba, Sn and O. O 1s high resolution scans were acquired to compare the relative oxygen vacancy concentration. Experimental data were fitted with 3 different Gaussian-Lorentzian mixed curves. The peak arising from the metal-lattice oxygen is known to appear at the lowest binding energy, i.e. 529.3 ± 0.1 eV. The non-lattice O^{2-} ions at the binding energy of 531.3± 0.15 and 533± 0.15 eV were peak fitted with two other curves. The oxygen deficient regions appeared at the middle at the binding energy of 531.3± 0.15 eV. The highest binding energy peak at 533± 0.15 eV corresponded to the loosely bound oxygen on the BSO film surface, which was relatively weak compared to the other two peaks. By taking the ratio of the integrated areas under the non-lattice and the lattice oxygen peaks ($O_{Non\text{-}Latttice}/O_{Lattice}$), relative oxygen vacancy concentration was calculated for the BSO films. Figure 61 (a) and (b) shows the experimental HR XPS data of O1s, and the corresponding peak fitting for the S_1×10^{-1}T and S_5×10^{-3}T, respectively. The values of $O_{Non\text{-}Latttice}/O_{Lattice}$ for these samples were 0.28 and 0.75, respectively. Therefore, it is evident that decreasing

oxygen pressure significantly increased the oxygen vacancy concentration. To further confirm this assumption, we carried out XPS for the rest of the samples. We found a pattern supporting the inverse relation between the oxygen deposition pressure and oxygen vacancy concentration in Figure 61 (c).

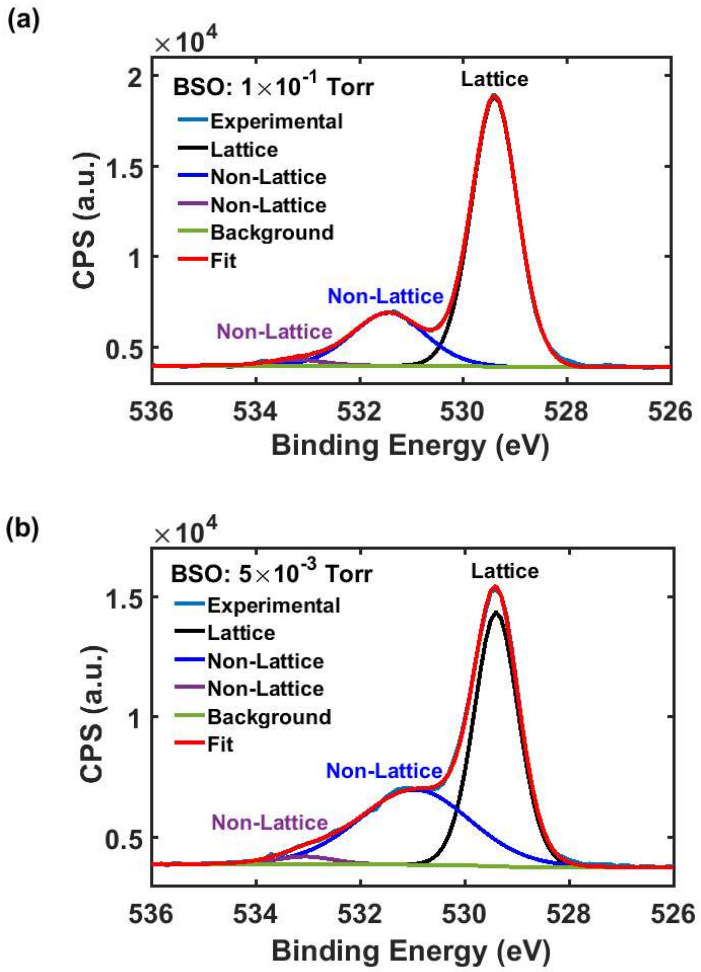

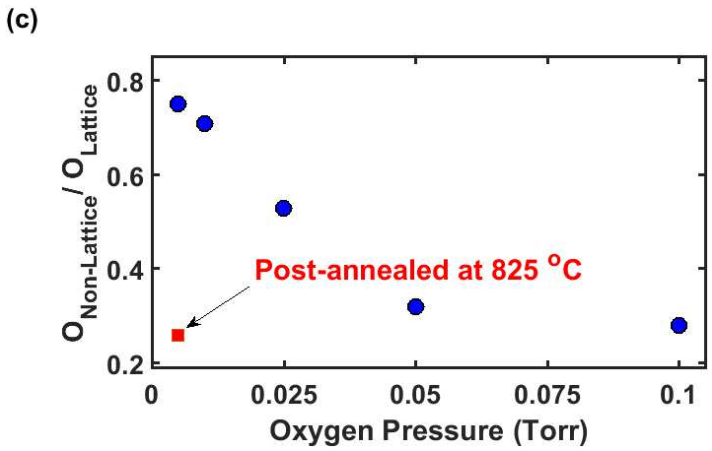

Figure 61: HR XPS of O 1s spectrum of are plotted in (a) S_1×10^{-1}T and (b) S_5×10^{-3}T. The experimental signal was reproduced by a peak fitted with 3 Lorentzian-Gaussian mix at 529.3± 0.1 eV, 531.3± 0.15 eV and 533± 0.15 eV. (c) $O_{Non-Latttice}/O_{Lattice}$ vs. oxygen pressure are plotted for the five fabricated samples and $Sample_{825C}$ [168]. With decreasing oxygen pressure there is a gradual increase in the ratio, and it is much higher for the S_1×10^{-2}T and S_5×10^{-3}T.

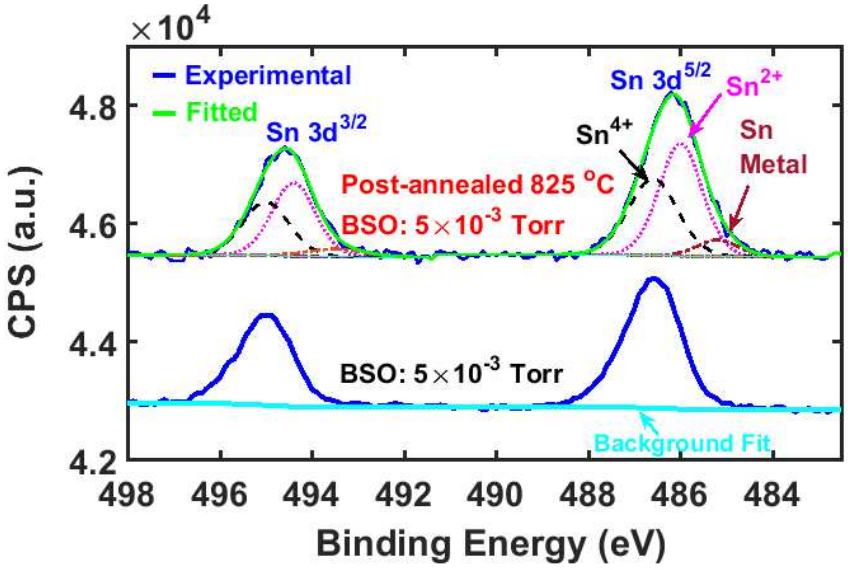

Figure 62: HR XPS of Sn 3d region of S_5×10^{-3}T and $Sample_{825C}$ [168].

To confirm the valence state of Sn, HR XPS of Sn 3d orbital was carried out. Spin-orbit splitting of 8.4 eV and the binding energy of Sn $3d^{5/2}$ at 486.6 eV for all of the fabricated samples were observed. This means that only a Sn^{4+} state exists in BSO film. One of these data sets acquired from the S_5×10^{-3}T is shown in the bottom part of the Figure 62. The post annealed samples (S_5×10^{-3}T and S_1×10^{-2}T) at 500, 700, and then 760 °C under 5 Torr oxygen pressure, did not show any noticeable change in the HR XPS scans of the elements. However, in $Sample_{825C}$, Sn^{2+} (binding energy at 486.0 eV) along with the Sn^{4+} states as of the original samples were observed. The Sn^{2+} and Sn^{0} valence states consisted of the 50% and 7.5% of the Sn 3d fittings shown in Figure 62. Moreover, an overall increase in FWHM of 0.2 eV was found in this sample. The presence of other valence states other than the Sn^{4+} state and wider FWHM are indications of the chemical instability of the films.

After annealing, the Ba $4d^{5/2}$ peak was shifted by 0.3 eV towards the higher binding energy from 779.4 eV in $Sample_{825C}$ (Figure 63). The overall FWHM of the Ba $3d^{5/2}$ peak changed from 2.2 to 1.45 eV due to excess oxidation. The original samples had a peak arising at 780.75 eV from the presence of hydroxylated species. Air exposure of the film surface is the cause of this peak in the BSO samples. This peak disappeared in $Sample_{825C}$, indicating changes on the surface chemistry. From the above discussion it is obvious that $Sample_{825C}$ showed observable differences compared with the fabricated and the samples annealed until 760 °C under 5 Torr oxygen pressure were stable.

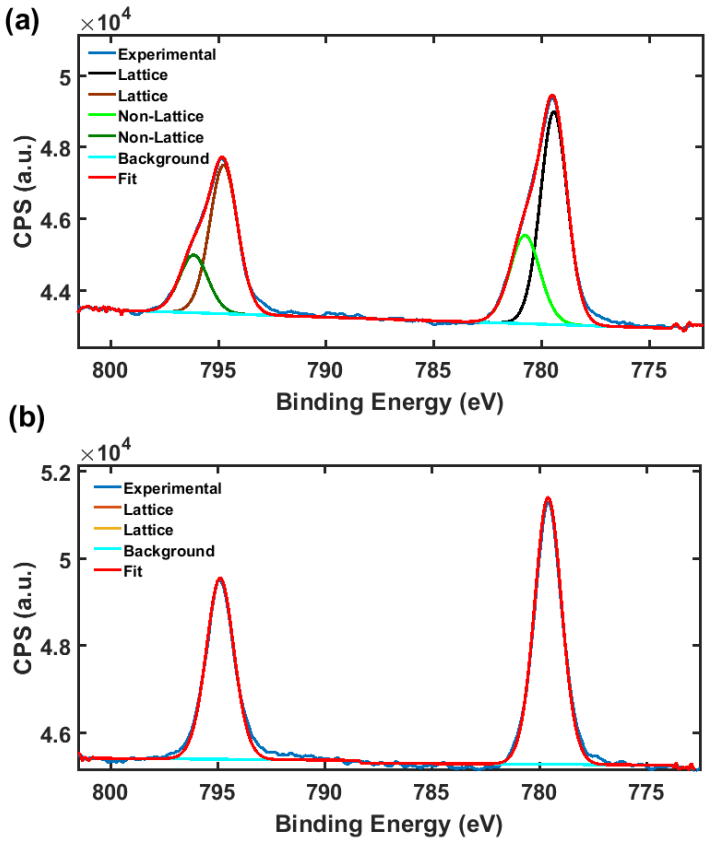

Figure 63: HR XPS of Ba 4d of the S_5×10^{-3}T (a) as fabricated, (b) after annealing at 825 ˚C.

7.3.3 PPMS Results

We have studied the transport properties of the fabricated films by PPMS from 300 K to 1.8 K. The S_1×10^{-1}T showed completely insulating behavior. The room temperature (RT) resistivity of the samples with varying oxygen deposition pressure is plotted with the $Sample_{825C}$ in Figure 64 (a). For S_5×10^{-2} T, RT resistivity was around 10^3 mΩ-cm. With a further decrease in oxygen pressure, the RT resistivity dropped almost exponentially. The minimum resistivity was observed for the S_5×10^{-3}T. The RT resistivity was 1.9 mΩ-cm for this sample.

The temperature dependent resistivity of the BSO films are shown in Figure 64 (b). Semiconductor-like behavior was observed for the S_5×10^{-2} T and S_2.5×10^{-2} T as plotted in the Figure 64 (c) and (d), respectively. The resistivity varied orders of magnitude with the decreasing temperatures in these two samples. The low temperature resistivity of the S_5×10^{-2} T was so high that it surpassed the upper limit of our measurement capability in PPMS configurations. The minima of the resistivity appeared at 2.9 mΩ-cm at 205K and 1.83 mΩ-cm at 90 K in the S_1×10^{-2}T and S_5×10^{-3}T, respectively (Figure 64 (e) and (f)).

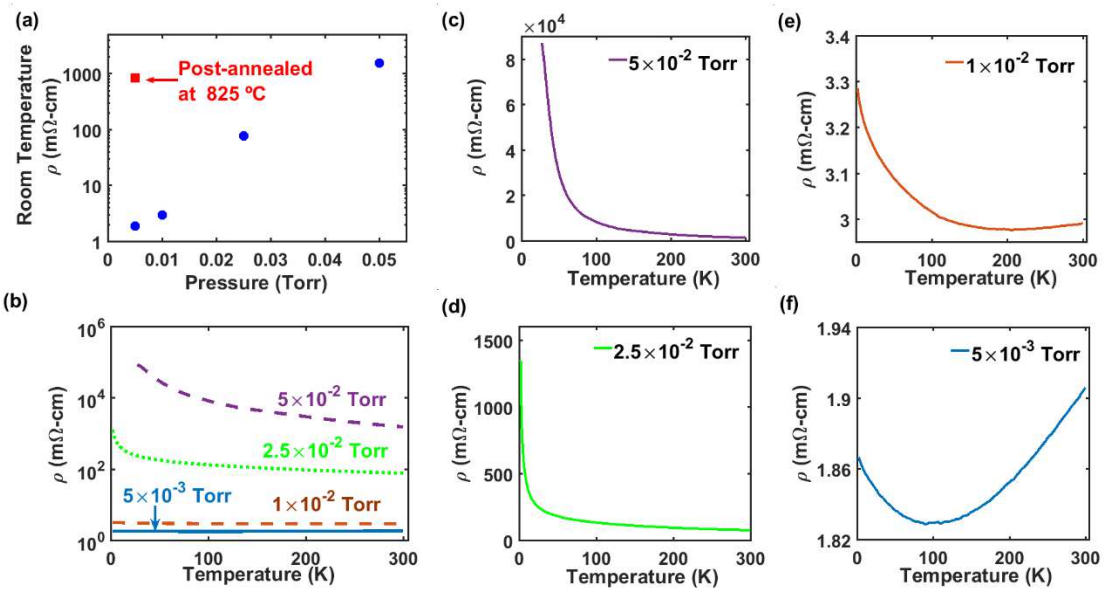

Figure 64: (a) Room temperature resistivity of the BSO films vs. oxygen pressure (Semi-log scale). (b) Temperature dependent resistivity (semi-log scale) of the BSO films measured by PPMS. (c), (d), (e) and (f) are the magnified plots (linear scale) of samples deposited at 5×10^{-2}, 2.5×10^{-2}, 1×10^{-2} and 5×10^{-3} Torr, respectively.

Minute changes in the resistivity were observed with varying temperature for the samples fabricated at low oxygen pressures. Such weak temperature dependence near T=0 K is a signature of metallic like behavior. There were small up-turns in the

S_1×10^{-2}T and S_5×10^{-3}T with decreasing temperature once the temperature minima were reached. Similar metallic like results have been reported on the oxygen deficient BSO samples previously [156], and 4% La and Gd doped BSO samples [169]. These results are more likely to result from the defect scattering rather than the phonon scattering as described in these previous studies.

The induced conduction in the oxygen deficient samples originated from the two excess electrons once the oxygen left the sample. There are studies especially for the BLSO, where the excess electrons from the dopants fill up the lower edge of the conduction band raising the Fermi level. Such phenomenon caused the Fermi level to cross the conduction band. To further support our assumption that oxygen vacancies were the origin of these observed conductions, the carrier concentrations of the S_2.5×10^{-2}T, S_1×10^{-2}T and S_5×10^{-3}T were calculated. At RT, the values of the carrier concentrations were 3.3, 8.22 and 16.5×10^{19} cm^{-3}, respectively. Therefore, we found a gradual increase in the carrier concentration with decreasing oxygen pressure, as expected when the oxygen vacancies are considered as the donor. Considering each oxygen vacancy is leaving two electrons, the vacancy concentrations for S_2.5×10^{-2}T, S_1×10^{-2}T and S_5×10^{-3}T were 1.65, 4.11 and 8.25×10^{19} cm^{-3}, respectively. Dividing the oxygen vacancy concentrations by the number of BSO molecules per unit volume gives the fraction of oxygen vacancies present in each BSO unit cell. This can be used to derive the values of δ in the chemical formula of $BaSnO_{3-\delta}$ for different films. Our calculation gave the chemical formula of $BaSnO_{2.998}$, $BaSnO_{2.997}$ and $BaSnO_{2.994}$ for S_2.5×10^{-2}T, S_1×10^{-2}T and S_5×10^{-3}T, respectively.

The mobility values were calculated from the Hall resistance measurements. One dataset for sample S_1×10^{-2}T is shown in Figure 65. The mobility values of the S_2.5×10^{-2}T, S_1×10^{-2}T and S_5×10^{-3}T are 19, 10 and 2 cm^{2}V^{-1}s^{-1}, respectively. The high resistance of S_5×10^{-2}T barred us from acquiring the data of the Hall resistance data for the S_5×10^{-2}T.

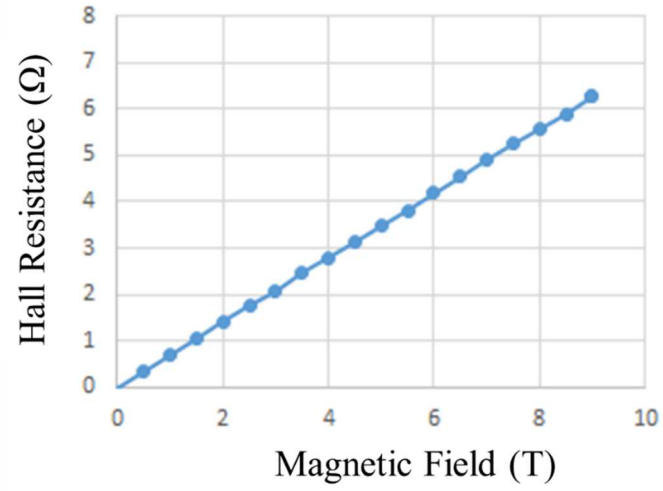

Figure 65: Hall resistance (Ω) vs. magnetic field (T) of S_1×10^{-2}T.

For investigating the electronic stability of S_5×10^{-3}T and S_1×10^{-2}T, films were post-annealed at 760 ºC under an oxygen pressure of 5 Torr. The electronic stability of these samples were confirmed as we observed negligible resistivity changes after 1.5 hours annealing until 760 ºC. However, Sample$_{825C}$ showed very high resistivity. The resistivity increased by three orders of magnitude of the original S_5×10^{-3}T. The $O_{Non\text{-}Latttice}/O_{Lattice}$ became similar to the insulating sample S_1×10^{-1}T.

7.3.4 Stability Studies of BSO on LAO Substrates

To make sure that the observed conductivity was rising from the BSO films alone and was not an artefact from the STO substrate, the low oxygen pressure BSO samples were fabricated over LAO substrates. Under the same deposition conditions as

of STO substrates, two BSO samples on LAO substrates at 5×10^{-3} and 1×10^{-2} Torr oxygen pressures. The observed resistivity for those samples were relatively higher compared to the BSO samples on STO. It was ~1.7 times higher corresponding to the samples on STO. Such results are expected because of the higher concentration of dislocations on LAO originating from the larger lattice mismatch. Our concern was that the high deposition temperature at low oxygen pressure might have modified the STO surface resulting in conductivity. However, this experiment confirmed that regardless of substrates, this conductivity happened in low oxygen pressure deposited BSO samples.

Moreover, annealing of a bare STO substrate was carried out at 5×10^{-3} Torr oxygen pressure and 760 ºC for the same time cycles as done during the deposition of S_5×10^{-3}T. No measurable conductivity was found after this thermal cycles. To make the STO substrate conductive, under high vacuum pressure (1×10^{-5} Torr), the STO substrates were annealed at 675 ºC for 1 hour. Measurable high resistivity of ~300 kΩ was observed for the films. To examine the reversible nature, the same STO substrate was annealed at 675 ºC under oxygen pressure of 5 Torr. The substrate became insulating again. All of the above studies confirmed that the observed conductivity in the BSO films have been originating from the oxygen vacancies in the BSO films alone.

7.4 Applications of the Oxygen Deficient BSO Films

We succeeded in in-situ formation of both an insulating and a conducting state by varying the oxygen deposition pressure in a single step process. Therefore, it is possible to fabricate field-effect transistors (FET) and other perovskite electronics containing both insulating dielectric and conducting channels or electrodes made of

BSO. This gives an opportunity to avoid any other dopants or surface termination. Previous studies of the oxygen vacancy induced conduction by post-annealing at ~1000 ^{o}C has severe limitations due to too high temperature which can impact both the other perovskite materials and other circuit elements in a device. Many of the other perovskites are more sensitive to oxygen vacancy and high temperature compared to BSO. Therefore, using the same BSO for different layers in the electronic devices can reduce the effect of the interfacial defects. It also solves the challenges regarding the strain from the multi-layers.

7.5 Future Studies

Fabrication of FET and other microelectronic circuits with an insulating BSO and a conducting BSO channel will be useful to evaluate both the performance and the limitations of the oxygen deficient films. It is also important to conduct studies on the diffusion of gases in the films in atmospheric conditions for a prolonged period. If exposure to atmosphere causes variations on the transport properties, possible diffusion barriers need to be identified. Studies can be conducted to find the role of the device operating temperature under many cycles of operation.

7.6 Conclusion

In this chapter, the role of oxygen vacancies in inducing conductivity in the BSO samples fabricated by PLD was discussed. By gradually reducing the oxygen pressure during the deposition, a gradual decrease in the resistivity from the original insulating state was observed. BSO films deposited at 5×10^{-3} Torr showed the lowest resistivity (1.73 mΩ-cm). The a_{oop} increased with decreasing oxygen pressure. These results were explained on the basis of the presence of the oxygen vacancy concentration

as revealed by XPS. The conductivity in BSO was stable up to the deposition temperature of 760 ºC and independent of the choice of substrates. These findings are important for the all perovskite FET devices. Moreover, for TCO based applications and energy applications such as solar cells, the compatibility of oxygen deficient BSO films can be studied in future.

Chapter 8: Band Gap Engineering of $BaSnO_3$ via Chemical Substitutions

In this chapter, we have discussed the tuning of the opto-electronic properties by modifying the chemical nature of BSO. The effects of chemical substitution in BSO thin films by multi-valent elements such as Sr, Pb and Bi are discussed. A combinatorial synthesis technique was applied for fabricating composition gradient thin films. The elemental, structural, electronic, and optical properties of these compositions were studied by WDS, XRD, PPMS and UV-vis spectroscopy, respectively. The experimental data was correlated with the DFT simulation (ACBN0 approach) carried out by our collaborators to explain the results.

8.1 Review of BSO Doping

To enhance the electronic and optical properties and induce magnetization, there are many reports on the doping of pure BSO. Both n and p-type doping are studied at two different sites (Ba and Sn) of BSO. BLSO is the most known and well-studied case in this field by various fabrication techniques. For BLSO, the highest conductivity (10^4 S cm^{-1}) with high mobility (120 cm^2 V^{-1} s^{-1}) was achieved by the MBE deposition [3]. The effects of La doping on the transport and optical properties in BSO is shown in Figure 66 and Figure 67. Because of measuring the direct optical band gap, the Tauc plot in Figure 67 (a) used $(h\nu\alpha)^2$ vs. photon energy ($h\nu$).

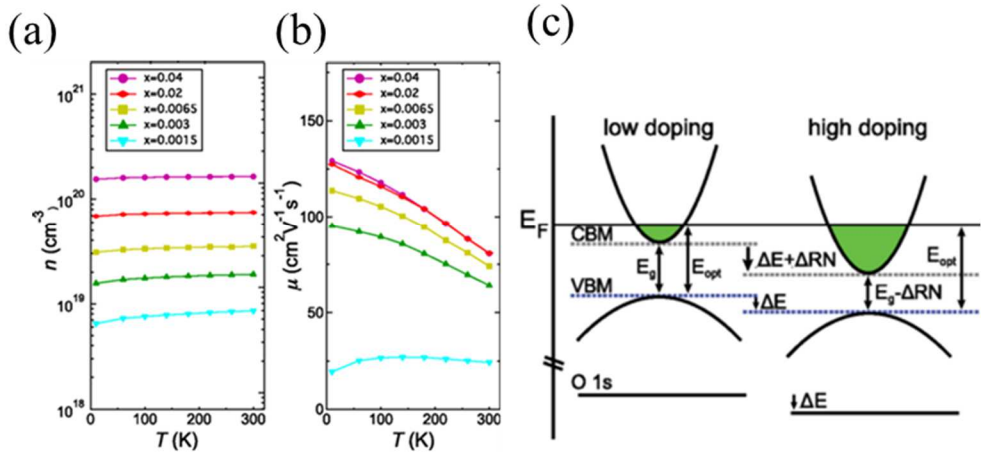

Figure 66: Temperature dependent (a) carrier concentration and (b) mobility of the $Ba_{1-x}La_xSnO_3$. (c) Schematic of the Moss-Burstein shift observed with La doping. Doping shifts the orbitals with respect to the Fermi level (E_F), increasing the optical gap (E_{opt}). The band gap renormalization (ΔRN) results from the lowering of the conduction band minimum (CBM) [170].

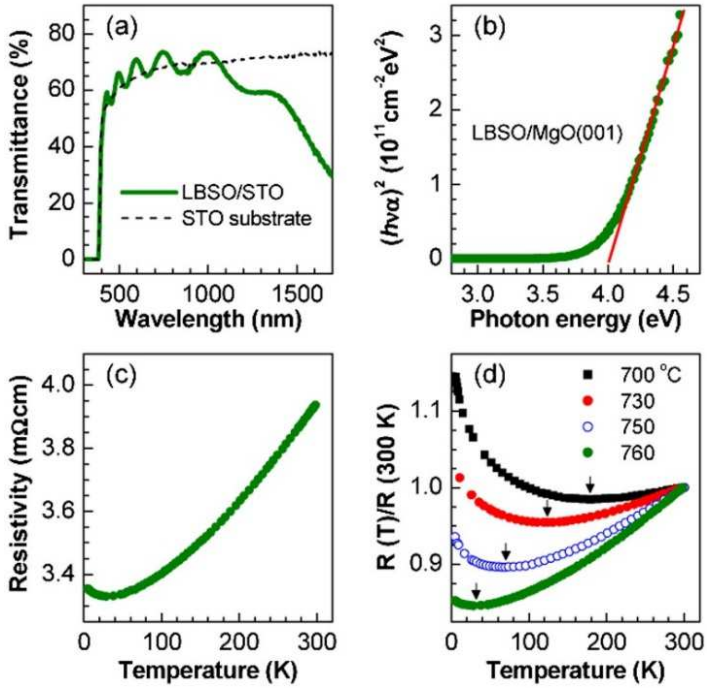

Figure 67: a) Optical transmission spectra of pure STO substrates and the BLSO/STO(001) films. (b) $(h\nu\alpha)^2$ vs (hv) plot of the LBSO/MgO(001) film. (c) R-T

curve of BLSO/STO(001) films deposited at 760°C, (d) Normalized Resistivity vs. Temperature (K) [171].

Because of the higher mobility of electrons compared to holes, n-type dopants are preferred. High electron mobility in BSO originates from the lower electron effective mass and electron-scattering rates as discussed on page 90. Both the deposition temperature and doping concentration impact the transport and optical properties. Besides, there are reports on the magnetic and ferroelectric properties by Fe [121], Gd [172] and Te [172] doping, respectively. In the following table, some of the dopants, their preferred sites (A/B), fabrication methods, characterizations and references are summarized.

Table 11: Chart of the dopants of BSO with their preferred sites in ABO_3 structure, fabrication methods, and functionalization.

Dopant	Method	Functionalization	References
La (A)	MBE	Optical & electronic (OE)	[3]
	PLD	OE	[8, 152, 153]
	Sol-gel	OE	[154]
Sb (B)	PLD	OE	[173]
Fe (B)	PLD	OE & magnetic	[121]
Te (B)	Ceramic	Electronic & ferroelectric	[172]
Gd (A)	PLD	OE & magnetic	[169]
Nb (B)	PLD	OE	[174]
Mn (B)	PLD	OE & magnetic	[175]

Moreover, doping induces different types of point and interface defects [126]. Strain is induced both by the substrate and elemental doping affecting the bandgaps and optical properties [128]. Differences in the ionic radius contribute to the structural distortions as well as the rotation of the bonding. Volume of the cubic BSO unit cell

changes based on the level of doping concentration, and often creates pseudo-cubic structures.

8.2 Chemical Substitutions of BSO by Sr, Pb, and Bi

For TCO and device applications, it is important to find the role of unknown elements in BSO in tuning bandgaps and electronic properties. While Sr is an alkaline earth metal, Pb and Bi are heavy metals with complicated electronic structures. In the wide ranges of compositions, there are possibilities of the elements to be distributed in different sites based on their valence states and structural stability. Therefore, in this chapter, we will focus on the experimental results of the Sr, Pb and Bi substitutions in BSO with the support of theoretical calculations.

The combinatorial thin films were fabricated on the LAO and MgO (001) substrates of 10 mm × 5 mm size. The PLD chamber background pressure was maintained at ~ 3×10^{-7} Torr, and the deposition oxygen (purity 99.999 %) pressure was kept at 50×10^{-2} Torr. The temperature during the PLD deposition for BSO-$SrSnO_3$ (SSO) and BLSO-SSO were 760 ^{o}C. The Bi and Pb based samples were deposited at 600 ^{o}C to avoid evaporation of these volatile elements. The laser energy was 50 mJ per pulse, and laser was shot at a frequency of 5 Hz. The thickness of the films were measured by profilometer and SEM. Each spread film was over 9 mm long in the composition gradient direction and the thickness of these films was almost 100 nm from end to end. In each cycle, using both A and B targets in our combinatorial PLD deposition system, the thickness was kept around half of the unit cell (0.21 nm). The following table summarizes the conditions used for the combinatorial synthesis of the thin films in this chapter and the next one.

Table 12: PLD targets and the deposition temperatures

Target A	Target B	Deposition Temperature (°C)
$BaSnO_3$	$SrSnO_3$	760
$BaSnO_3$	$BaPbO_3$	600
$BaSnO_3$	$BaBiO_3$	600
$La_{0.07}Ba_{0.93}SnO_3$	$SrSnO_3$	760
$BaPb_{0.1}Sn_{0.9}O_3$	$La_{0.5}Ba_{0.5}Pb_{0.1}Sn_{0.9}O_3$	600
$BaBi_{0.5}Sn_{0.5}O_3$	$LaBi_{0.5}Sn_{0.5}O_3$	600

The fabricated films appeared like the schematics shown in Figure 68. Both end points of the substrates were pure phases of the BSO and the dopant target.

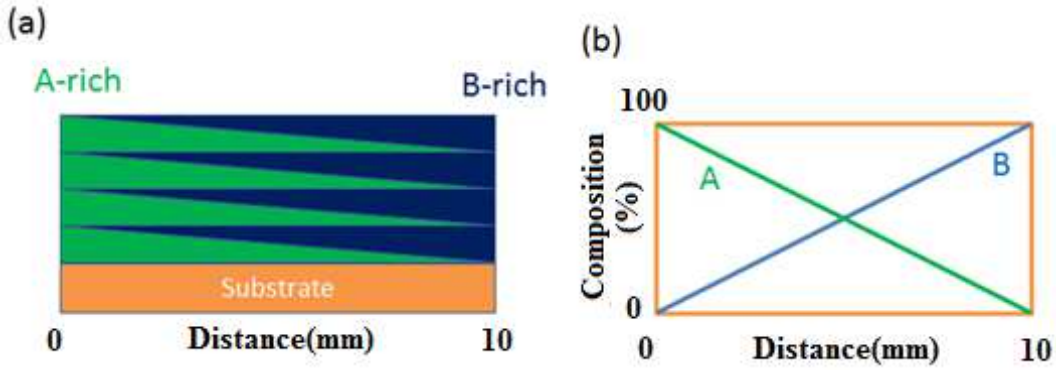

Figure 68: (a) Combinatorial thin film after deposition. (b) The profile of the composition gradient of two phases A (BSO) and B (dopant target).

8.3 Results

8.3.1 Sr-Doped BSO Combinatorial Films

The structural and optical experimental data of the Sr-substitution up to 50% composition are shown in the Figure 69. The XRD data shows the linear decrease in the out-of-plane lattice parameter with increasing Sr concentration in Figure 69 (a). This is a case of iso-valent substitution at A site where Ba is replaced by Sr. The ionic

radius of Sr^{2+} is 144 pm, slightly smaller than the Ba^{2+} (161 pm). Therefore, the observed results of lattice parameter reduction is expected. Moreover, the band-gap of pure $SrSnO_3$ is around 3.93 eV. Therefore, increasing Sr concentration in BSO is expected to increase the band-gap as observed in Figure 69 (b). The bandgaps shown in the Figure 69 (b) were derived from the slope of the Tauc-plot in the linear region shown in the Figure 69 (c). The arrow in the figure indicates the direction of the increasing Sr concentration. The absorption edge shifted gradually towards the higher energies with increasing Sr. The monotonous shift resulted into higher bandgaps with the increasing doping. Volume change due to the iso-valent substitution by smaller ions distorted the ideal octahedral and tilted the bonding angles of BSO [176]. Therefore, a corresponding increase in the bandgap was observed due to the increasing level of hybridization. The theoretical values showed similar patterns and computed bandgap values were within 10% of the experimental results [120].

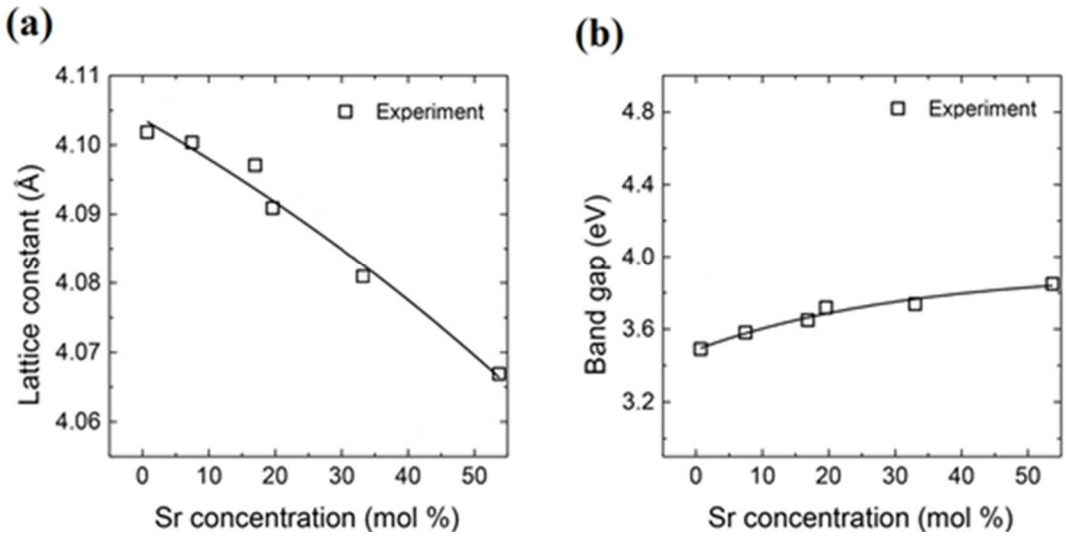

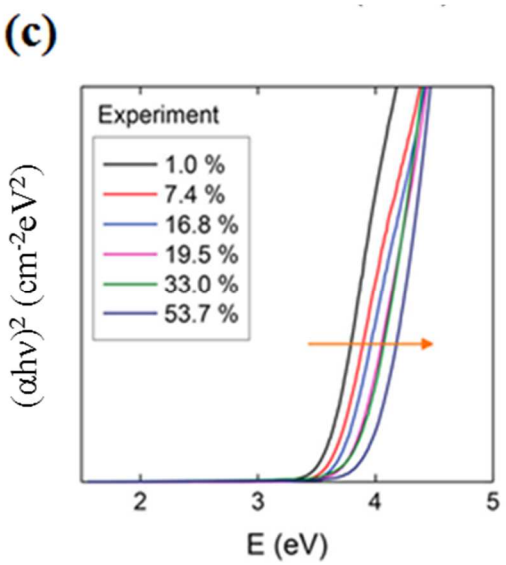

Figure 69: Experimental results of (a) the lattice constant, (b) the band-gap of Sr doped BSO, (c) Tauc-plot of Sr substituted BSO samples [120].

8.3.2 Pb-Doped BSO Combinatorial Films

The Pb substitution of BSO showed site preference based on concentration and multi-valent states. Comparing the theoretical calculations to our experimental results of the XRD, it appears that Pb^{4+} replaces Sn^{4+} at B-site. The theoretical values showed similar trends within 1% variations from the experimental data. The ionic radius of the Pb^{4+} (77.5 pm) is slightly higher than the Sn^{4+} ion (69 pm). Therefore, an increase of the lattice parameter is expected. Individual composition films were made to verify the combinatorial results. The XRD data was reproducible in the case of single films. The RSM plots of these films showed relaxed behavior on LAO substrates. However, the experimental bandgap results complicated this simple interpretation of substitutional site distribution at B-site alone. The optical bandgap showed non-monotonous shifts with increasing concentrations of Pb. Such results required detailed understanding of the band-structure of the individual target materials used.

The pure $BaPbO_3$ (BPO) shows semi-metallic nature with a band gap of 1.8 eV due to the strong overlap of the conduction band (Pb 6s) and valence band (O 2p), and compensating structural relaxation [177]. Therefore, in case of just B-site substitution in BSO-BPO compositions, the bandgap with increasing Pb is supposed to be lower as shown by the theoretical calculation in Figure 70 (b). However, the experimental result showed an upturn in the bandgap after 20% Pb concentration. Such behavior is not possible to explain just considering the B-site substitution. In case of partial substitution of the Ba^{2+} at A site by Pb^{2+}, the slightly smaller ionic radius of Pb^{2+} (144 pm) compared to Ba^{2+} (161 pm) will compensate the increase of lattice parameter by B-site substitution. Moreover, hypothetical cubic $PbSnO_3$ has a band gap of ~4 eV that might contribute towards the increasing bandgap over 20% Pb concentration. To confirm the valence states of Pb, XPS was carried out for two single films of 14 and 30% Pb concentrations. The HR XPS of the 4f orbital showed more asymmetry in case of 30% Pb sample with an additional peak around 0.75 eV apart from the Pb^{4+} state at 137.5 eV. This additional peak at 138.2 eV is a signature of the presence of the Pb^{2+} state. Therefore, we can conclude that increasing Pb concentration leads to mixed valence states of Pb^{2+} and Pb^{4+} at both A and B sites of BSO which resulted in the nonmonotonic behavior of the band gap. The tilting distortions of bonding due to Pb ion substitutions at two different sites simultaneously complicate the theoretical calculation of the bandgap and lattice parameter.

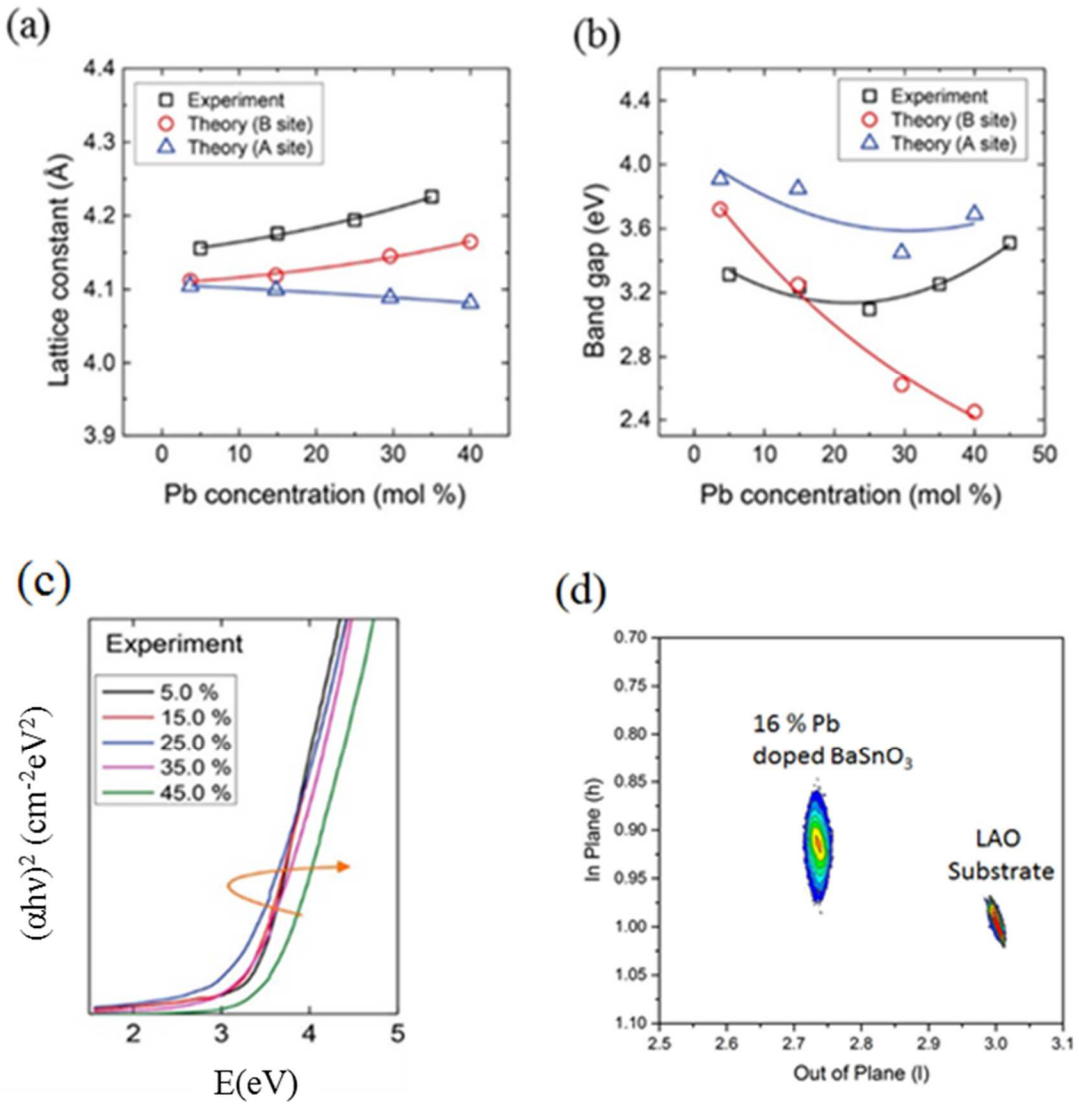

Figure 70: Experimental and theoretical values of (a) the lattice constant and (b) the band gap of Pb-substituted BSO. (c) Experimental Tauc plots of Pb-substituted BSO [120]. (d) RSM plot of the (103) plane of 16% Pb doped BSO on LAO substrate.

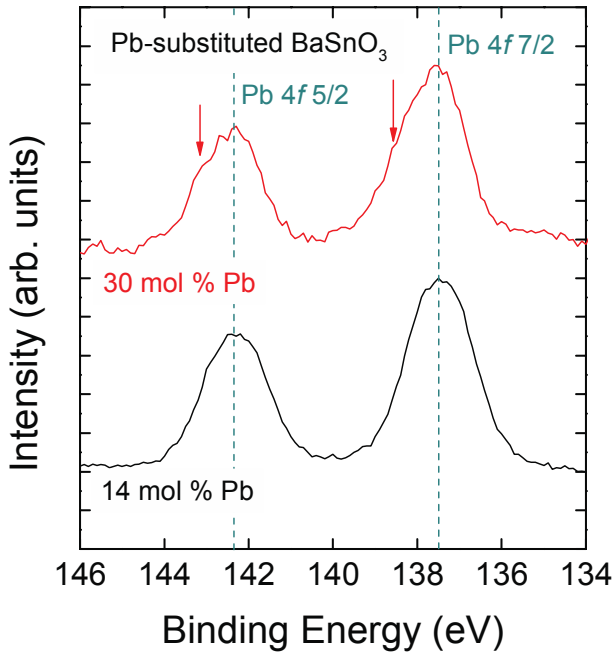

Figure 71: HR XPS of Pb 4f of Pb-substituted $BaSnO_3$ thin films. Two different Pb concentrations of 14 mol % (bottom) and 30 mol % (top) are plotted. The red arrows indicate additional peaks superimposed, which implies the presence of the mixed valence state of Pb ions [120].

8.3.3 Bi-Doped BSO Combinatorial Films

The combinatorial films of Bi doped BSO were fabricated using BSO and $BaBiO_3$ targets. The $BaBiO_3$ crystal structure is more complicated than the other ones discussed previously. Although from the chemical formula it appears that the Bi has 4+ valence state, in neutron diffraction experiments 3+ and 5+ states are observed. The valence state is also sensitive to the oxygen stoichiometry [178]. In case of the Bi^{4+} state alone, metallic behavior is expected to originate from the half-filled Bi 6s state. However, semiconducting behavior with a bandgap of around 1.8-2 eV is reported due to the titling and octahedral breathing, and such gaps are supported by theoretical

calculations [179]. There are also reports of the Bi valence ordering in these cases. Moreover, the presence of the multivalent states contribute to the distortion of the ideal cubic crystal structure of $BaBiO_3$ which makes the unit cell double of the theoretical cubic structure. This can explain the semiconducting behavior instead of the metallic behavior [180]. In such geometric configuration and disproportionate charges, the overlap of Bi 6s and O 2p is significantly reduced, and stable semiconducting behavior is observed with high level of doping in case of in $BaPb_{1-x}Bi_xO_3$. There are also reports of clustering like behavior rather than uniform distributions of the Bi ions when a high percentage of the Bi is present in $BaPbO_3$ [181].

The ionic radius of both Bi^{3+} and Bi^{5+} are bigger than the Sn^{4+}. Therefore, the observed increase in the lattice parameter (Figure 72 (b)) in our combinatorial film with increasing Bi content is expected. We did not observe conductivity for the fabricated compositions. The insulating nature supports distorted perovskite structure assumptions with the possibility of the mixed valence states. With increasing Bi up to 10%, the bandgap showed negligible effects although the lattice parameter increased which might be attributed to the initial random substitution at B sites shown in Figure 72 (c). Afterwards, the band gap continuously decreased up to 40% concentration. We observed the continuous red shift of the absorption edge with increasing Bi doping. An in-gap state below 3 eV was observed both in the experimental and theoretical calculations which might rise from the Bi clustering effect as shown in Figure 72 (e) and (f). Also, the clustering of Bi was also found to be energetically favorable than the non-clustered ones by theoretical calculation [120]. Therefore, we can conclude that in

the BSO-$BaBiO_3$ combinatorial films, clustering of Bi-atoms was reducing the bandgaps and increased the lattice parameter at high concentrations.

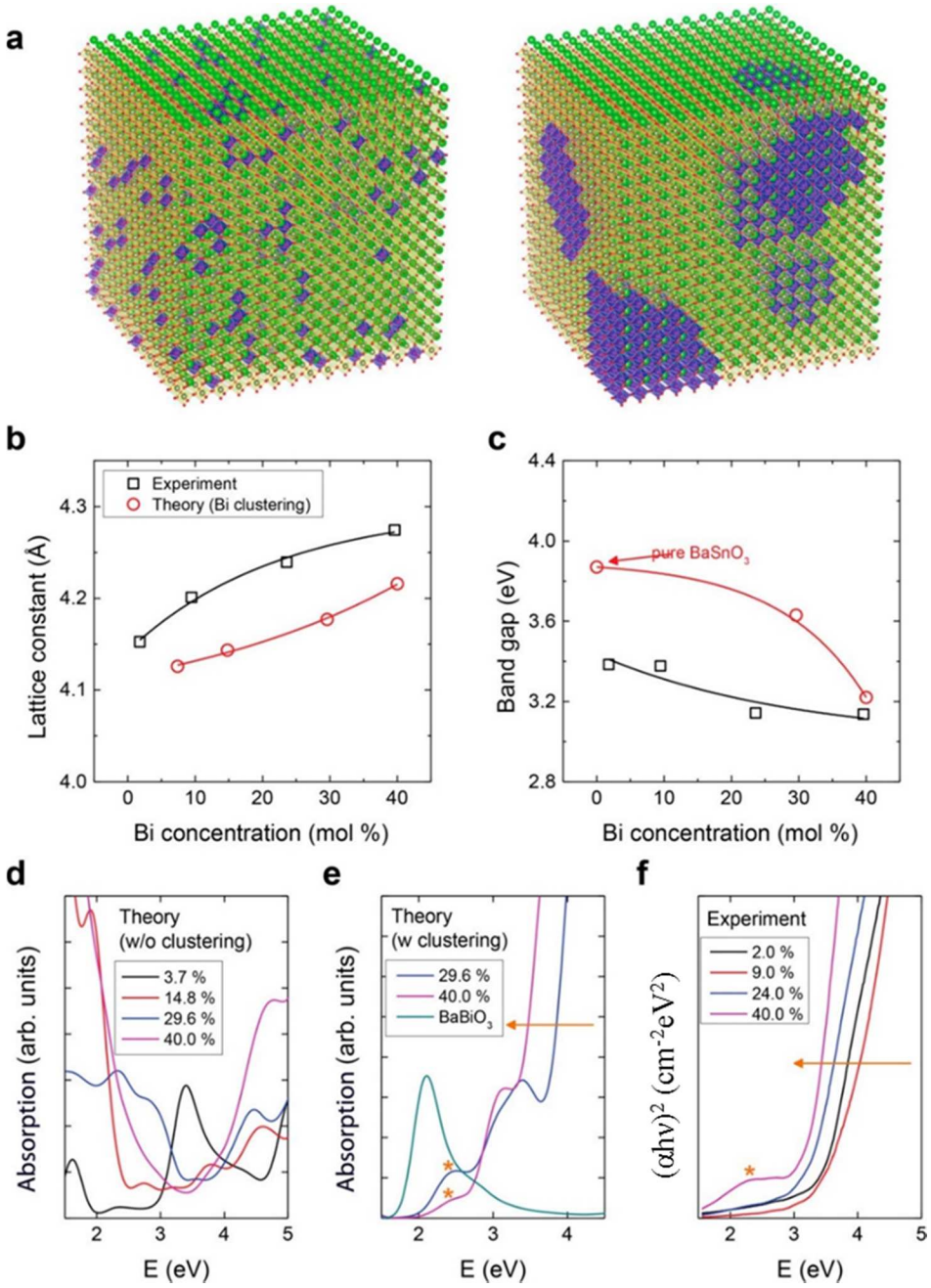

Figure 72: (a) Theoretical random distribution of the Bi ions in $BaSnO_3$ (left) and formation of clusters (right). Experimental and theoretical values of (b) the lattice

constant and (c) the band gap of Bi-substituted $BaSnO_3$. Theoretical absorption spectra of Bi-substituted $BaSnO_3$ as a function of Bi concentration in (d) uniform and (e) a cluster distribution, respectively. (f) Experimental $(\alpha h\nu)^2$ plots as a function of photon energy (E) (units of mole percent). The asterisk indicates an additional absorption peak below the band gap energy. The asterisks in panels (e) and (f) indicate the in-gap state, and it is consistently observed in the experimental absorption and theoretical absorption with the Bi clustering model [120].

8.4 Future Studies

For future research, we suggest certain experiments to examine the arrangements of Pb and Bi atoms in detail. One possible way is to investigate them using atomic resolution TEM. SADP might distinguish the effects of substitutions rising from the strain and clustered regions. Another method is to utilize EELS to individually probe atomic bonding. PCA analysis might be used to remap the EELS regions based on the different Pb and Bi-bonding signal to identify site locations of the Pb, and the random and clustered Bi-atoms. ARPES can be applied to image the band-structure and get a clearer picture of the in-state bandgaps observed in the optical bandgaps. Moreover, the role of the defects formed during A and B site substitutions and their impact on the bandgap can be studied.

8.5 Conclusion

In this chapter, the role of substitution by multivalent state elements such as Sr, Pb and Bi in the BSO were discussed. It is found that the band gap of BSO can be tuned from 3 to 4 eV by chemical substitution using these elements. The results present complex physics in tuning optical bandgaps and structural modifications in the BSO

systems based on the substituting elements. While Pb distribution in A and B sites were dependent upon concentration and show non-monotonic bandgaps, Bi addition in larger concentrations created clusters of Bi showing in-gap states. These studies can be applied for the future studies in BSO and similar complex oxide perovskites for predicting band-gap and structural distortions.

Chapter 9: Search for Superconductivity by Carrier Injection and Strain Engineering

In this chapter, we attempted to induce superconductivity by carrier injection and creating multi-valent states in the Sr, Pb and Bi substituted BSO samples. Based on the optimum conditions for the compositions discussed in the previous chapter, La doping was carried out to investigate the impact of increased carrier concentration on the transport properties. Moreover, we have studied the role of the lattice strain of BLSO on LAO substrate to induce tetragonal distortion.

9.1 Possible Superconductivity

In addition to the optical and functional properties, we searched the superconducting properties of BSO for several reasons. The lattice parameter of BSO closely matches with the substrates available such as MgO and STO, can be integrated with other perovskites, and the device applications of BSO based materials are prominent. While many of the high T_C superconductors are highly anisotropic such as YBCO and non-cubic, superconductivity in nearly cubic structure is highly desirable. In the case of BSO, there are certain aspects of bonding and band structure similar to other superconductors such as Bismuthates and doped TCO which motivated us to search for superconductivity in chemically substituted and strained BSO.

One of the reasons for the interest in BSO originates from the presence of the Sn 5s – O 2p (conduction and valence bands) similar to hybridized Pb 6s – O 2p and Bi 6s – O 2p orbitals in $BaPb_{1-x}Bi_xO_3$ (BPBO) [177] and $Ba_{1-x}K_xBiO_3$ (BKBO) [182], respectively. For BPBO and BKBO compositions, the highest transition temperatures

are 13 and 34 K, respectively, which are surprisingly high for bad metallic oxides. Although these materials were discovered almost 30 years ago, the exact mechanism of superconductivity is still under debate. Due to the complexity of atomic bonding, phases and charge distribution, the bismuthate family is often referred as "the other high-temperature superconductor"[183]. However, it is expected that both charge disproportion and tetragonal phase with increasing doping of elements cause superconducting transitions. In these bismuthates, a competing charge-ordered phase exists [184, 185]. It is assumed that a frozen distortion of the Bi–O octahedra creates a charge-disproportionated charge density wave (CDW) state [183]. The origin of such disproportionated CDW traces back to the multi-valent states of Bi^{3+} and Bi^{5+}. Variable bonding lengths have been reported due to the presence of CDW. Because of the presence of K atoms in BKBO, long range structural distortions are observed by a tilt of the BiO_6 octahedra [186]. Moreover, partially filled s-orbital is also supposed to be one of the factors for superconductivity.

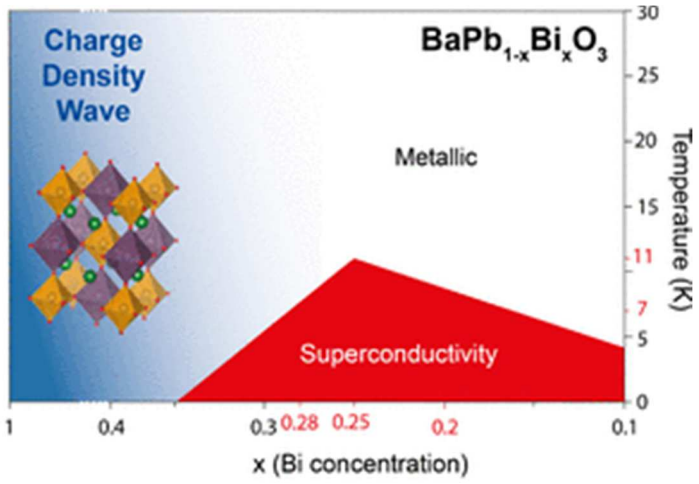

Figure 73: Schematic temperature-doping phase diagram of $BaPb_{1-x}Bi_xO_3$ [187]. The CDW and superconducting phases are colored in blue and red, respectively. In the

crystal structure of $BaBiO_3$, two distinct Bi sites, are surrounded by oxygen octahedra with different Bi – O bond lengths (yellow and violet), and Ba ions (green circles).

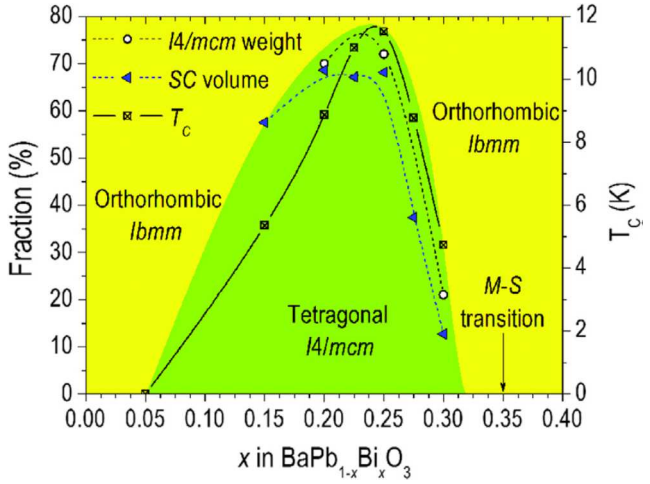

Figure 74: Variation of T_c, superconducting volume and relative amount of phases are shown in $BaPb_{1-x}Bi_xO_3$ [188]. Superconductivity exists only in tetragonal phase, and T_c increases with tetragonal phase fraction.

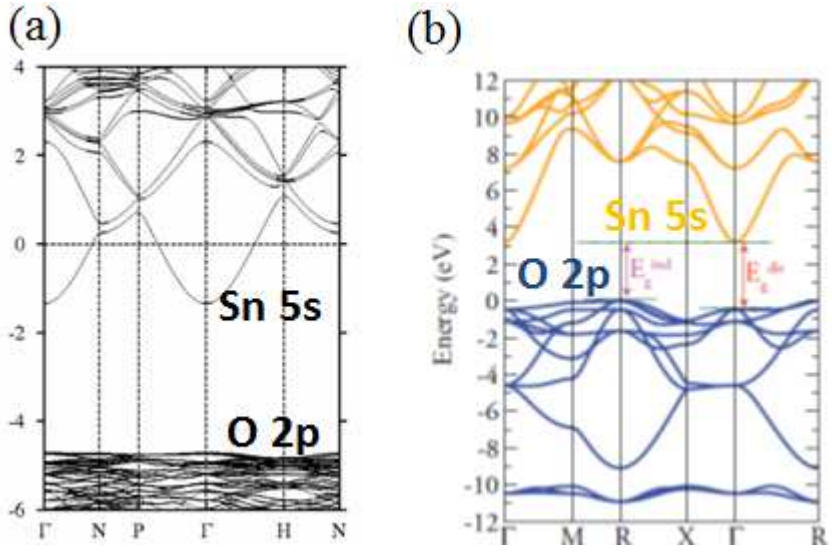

Figure 75: Band-structure of (a) ITO [189] and (b) BSO [126].

In the case of BSO, insulator to conducting state transition happens with La doping creating partially filled Sn 5s band. In the previous chapter, we also found the

existence of multivalent states in case of Pb and Bi substitutions in BSO at higher concentrations. Such charge distributions and tetragonal distortions in these Sr, Pb and Bi substituted BSO compositions might show superconducting properties with optimum carrier concentration. Therefore, we added La in these substituted BSO compositions to investigate the low temperature electronic properties and superconductivity. Increasing La concentration is expected to create additional lattice distortion, insulator-conductor transitions and modify the band gaps, which might facilitate Cooper-pair formation for certain compositions.

Moreover, transparent materials such as doped ITO has previously shown superconductivity. In the case of Na and Zn doped ITO, reversible superconductivity was observed up to 5 and 3.3K, respectively [190, 191]. Both ITO and BSO have similar band structures with highly dispersive s-bands shown in Figure 75, which makes electron doped BSO an ideal candidate for superconductivity.

9.2 Results

We injected excess n-type carriers by La in Sr, Pb and Bi substituted BSO films. The substitution of Ba^{2+} by La^{3+} is supposed to give one excess electron for each substitution. The low temperature properties were measured from room temperature to 1.8 K using the PPMS system.

9.2.1 Combinatorial Films of $(La_{0.07}Ba_{0.93})SnO_3$-$SrSnO_3$ (SSO)

Since BSO-SSO films were insulating, we investigated $(La_{0.07}Ba_{0.93})_{1-x}SnO_3$-$Sr_XSnO_3$ compositions in combinatorial systems to find the role of excess n-type carriers originating from La. We fabricated these films on MgO substrates at 760 ^oC at 1×10^{-1} Torr to maintain the high crystalline quality. The relative Sr concentration

(Sr/(Sr+Ba+La)) along the film, and out-of-plane lattice parameter vs. relative Sr concentration are shown in Figure 76. The Sr substitution increased at A-site almost linearly with positon. Sr substitution also decreased the lattice parameter almost linearly from 4.11 Å (pure BLSO) to 4.03 Å (90% Sr substitution). The room temperature resistivity showed conducting to insulating transition with increasing Sr concentration at $(La_{0.07}Ba_{0.93})_{0.3}Sr_{0.7}SnO_3$ (Figure 77 (a)). The temperature dependent data did not find any superconducting transition for any of the compositions. Two data sets of temperature dependent resistivity are shown in Figure 77 (b).

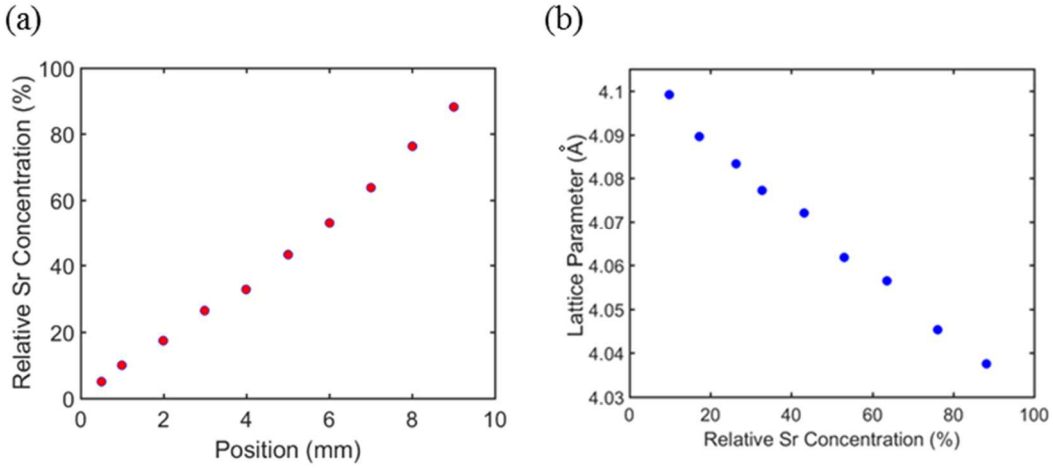

Figure 76: (a) Relative Sr concentration (Sr/(Sr+Ba+La)) vs. position on MgO substrate. (b) Lattice parameter vs. relative Sr concentration of $(La_{0.07}Ba_{0.93})_{1-x}SnO_3$-$Sr_XSnO_3$ compositions.

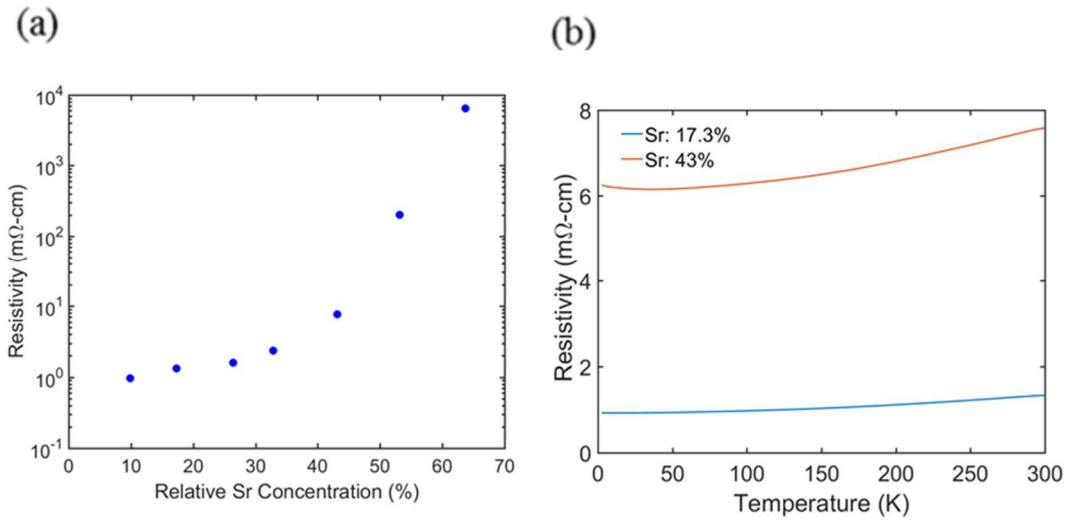

Figure 77: (a) Room temperature resistivity (mΩ-cm) vs. relative Sr concentration (%). (b) Temperature dependent resistivity of the 20 and 43% Sr substitution from 300K to 1.8K.

9.2.2 Combinatorial Films of $BaPb_{0.12}Sn_{0.88}O_3$- $La_{0.5}Ba_{0.5}Pb_{0.12}Sn_{0.88}O_3$

Similar to the Sr based system, one set of Pb based combinatorial films were fabricated on MgO substrates at 600 ºC with $BaPb_{0.12}Sn_{0.88}O_3$ and $La_{0.5}Ba_{0.5}Pb_{0.12}Sn_{0.88}O_3$ targets to investigate the role of excess carriers by La substitution. Since the increasing Pb concentration in BSO reduces the bandgap from the pure BSO, and La is a known n-type dopant with high carrier density, we investigated the combined effects of double substitutions in these compositions for inducing superconductivity. In these samples, La concentration was varied linearly from 0 to 50%. The out-of-plane lattice parameter of the compositions increased gradually with increasing La concentration (Figure 78). No superconductivity was detected in any of the combinatorial $La_xBa_{1-x}Pb_{0.12}Sn_{0.88}O_3$ compositions ($0<x<0.5$). All of the compositions showed semiconducting behavior as resistivity increased with decreasing temperature (Figure 79). The resistivity of

$La_{0.02}Ba_{0.98}Pb_{0.1}Sn_{0.9}O_3$ was the highest among all the compositions at room temperature, and became too high to measure below 60 K due to the limits of PPMS measurement. With increasing La concentrations up to 12%, the resistivity dropped by two orders of magnitude. The lowest resistivity was found 1.3 mΩ-cm for $La_{0.12}Ba_{0.88}Pb_{0.1}Sn_{0.9}O_3$, and showed little variations with decreasing temperature. Afterwards, with increasing La concentration up to 45%, the resistivity increased due to increasing lattice distortion, disordered structure and high concentration of scattering centers.

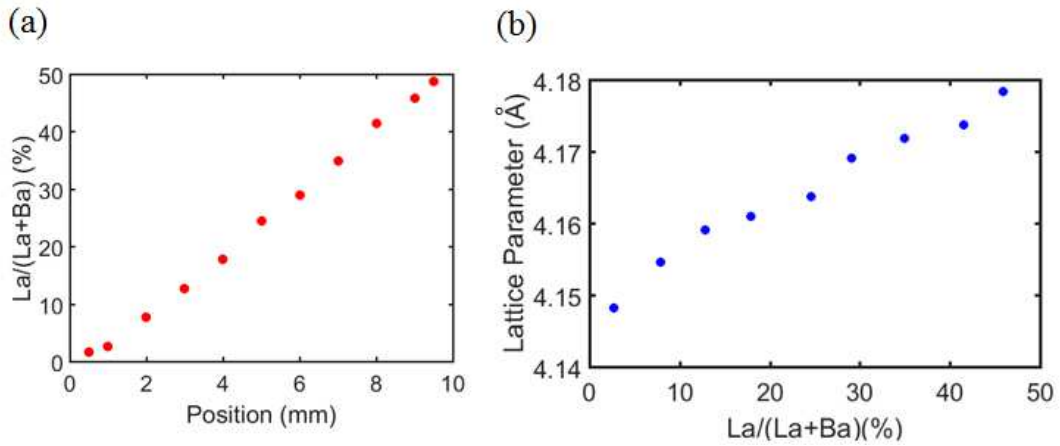

Figure 78: (a) WDS results of the combinatorial $La_xBa_{1-x}Pb_{0.12}Sn_{0.88}O_3$ showing relative La concentration (%) vs. position (mm) on the substrate. (b) Lattice parameter (Å) vs. relative La concentration (%) of the combinatorial $La_xBa_{1-x}Pb_{0.12}Sn_{0.88}O_3$ film.

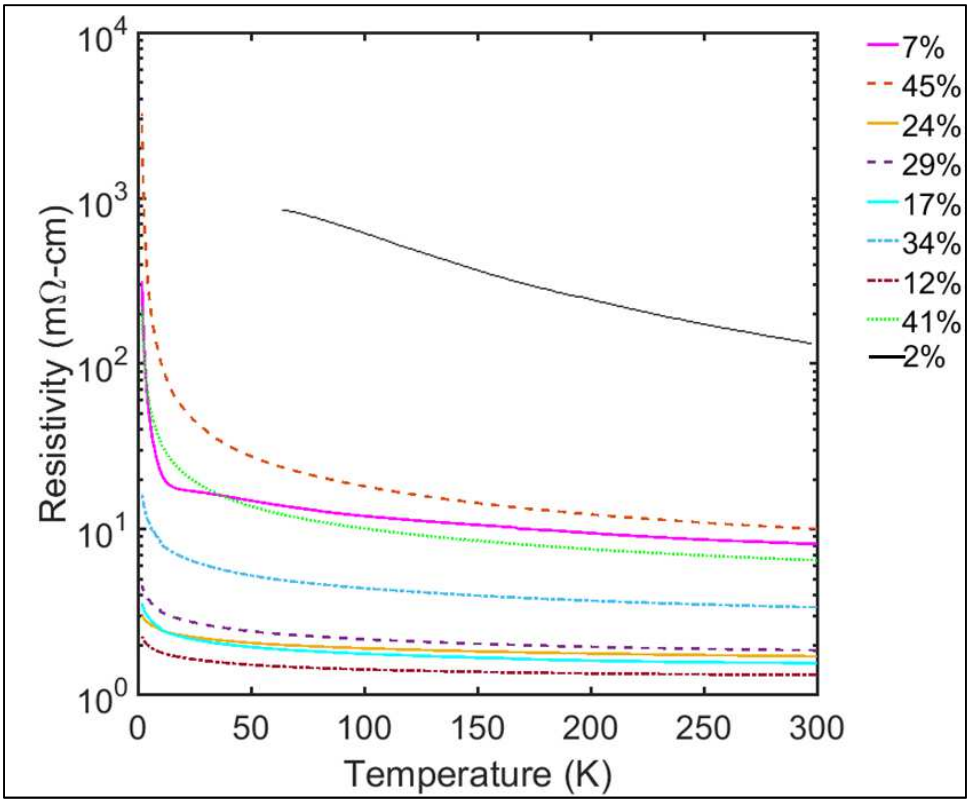

Figure 79: Temperature dependent resistivity (mΩ-cm) of $La_xBa_{1-x}Pb_{0.12}Sn_{0.88}O_3$ compositions from 300K to 1.8K. The relative La concentrations (La/La+Ba) are shown on the right side of the figure.

9.2.3 Combinatorial Films of $BaBi_{0.5}Sn_{0.5}O_3$ - $LaBi_{0.5}Sn_{0.5}O_3$

To investigate the effects of La doping with excess carriers in the BSO-$BaBiO_3$ compositions, combinatorial films were deposited on MgO substrates from the $BaBi_{0.5}Sn_{0.5}O_3$ and $LaBi_{0.5}Sn_{0.5}O_3$ targets at 600 ^oC. The goal was to induce insulator to metal transitions to investigate superconductivity. The composition was varied from $La_xBa_{1-x}Bi_{0.5}Sn_{0.5}O_3$ where $0<x<1$ as shown in Figure 80. At room temperature, the film was completely insulator for all the compositions. The XRD results showed the presence of mixed phases with low crystallinity. The close proximity of the peaks

limited our ability to analyze the phases in detail. The insulating nature might have originated from the disorder and lack of crystallinity.

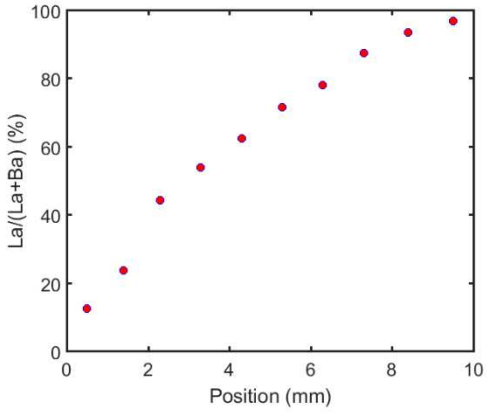

Figure 80: WDS results of the combinatorial La_xBa_{1-x} $Bi_{0.5}Sn_{0.5}O_3$. In the 10 mm long MgO film, the La substitution varied from 0 to 100% in the La_xBa_{1-x} $Bi_{0.5}Sn_{0.5}O_3$.

9.3 Strain Engineering

Substrate-film interface based strain engineering is an established method to induce superconductivity, and change the T_C observed for the relaxed films. In these cases, structural changes were enforced in controlling the superconducting phase diagram. For the films with thickness below 30 nm, superconductivity in the $BaFe_2As_2$ was observed just by tensile lattice strain without charge doping [192]. In these films, the lattice misfit increased the Fe-Fe distance, and induced superconductivity with bulk $T_c \approx 10$ K. Another example of strain engineering for modifying superconducting property is FeSe films on STO. The strain increased the T_c of bulk FeSe from 8 K to almost 60K [193]. Among perovskite superconductors, using epitaxial strain in $La_{1.9}Sr_{0.1}CuO_4$, a critical temperature of 49 K was observed in single-crystal thin films from the bulk value of 25 K [194].

Below critical thickness on mismatched substrates such as LAO, the BSO film will not have cubic crystal structure due to in-plane strain, and the volume of the unit cell will reduce. The distance and angle between the ideal linear O-Sn-O bonding are varied differently based on the thickness [195]. Such deviations have a direct impact on the band structure as the overlap between the Sn 5s – O 2p changes. There are multiple studies on the effect of in-plane strain of BSO. One study was carried out by first-principles based calculations to find ferroelectric property in BSO which predicted multiple high-symmetry phases including a tetragonal phase in BSO based on compressive and tensile strains as shown in Figure 81 [196]. In another study by applying tight-binding models, the effect of the volumetric strain has been calculated. Unlike most of the transition metal based perovskites, BSO showed a great degree of sensitivity in tuning bandgap with varying strains as shown in Figure 82 [128].

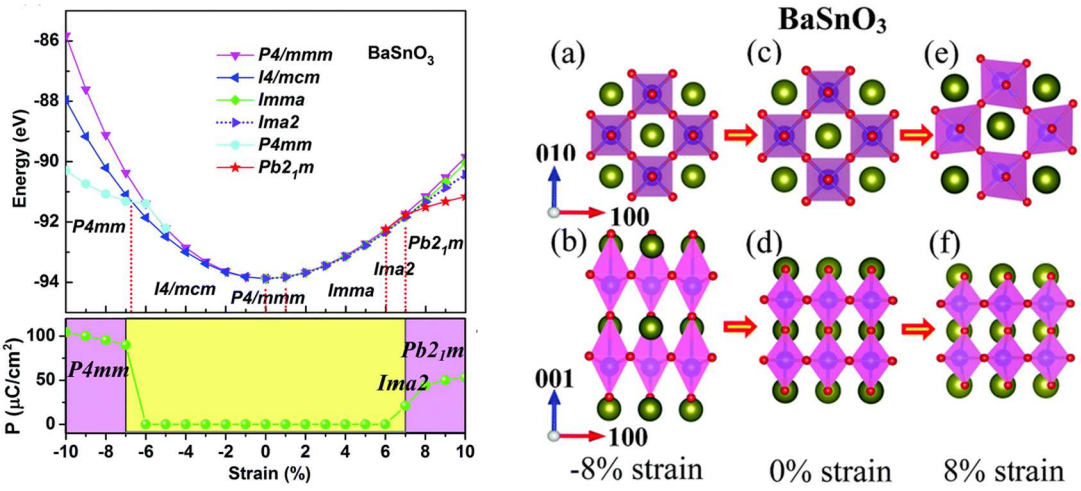

Figure 81: Left: Total energy of various possible ground states and polarization under strain for $BaSnO_3$. Right: (a) top view and (b) side view under 8% compressive strain, (c) top view and (d) side view under zero strain, (e) top view and (f) side view under 8% tensile strain [196].

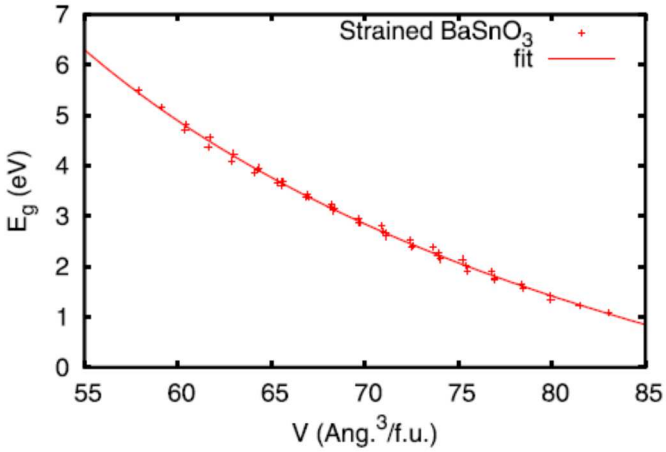

Figure 82: Band gap of strained BSO as a function of volume per formula unit as obtained with the TB-mBJ functional [128]. The unstrained cube has a volume of 69.7 $Å^3$.

In this section, we have studied the role of the lattice strain on $La_{0.07}Ba_{0.93}SnO_3$ by utilizing the 8% lattice mismatch with the LAO substrate. 7% La doping was chosen to create high conductivity and carrier concentration instead of insulating state of original BSO. Although the La^{3+} ionic radius is smaller than the BSO, replacing Ba^{2+} ion increases the out-of-plane lattice parameter in the relaxed films due to the increasing Columbic repulsion rising from the excess charge. Therefore, both doping and structural distortions due to thickness reduction are expected to impact the bandgap of the strained $La_{0.07}Ba_{0.93}SnO_3$.

At first, we fabricated $La_{0.07}Ba_{0.93}SnO_3$ single films on LAO substrates of 10 and 20 nm thicknesses at 760 ^oC under 1×10^{-1} Torr. Interestingly, we observed an insulating nature for the 10 nm film which was strained and showed low crystallinity. The lattice parameter of this film was 4.095 Å. The conducting 20 nm thick $La_{0.07}Ba_{0.93}SnO_3$ film had a lattice parameter of 4.125 Å and showed relaxed behavior in the RSM plot of the (103) plane (Figure 83 (b)). To further investigate the role of the

thickness on transport properties, a thickness gradient film of 20 to 50 nm thickness was fabricated on LAO substrate. The temperature dependent resistance showed similar semiconducting behavior for different positions, and resistance curves of 28, 38, 44 and 47 nm thick positions are plotted in Figure 84. Therefore, although sub 10 nm $La_{0.07}Ba_{0.93}SnO_3$ on LAO substrates showed insulating behavior, the increasing thickness gradient did not induce superconductivity and the transport properties were independent of the film thickness.

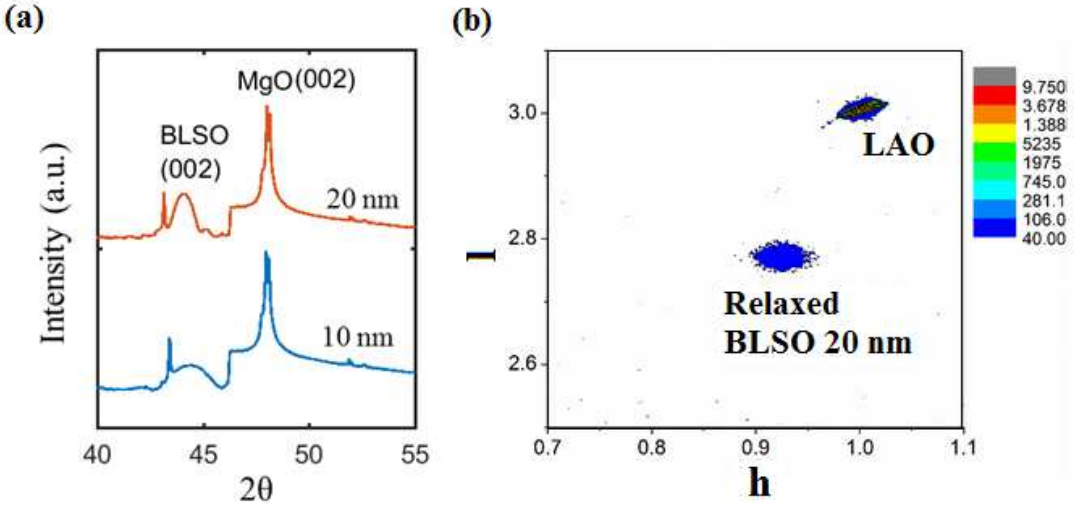

Figure 83: (a) XRD of 10 and 20 nm thick $La_{0.07}Ba_{0.93}SnO_3$ in semi-log scale. (b) RSM of (103) plane of 20 nm thick $La_{0.07}Ba_{0.93}SnO_3$ on LAO.

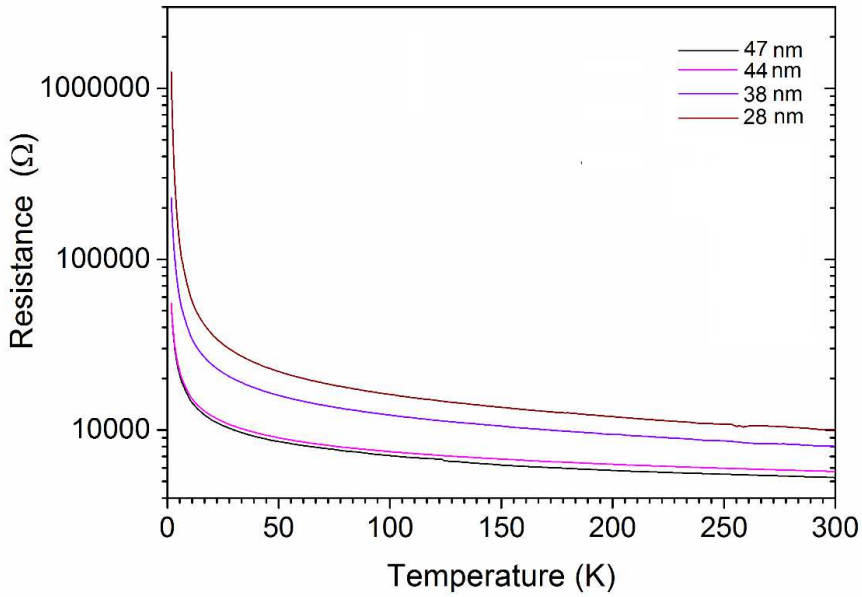

Figure 84: Thickness dependent resistance as a function of temperature of $La_{0.07}Ba_{0.93}SnO_3$ film on LAO from 300K to 1.8K.

9.4 Conclusion

We investigated the role of excess carrier injection in Sr, Pb and Bi substituted BSO to search for superconductivity. La doped BSO-SSO and BSO-BPO showed conducting nature for certain compositions while Bismuth based compositions were completely insulating at room temperature. We also investigated the role of strain for modifying the electronic properties in BLSO. Excess carriers by La doping or strain engineering did not induce superconducting nature in these compositions.

References

1 Schlesinger, J.M.: 'U.S. to Probe Aluminum as It Presses China on Trade', The Wall Street Journal, 2017, https://www.wsj.com/articles/u-s-sets-china-aluminum-probe-as-it-presses-on-trade-1511900565

2 Miles, T.: 'U.S. may put emergency tariffs on solar imports', 2017 https://www.reuters.com/article/us-usa-solar-wto/u-s-may-put-emergency-tariffs-on-solar-imports-idUSKBN18P1JL

3 Prakash, A., Xu, P., Faghaninia, A., Shukla, S., Ager III, J.W., Lo, C.S., and Jalan, B.: 'Wide bandgap BaSnO3 films with room temperature conductivity exceeding 104 S cm^{-1}', Nat Commun, 2017, 8
4 Park, J., Kim, U., and Char, K.: 'Photoconductivity of transparent perovskite semiconductor $BaSnO_3$ and $SrTiO_3$ epitaxial thin films', Applied Physics Letters, 2016, 108, (9)
5 Kim, H.M., Kim, U., Park, C., Kwon, H., and Char, K.: 'Thermally stable pn-junctions based on a single transparent perovskite semiconductor $BaSnO_3$', Apl Materials, 2016, 4, (5)
6 Cerda, J., Arbiol, J., Dezanneau, G., Dıaz, R., and Morante, J.: 'Perovskite-type $BaSnO_3$ powders for high temperature gas sensor applications', Sensors and Actuators B: chemical, 2002, 84, (1), pp. 21-25
7 Hussain, A.M., Pan, K.-J., Robinson, I.A., Hays, T., and Wachsman, E.D.: 'Stannate-based ceramic oxide as anode materials for oxide-ion conducting low-temperature solid oxide fuel cells', J Electrochem Soc, 2016, 163, (10), pp. F1198-F1205
8 Kim, H.J., Kim, U., Kim, T.H., Kim, J., Kim, H.M., Jeon, B.-G., Lee, W.-J., Mun, H.S., Hong, K.T., and Yu, J., Char, K., Kim, K. K., 'Physical properties of transparent perovskite oxides (Ba, La)SnO_3 with high electrical mobility at room temperature', Phys Rev B, 2012, 86, (16), pp. 165205
9 Cheung, J., and Horwitz, J.: 'Pulsed laser deposition history and laser-target interactions', MRS bulletin, 1992, 17, (02), pp. 30-36
10 Jaim, H.I., Aguilar, J., Sarabi, B., Rosen, Y., Ramanayaka, A., Lock, E., Richardson, C., and Osborn, K.: 'Superconducting tin films sputtered over a large range of substrate dc bias', IEEE Transactions on Applied Superconductivity, 2015, 25, (3), pp. 1-5
11 Cole, D.P., Riddick, J.C., Iftekhar Jaim, H., Strawhecker, K.E., and Zander, N.E.: 'Interfacial mechanical behavior of 3D printed ABS', Journal of Applied Polymer Science, 2016, 133, (30)
12 Jaim, H.M. I., Cole, D.P., and Salamanca-Riba, L.G.: 'Surface Analysis of sp^2 Carbon in Ag and Al Covetic Alloys', APS March Meeting 2016.
13 Salamanca-Riba, L., Ge, X., Isaacs, R., Jaim, H.M.I., Wuttig, M., Rashkeev, S., Kuklja, M., Hu, L., and Team, Covetic: 'Graphene-like Networks in the lattice of Ag, Cu and Al metals', APS March Meeting 2016.
14 Salamanca-Riba, L., Isaacs, R., Wuttig, M., LeMieux, M., Hu, L., Jaim, H.M.I., Rashkeev, S., Kukla, M., Rabin, O., and Mansour, A.: '3D Epitaxy of Graphene nanostructures in the Matrix of Ag, Al and Cu', APS March Meeting 2015.
15 http://www.alcotec.com/us/en/education/knowledge/techknowledge/understanding-the-alloys-of-aluminum.cfm'
16 'ASM Specialty Handbook: Aluminum and Aluminum Alloys' (ASM International 1993)
17 Masuda, K., Tsujimura, K., Shinoda, K., and Kato, T.: 'Silver-promoted catalyst for removal of nitrogen oxides from emission of diesel engines', Applied Catalysis B: Environmental, 1996, 8, (1), pp. 33-40

18 An, J., Zhang, M., Wang, S., and Tang, J.: 'Physical, chemical and microbiological changes in stored green asparagus spears as affected by coating of silver nanoparticles-PVP', LWT - Food Science and Technology, 2008, 41, (6), pp. 1100-1107
19 Allen, M.J., Tung, V.C., and Kaner, R.B.: 'Honeycomb carbon: a review of graphene', Chemical reviews, 2009, 110, (1), pp. 132-145
20 Vanin, M., Mortensen, J.J., Kelkkanen, A., Garcia-Lastra, J.M., Thygesen, K.S., and Jacobsen, K.W.: 'Graphene on metals: A van der Waals density functional study', Phys Rev B, 2010, 81, (8), pp. 081408
21 Giovannetti, G., Khomyakov, P., Brocks, G., Karpan, V.v., Van den Brink, J., and Kelly, P.J.: 'Doping graphene with metal contacts', Physical review letters, 2008, 101, (2), pp. 026803
22 Qiu, C., and Metselaar, R.: 'Solubility of Carbon in Liquid Al and Stability of Al_4C_3', J Alloy Compd, 1994, 216, (1), pp. 55-60
23 Karakaya, I., and Thompson, W.: 'The Ag− C (silver-carbon) system', Journal of Phase Equilibria, 1988, 9, (3), pp. 226-227
24 Subramaniam, C., Yamada, T., Kobashi, K., Sekiguchi, A.,Futaba, D. N.,Yumura, M.,Hata, K.: 'One hundred fold increase in current carrying capacity in a carbon nanotube-copper composite', Nat Commun, 2013, 4, pp. 2202
25 Reed, J.C., Zhu, H., Zhu, A.Y., Li, C., and Cubukcu, E.: 'Graphene-enabled silver nanoantenna sensors', Nano letters, 2012, 12, (8), pp. 4090-4094
26 Jeyasimman, D., Sivaprasad, K., Sivasankaran, S., and Narayanasamy, R.: 'Fabrication and consolidation behavior of Al 6061 nanocomposite powders reinforced by multi-walled carbon nanotubes', Powder Technology, 2014, 258, pp. 189-197
27 Bastwros, M., Kim, G. Y.,Zhu, C.,Zhang, K.,Wang, S. R.,Tang, X. D.,Wang, X. W.: 'Effect of ball milling on graphene reinforced Al6061 composite fabricated by semi-solid sintering', Composites Part B-Engineering, 2014, 60, pp. 111-118
28 Ogawa, F., and Masuda, C.: 'Fabrication of carbon nanofiber-reinforced aluminum matrix composites assisted by aluminum coating formed on nanofiber surface by in situ chemical vapor deposition', Materials Research Express, 2015, 2, (1), pp. 015601
29 Jeon, C.H., Jeong, Y. H., Seo, J. J.,Tien, H. N.,Hong, S. T.,Yum, Y. J.,Hur, S. H.,Lee, K. J.: 'Material Properties of Graphene/Aluminum Metal Matrix Composites Fabricated by Friction Stir Processing', International Journal of Precision Engineering and Manufacturing, 2014, 15, (6), pp. 1235-1239
30 Bakshi, S.R., Singh, V., Balani, K., McCartney, D. G., Seal, S., Agarwal, A.: 'Carbon nanotube reinforced aluminum composite coating via cold spraying', Surface & Coatings Technology, 2008, 202, (21), pp. 5162-5169
31 Laha, T., Agarwal, A., McKechnie, T., and Seal, S.: 'Synthesis and characterization of plasma spray formed carbon nanotube reinforced aluminum composite', Mat Sci Eng a-Struct, 2004, 381, (1-2), pp. 249-258
32 Laha, T., Chen, Y., Lahiri, D., and Agarwal, A.: 'Tensile properties of carbon nanotube reinforced aluminum nanocomposite fabricated by plasma spray forming', Composites Part a-Applied Science and Manufacturing, 2009, 40, (5), pp. 589-594

33 Liao, J.Z., and Tan, M.J.: 'Mixing of carbon nanotubes (CNTs) and aluminum powder for powder metallurgy use', Powder Technology, 2011, 208, (1), pp. 42-48
34 Kumar, K.H., and Raghavan, V.: 'A thermodynamic analysis of the Al-C-Fe system', Journal of phase equilibria, 1991, 12, (3), pp. 275-286
35 Simensen, C.J.: 'Comments on the solubility of carbon in molten aluminum', Metallurgical Transactions A, 1989, 20, pp. 191-191
36 Isaacs, R.A., Zhu, H., Preston, C., Mansour, A., LeMieux, M., Zavalij, P. Y., Jaim, H. M. I., Rabin, O.,Hu, L.,Salamanca-Riba, L. G.: 'Nanocarbon-copper thin film as transparent electrode', Applied Physics Letters, 2015, 106, (19), pp. 193108
37 Isaacs, R.A., Jaim, H.M.I., Cole, D.P., Gaskell, K., Rabin, O., and Salamanca-Riba, L.G.: 'Synthesis and characterization of copper-nanocarbon films with enhanced stability', Carbon, 2017, 122, pp. 336-343
38 Salamanca-Riba, L.G., Isaacs, Romaine A., LeMieux, Melburne C.,Wan, Jiayu,Gaskell, Karen,Jiang, Yeping,Wuttig, Manfred,Mansour, Azzam N.,Rashkeev, Sergey N.,Kuklja, Maija M.,Zavalij, Peter Y.,Santiago, Jaime R.,Hu, Liangbing: 'Synthetic Crystals of Silver with Carbon: 3D Epitaxy of Carbon Nanostructures in the Silver Lattice', Advanced Functional Materials, 2015, 25, (30), pp. 4768-4777
39 Brown, L., Joyce, P., Forrest, D., and Salamanca-Riba, L.: 'Physical and Mechanical Characterization of a Nanocarbon Infused Aluminum-Matrix Composite', Materials Performance and Characterization, 2014, 3, (1), pp. 20130023
40 Dresselhaus, M.S., Jorio, A., Hofmann, M., Dresselhaus, G., and Saito, R.: 'Perspectives on carbon nanotubes and graphene Raman spectroscopy', Nano Lett, 2010, 10, (3), pp. 751-758
41 Cong, C., Yu, T., Saito, R., Dresselhaus, G.F., and Dresselhaus, M.S.: 'Second-order overtone and combination Raman modes of graphene layers in the range of 1690− 2150 cm^{-1}', ACS nano, 2011, 5, (3), pp. 1600-1605
42 Eklund, P., Holden, J., and Jishi, R.: 'Vibrational modes of carbon nanotubes; spectroscopy and theory', Carbon, 1995, 33, (7), pp. 959-972
43 Suenaga, K., and Koshino, M.: 'Atom-by-atom spectroscopy at graphene edge', Nature, 2010, 468, (7327), pp. 1088-1090
44 Egerton, R., and Whelan, M.: 'Electron energy loss spectra of diamond, graphite and amorphous carbon', Journal of Electron Spectroscopy and Related Phenomena, 1974, 3, (3), pp. 232-236
45 http://eels.kuicr.kyoto-u.ac.jp/eels.en.html
46 https://xpssimplified.com/elements/carbon.php
47 Kosynkin, D.V., Higginbotham, A.L., Sinitskii, A., Lomeda, J.R., Dimiev, A., Price, B.K., and Tour, J.M.: 'Longitudinal unzipping of carbon nanotubes to form graphene nanoribbons', Nature, 2009, 458, (7240), pp. 872-876
48 Jia, X., Campos-Delgado, J., Terrones, M., Meunier, V., and Dresselhaus, M.S.: 'Graphene edges: a review of their fabrication and characterization', Nanoscale, 2011, 3, (1), pp. 86-95
49 Jaim, H.M.I., Isaacs, R.A., Rashkeev, S.N., Kuklja, M., Cole, D.P., LeMieux, M.C., Jasiuk, I., Nilufar, S., and Salamanca-Riba, L.G.: 'Sp^2 carbon embedded in Al-6061 and Al-7075 alloys in the form of crystalline graphene nanoribbons', Carbon, 2016, 107, pp. 56-66

50 Jaim, H.M.I., Cole, D.P., and Salamanca-Riba, L.G.: 'Characterization of carbon nanostructures in Al and Ag covetic alloys', Carbon, 2017, 111, pp. 309-321
51 Hauert, R., Patscheider, J., Tobler, M., and Zehringer, R.: 'Xps Investigation of the a-Ch/Al Interface', Surface Science, 1993, 292, (1-2), pp. 121-129
52 Schwan, J., Ulrich, S., Batori, V., Ehrhardt, H., and Silva, S.: 'Raman spectroscopy on amorphous carbon films', J Appl Phys, 1996, 80, (1), pp. 440-447
53 Shimizu, T., Haruyama, J., Marcano, D.C., Kosinkin, D.V., Tour, J.M., Hirose, K., and Suenaga, K.: 'Large intrinsic energy bandgaps in annealed nanotube-derived graphene nanoribbons', Nat Nanotechnol, 2011, 6, (1), pp. 45-50
54 Jovanovic, S., Da Ross, T., Ostric, A., Tosic, D., Prekodravac, J., Markovic, Z., and Markovic, B.T.: 'Raman spectroscopy of graphene nanoribbons synthesized by longitudinal unzipping of multiwall carbon nanotubes', Physica Scripta, 2014, T162, pp. 014023
55 Iqbal, M., Singh, A.K., Iqbal, M., and Eom, J.: 'Raman fingerprint of doping due to metal adsorbates on graphene', Journal of Physics: Condensed Matter, 2012, 24, (33), pp. 335301
56 Yang, X.X., Li, J.W., Zhou, Z.F., Wang, Y., Yang, L.W., Zheng, W.T., and Sun, C.Q.: 'Raman spectroscopic determination of the length, strength, compressibility, Debye temperature, elasticity, and force constant of the C-C bond in graphene', Nanoscale, 2012, 4, (2), pp. 502-510
57 Gupta, A.K., Russin, T.J., Gutiérrez, H.R., and Eklund, P.C.: 'Probing Graphene Edges via Raman Scattering', ACS Nano, 2009, 3, (1), pp. 45-52
58 Graf, D., Molitor, F., Ensslin, K., Stampfer, C., Jungen, A., Hierold, C., and Wirtz, L.: 'Spatially resolved raman spectroscopy of single- and few-layer graphene', Nano Letters, 2007, 7, (2), pp. 238-242
59 Mohiuddin, T., Lombardo, A., Nair, R., Bonetti, A., Savini, G., Jalil, R., Bonini, N., Basko, D., Galiotis, C., Marzari, N., Novoselov, K., Geim, A., and Ferrari, A.: 'Uniaxial strain in graphene by Raman spectroscopy: G peak splitting, Grüneisen parameters, and sample orientation', Phys Rev B, 2009, 79, (20)
60 Cong, C., Yu, T., Sato, K., Shang, J., Saito, R., Dresselhaus, G.F., and Dresselhaus, M.S.: 'Raman characterization of ABA-and ABC-stacked trilayer graphene', ACS nano, 2011, 5, (11), pp. 8760-8768
61 Voloshina, E., Generalov, A., Weser, M., Böttcher, S., Horn, K., and Dedkov, Y.S.: 'Structural and electronic properties of the graphene/Al/Ni (111) intercalation system', New Journal of Physics, 2011, 13, (11), pp. 113028
62 Enderlein, C., Kim, Y., Bostwick, A., Rotenberg, E., and Horn, K.: 'The formation of an energy gap in graphene on ruthenium by controlling the interface', New Journal of Physics, 2010, 12, (3), pp. 033014
63 Wang, W.X., Liang, S.H., Yu, T., Li, D.H., Li, Y.B., and Han, X.F.: 'The study of interaction between graphene and metals by Raman spectroscopy', J Appl Phys, 2011, 109, (7), pp. 07C501
64 Yang, X., Li, J., Zhou, Z., Wang, Y., Yang, L., Zheng, W., and Sun, C.Q.: 'Raman spectroscopic determination of the length, strength, compressibility, Debye temperature, elasticity, and force constant of the C–C bond in graphene', Nanoscale, 2012, 4, (2), pp. 502-510

65 Wang, Y.Y., Ni, Z.H., Yu, T., Shen, Z.X., Wang, H.M., Wu, Y.H., Chen, W., and Shen Wee, A.T.: 'Raman studies of monolayer graphene: the substrate effect', The Journal of Physical Chemistry C, 2008, 112, (29), pp. 10637-10640
66 Ni, Z.H., Yu, T., Lu, Y.H., Wang, Y.Y., Feng, Y.P., and Shen, Z.X.: 'Uniaxial Strain on Graphene: Raman Spectroscopy Study and Band-Gap Opening', ACS Nano, 2008, 2, (11), pp. 2301-2305
67 Tilley, R.J.: 'Perovskites: structure-property relationships' (John Wiley & Sons, 2016. 2016)
68 Ogino, H., Matsumura, Y., Katsura, Y., Ushiyama, K., Horii, S., Kishio, K., and Shimoyama, J..: 'Superconductivity at 17 K in $(Fe_2P_2)(Sr_4Sc_2O_6)$: a new superconducting layered pnictide oxide with a thick perovskite oxide layer', Superconductor Science and Technology, 2009, 22, (7), pp. 075008
69 Galasso, F.S.: 'Perovskites and high-T_c superconductors', 1990
70 Fiebig, M., Lottermoser, T., Meier, D., and Trassin, M.: 'The evolution of multiferroics', Nature Reviews Materials, 2016, 1, pp. 16046
71 Grinberg, I., West, D.V., Torres, M., Gou, G., Stein, D.M., Wu, L., Chen, G., Gallo, E.M., Akbashev, A.R., and Davies, P.K.: 'Perovskite oxides for visible-light-absorbing ferroelectric and photovoltaic materials', Nature, 2013, 503, (7477), pp. 509-512
72 Huang, J., Yuan, Y., Shao, Y., and Yan, Y.: 'Understanding the physical properties of hybrid perovskites for photovoltaic applications', Nature Reviews Materials, 2017, 2, pp. 17042
73 Sutherland, B.R., and Sargent, E.H.: 'Perovskite photonic sources', Nat Photon, 2016, 10, (5), pp. 295-302
74 Yang, S., Fu, W., Zhang, Z., Chen, H., and Li, C.-Z.: 'Recent advances in perovskite solar cells: efficiency, stability and lead-free perovskite', Journal of Materials Chemistry A, 2017
75 Park, N.-G.: 'Perovskite solar cells: an emerging photovoltaic technology', Materials Today, 2015, 18, (2), pp. 65-72
76 Snaith, H.J.: 'Perovskites: the emergence of a new era for low-cost, high-efficiency solar cells', The Journal of Physical Chemistry Letters, 2013, 4, (21), pp. 3623-3630
77 Hancock, C., Porras-Vazquez, J., Keenan, P., and Slater, P.: 'Oxyanions in perovskites: from superconductors to solid oxide fuel cells', Dalton Transactions, 2015, 44, (23), pp. 10559-10569
78 Ishihara, T.: 'Perovskite oxide for solid oxide fuel cells' (Springer Science & Business Media, 2009. 2009)
79 Seyfi, B., Baghalha, M., and Kazemian, H.: 'Modified $LaCoO_3$ nano-perovskite catalysts for the environmental application of automotive CO oxidation', Chemical Engineering Journal, 2009, 148, (2), pp. 306-311
80 Fang, Y., Liu, Y., and Zhang, L.: 'LaFeO 3-supported nano Co-Cu catalysts for higher alcohol synthesis from syngas', Applied Catalysis A: General, 2011, 397, (1), pp. 183-191
81 Pintilie, L., Boldyreva, K., Alexe, M., and Hesse, D.: 'Capacitance tuning in antiferroelectric–ferroelectric $PbZrO_3$–Pb $(Zr_{0.8}Ti_{0.2})O_3$ epitaxial multilayers', New Journal of Physics, 2008, 10, (1), pp. 013003

82 Vrejoiu, I., Alexe, M., Hesse, D., and Gösele, U.: 'Functional perovskites–from epitaxial films to nanostructured arrays', Advanced Functional Materials, 2008, 18, (24), pp. 3892-3906
83 Bednorz, J.G., and Müller, K.A.: 'Possible highTc superconductivity in the Ba−La−Cu−O system', Zeitschrift für Physik B Condensed Matter, 1986, 64, (2), pp. 189-193
84 Borisov, P., Hochstrat, A., Chen, X., Kleemann, W., and Binek, C.: 'Magnetoelectric switching of exchange bias', Physical Review Letters, 2005, 94, (11), pp. 117203
85 Zavaliche, F., Zheng, H., Mohaddes-Ardabili, L., Yang, S., Zhan, Q., Shafer, P., Reilly, E., Chopdekar, R., Jia, Y., and Wright, P.: 'Electric field-induced magnetization switching in epitaxial columnar nanostructures', Nano letters, 2005, 5, (9), pp. 1793-1796
86 Eerenstein, W., Mathur, N., and Scott, J.F.: 'Multiferroic and magnetoelectric materials', nature, 2006, 442, (7104), pp. 759-765
87 Sasaki, S., Prewitt, C.T., Bass, J.D., and Schulze, W.: 'Orthorhombic perovskite CaTiO3 and CdTiO3: structure and space group', Acta Crystallographica Section C: Crystal Structure Communications, 1987, 43, (9), pp. 1668-1674
88 Yusa, H., Sata, N., and Ohishi, Y.: 'Rhombohedral (9R) and hexagonal (6H) perovskites in barium silicates under high pressure', American Mineralogist, 2007, 92, (4), pp. 648-654
89 Misra, D., and Kundu, T.K.: 'Oxygen vacancy induced metal-insulator transition in $LaNiO_3$', The European Physical Journal B, 2016, 89, (1), pp. 4
90 Jacobsson, T.J., Schwan, L.J., Ottosson, M., Hagfeldt, A., and Edvinsson, T.: 'Determination of thermal expansion coefficients and locating the temperature-induced phase transition in methylammonium lead perovskites using x-ray diffraction', Inorganic chemistry, 2015, 54, (22), pp. 10678-10685
91 Li, D., Wang, G., Cheng, H.-C., Chen, C.-Y., Wu, H., Liu, Y., Huang, Y., and Duan, X.: 'Size-dependent phase transition in methylammonium lead iodide perovskite microplate crystals', Nat Commun, 2016, 7
92 Lu, Q., and Yildiz, B.: 'Voltage-controlled topotactic phase transition in thin-film $SrCoO_x$ monitored by in situ X-ray diffraction', Nano letters, 2016, 16, (2), pp. 1186-1193
93 Ullah, A., Malik, R.A., Ullah, A., Lee, D.S., Jeong, S.J., Lee, J.S., Kim, I.W., and Ahn, C.W.: 'Electric-field-induced phase transition and large strain in lead-free Nb-doped BNKT-BST ceramics', Journal of the European Ceramic Society, 2014, 34, (1), pp. 29-35
94 Wang, L., Wang, K., Xiao, G., Zeng, Q., and Zou, B.: 'Pressure-Induced Structural Evolution and Band Gap Shifts of Organometal Halide Perovskite-Based Methylammonium Lead Chloride', J. Phys. Chem. Lett, 2016, 7, (24), pp. 5273-5279
95 Dagotto, E.: 'Complexity in strongly correlated electronic systems', Science, 2005, 309, (5732), pp. 257-262
96 Laukhin, V., Fontcuberta, J., Garcia-Munoz, J., and Obradors, X.: 'Pressure effects on the metal-insulator transition in magnetoresistive manganese perovskites', Phys Rev B, 1997, 56, (16), pp. R10009

97 Obradors, X., Paulius, L., Maple, M., Torrance, J., Nazzal, A., Fontcuberta, J., and Granados, X.: 'Pressure dependence of the metal-insulator transition in the charge-transfer oxides $RNiO_3$ (R= Pr, Nd, $Nd_{0.7}La_{0.3}$)', Phys Rev B, 1993, 47, (18), pp. 12353
98 Medvedeva, I., Bärner, K., Rao, G., Hamad, N., Bersenev, Y.S., and Sun, J.: 'Pressure dependences of the metal–insulator transition temperature of $La_{0.7}Ca_{0.3}Mn_{1-x}(Fe/Ge)_xO_3$ perovskites', Physica B: Condensed Matter, 2000, 292, (3), pp. 250-256
99 Frand, G., Bohnke, O., Lacorre, P., Fourquet, J., Carré, A., Eid, B., Théobald, J., and Gire, A.: 'Tuning of Metal/Insulator Transition around Room Temperature of Perovskites $Sm_{1-x}Nd_xNiO_3$', J Solid State Chem, 1995, 120, (1), pp. 157-163
100 Sanchez, R., Causa, M., Caneiro, A., Butera, A., Vallet-Regi, M., Sayagues, M., Gonzalez-Calbet, J., Garcia-Sanz, F., and Rivas, J.: 'Metal-insulator transition in oxygen-deficient $LaNiO_{3-x}$ perovskites', Phys Rev B, 1996, 54, (23), pp. 16574
101 Raychaudhuri, A.: 'Metal-insulator transition in perovskite oxides: a low-temperature perspective', Advances in Physics, 1995, 44, (1), pp. 21-46
102 Strukov, D.B., Snider, G.S., Stewart, D.R., and Williams, R.S.: 'The missing memristor found', Nature, 2008, 453, (7191), pp. 80-83
103 Lüders, U., Barthélémy, A., Bibes, M., Bouzehouane, K., Fusil, S., Jacquet, E., Contour, J.P., Bobo, J.F., Fontcuberta, J., and Fert, A.: '$NiFe_2O_4$: a versatile spinel material brings new opportunities for spintronics', Advanced Materials, 2006, 18, (13), pp. 1733-1736
104 Biscaras, J., Bergeal, N., Kushwaha, A., Wolf, T., Rastogi, A., Budhani, R.C., and Lesueur, J.: 'Two-dimensional superconductivity at a Mott-Insulator/Band-Insulator interface: $LaTiO_3/SrTiO_3$', arXiv preprint arXiv:1002.3737, 2010
105 Yun, H., Ganguly, K., Prakash, A., Leighton, C., Jalan, B., Mkhoyan, K.A., and Jeong, J.S.: 'Study of Strain and Intermixing at the $BaSnO_3/SrTiO_3$ and $BaSnO_3/LaAlO_3$ Interfaces Using STEM and EELS', Microscopy and Microanalysis, 2016, 22, pp. 320
106 Kim, D.H., Aimon, N.M., Sun, X., and Ross, C.A.: 'Compositionally modulated magnetic epitaxial spinel/perovskite nanocomposite thin films', Advanced Functional Materials, 2014, 24, (16), pp. 2334-2342
107 Kim, U., Park, C., Ha, T., Kim, Y.M., Kim, N., Ju, C., Park, J., Yu, J., Kim, J.H., and Char, K.: 'All-perovskite transparent high mobility field effect using epitaxial BaSnO3 and LaInO3', APL materials, 2015, 3, (3), pp. 036101
108 Miyano, K., Tanaka, T., Tomioka, Y., and Tokura, Y.: 'Photoinduced insulator-to-metal transition in a perovskite manganite', Physical review letters, 1997, 78, (22), pp. 4257
109 Yang, W.S., Park, B.-W., Jung, E.H., Jeon, N.J., Kim, Y.C., Lee, D.U., Shin, S.S., Seo, J., Kim, E.K., and Noh, J.H.: 'Iodide management in formamidinium-lead-halide–based perovskite layers for efficient solar cells', Science, 2017, 356, (6345), pp. 1376-1379
110 Wang, W., Tadé, M.O., and Shao, Z.: 'Research progress of perovskite materials in photocatalysis-and photovoltaics-related energy conversion and environmental treatment', Chemical Society Reviews, 2015, 44, (15), pp. 5371-5408

111 Esaka, T., Sakaguchi, H., and Kobayashi, S.: 'Hydrogen storage in proton-conductive perovskite-type oxides and their application to nickel–hydrogen batteries', Solid State Ionics, 2004, 166, (3), pp. 351-357
112 Lokanc, M., Eggert, R., and Redlinger, M.: 'The Availability of Indium: The Present, Medium Term, and Long Term' (National Renewable Energy Lab.(NREL), Golden, CO (United States), 2015)
113 Allen, G.: 'NanoMarkets predicts entire transparent conductor market to reach 5.6 billion dollars in 2015', http://www.azonano.com/news.aspx?newsID=18021
114 Jewell, S.: 'Mineral Commodity Summaries 2016 ', (2016), pp. 30
115 Kim, H.J., Kim, U., Kim, H.M., Kim, T.H., Mun, H.S., Jeon, B.-G., Hong, K.T., Lee, W.-J., Ju, C., and Kim, K.H.: 'High mobility in a stable transparent perovskite oxide', Applied Physics Express, 2012, 5, (6), pp. 061102
116 Fei, X., Luo, B.C., Jin, K.X., and Chen, C.L.: 'Electrical and optical behaviors of La-doped $BaSnO_3$ thin film', Acta Physica Sinica, 2015, 64, (20)
117 Kumar, A., Choudhary, R., Singh, B., and Thakur, A.K.: 'Effect of strontium concentration on electrical conduction properties of Sr-modified $BaSnO_3$', Ceram Int, 2006, 32, (1), pp. 73-83
118 Lu, Z., Chen, L., Tang, Y., and Li, Y.: 'Preparation and luminescence properties of Eu^{3+}-doped $MSnO_3$ (M= Ca, Sr and Ba) perovskite materials', J Alloy Compd, 2005, 387, (1), pp. L1-L4
119 Liu, Q.Z., Dai, J.M., Liu, Z.L., Zhang, X.B., Zhu, G.P., and Ding, G.H.: 'Electrical and optical properties of Sb-doped $BaSnO_3$ epitaxial films grown by pulsed laser deposition', J Phys D Appl Phys, 2010, 43, (45)
120 Lee, S., Wang, H., Gopal, P., Shin, J., Jaim, H.M.I., Zhang, X., Jeong, S.-Y., Usanmaz, D., Curtarolo, S., Fornari, M., Buongiorno Nardelli, M., and Takeuchi, I.: 'Systematic Band Gap Tuning of BaSnO3 via Chemical Substitutions: The Role of Clustering in Mixed-Valence Perovskites', Chemistry of Materials, 2017
121 Alaan, U.S., N'Diaye, A.T., Shafer, P., Arenholz, E., and Suzuki, Y.: 'Structure and magnetism of Fe-doped $BaSnO_3$ thin films', AIP Advances, 2017, 7, (5), pp. 055716
122 Mizoguchi, H., Chen, P., Boolchand, P., Ksenofontov, V., Felser, C., Barnes, P.W., and Woodward, P.M.: 'Electrical and Optical Properties of Sb-Doped BaSnO3', Chemistry of Materials, 2013, 25, (19), pp. 3858-3866
123 Joo, B.S., Chang, Y.J., Moreschini, L., Bostwick, A., Rotenberg, E., and Han, M.: 'Evidence for indirect band gap in $BaSnO_3$ using angle-resolved photoemission spectroscopy', Current Applied Physics, 2017, 17, (5), pp. 595-599
124 Moreira, E., Henriques, J.M., Azevedo, D.L., Caetano, E.W.S., Freire, V.N., and Albuquerque, E.L.: 'Structural and electronic properties of $Sr_xBa_{1-x}SnO_3$ from first principles calculations', J Solid State Chem, 2012, 187, pp. 186-194
125 Stanislavchuk, T., Sirenko, A., Litvinchuk, A., Luo, X., and Cheong, S.-W.: 'Electronic band structure and optical phonons of $BaSnO_3$ and $Ba_{0.97}La_{0.03}SnO_3$ single crystals: Theory and experiment', J Appl Phys, 2012, 112, (4), pp. 044108
126 Scanlon, D.O.: 'Defect engineering of $BaSnO_3$ for high-performance transparent conducting oxide applications', Phys Rev B, 2013, 87, (16), pp. 161201
127 Kim, B.G., Jo, J., and Cheong, S.: 'Hybrid functional calculation of electronic and phonon structure of $BaSnO_3$', J Solid State Chem, 2013, 197, pp. 134-138

128 Singh, D.J., Xu, Q., and Ong, K.P.: 'Strain effects on the band gap and optical properties of perovskite $SrSnO_3$ and $BaSnO_3$', Applied Physics Letters, 2014, 104, (1), pp. 011910
129 Luo, B.C., Cao, X.S., Jin, K.X., and Chen, C.L.: 'Determination of the effective mass and nanoscale electrical transport in La-doped BaSnO3 thin films', Current Applied Physics, 2016, 16, (1), pp. 20-23
130 Lee, W.-J., Kim, H.J., Kang, J., Jang, D.H., Kim, T.H., Lee, J.H., and Kim, K.H.: 'Transparent Perovskite Barium Stannate with High Electron Mobility and Thermal Stability', Annual Review of Materials Research, 2017, (0)
131 Kim, U., Park, C., Ha, T., Kim, Y.M., Kim, N., Ju, C., Park, J., Yu, J., Kim, J.H., and Char, K.: 'All-perovskite transparent high mobility field effect using epitaxial BaSnO3 and LaInO3', Apl Materials, 2015, 3, (3)
132 Park, C., Kim, U., Ju, C.J., Park, J.S., Kim, Y.M., and Char, K.: 'High mobility field effect transistor based on $BaSnO_3$ with Al_2O_3 gate oxide', Applied Physics Letters, 2014, 105, (20), pp. 203503
133 Zhu, L., Shao, Z., Ye, J., Zhang, X., Pan, X., and Dai, S.: 'Mesoporous BaSnO 3 layer based perovskite solar cells', Chemical Communications, 2016, 52, (5), pp. 970-973
134 Lampe, U., Gerblinger, J., and Meixner, H.: 'Nitrogen oxide sensors based on thin films of BaSnO3', Sensors and Actuators B: Chemical, 1995, 26, (1–3), pp. 97-98
135 Lampe, U., Gerblinger, J., and Meixner, H.: 'Carbon-monoxide sensors based on thin films of $BaSnO_3$', Sensors and Actuators B: Chemical, 1995, 25, (1), pp. 657-660
136 Doroftei, C., Popa, P., and Iacomi, F.: 'Study of the influence of nickel ions substitutes in barium stannates used as humidity resistive sensors', Sensors and Actuators A: Physical, 2012, 173, (1), pp. 24-29
137 Krishnaswamy, K., Bjaalie, L., Himmetoglu, B., Janotti, A., Gordon, L., and Van de Walle, C.G.: '$BaSnO_3$ as a channel material in perovskite oxide heterostructures', Applied Physics Letters, 2016, 108, (8), pp. 083501
138 Lee, W.J., Kim, H.J., Sohn, E., Kim, H.M., Kim, T.H., Char, K., Kim, J.H., and Kim, K.H.: 'Oxygen diffusion process in a $Ba_{0.96}La_{0.04}SnO_3$ thin film on $SrTiO_3$ (001) substrate as investigated by time-dependent Hall effect measurements', physica status solidi (a), 2015, 212, (7), pp. 1487-1493
139 Bayraktaroglu, B., Leedy, K., and Bedford, R.: 'High temperature stability of postgrowth annealed transparent and conductive ZnO: Al films', Applied Physics Letters, 2008, 93, (2), pp. 022104
140 Pavlenko, N., Kopp, T., Tsymbal, E.Y., Sawatzky, G.A., and Mannhart, J.: 'Magnetic and superconducting phases at the $LaAlO_3/SrTiO_3$ interface: The role of interfacial Ti 3d electrons', Phys Rev B, 2012, 85, (2), pp. 020407
141 Shin, S.S., Kim, J.S., Suk, J.H., Lee, K.D., Kim, D.W., Park, J.H., Cho, I.S., Hong, K.S., and Kim, J.Y.: 'Improved quantum efficiency of highly efficient perovskite $BaSnO_3$-based dye-sensitized solar cells', ACS nano, 2013, 7, (2), pp. 1027-1035

142 Mizoguchi, H., Woodward, P.M., Park, C.-H., and Keszler, D.A.: 'Strong Near-Infrared Luminescence in $BaSnO_3$', J Am Chem Soc, 2004, 126, (31), pp. 9796-9800
143 Maekawa, T., Kurosaki, K., and Yamanaka, S.: 'Thermal and mechanical properties of polycrystalline $BaSnO_3$', J Alloy Compd, 2006, 416, (1), pp. 214-217
144 Kumar, A., Singh, B., Choudhary, R., and Thakur, A.K.: 'AC Impedance analysis of the effect of dopant concentration on electrical properties of calcium modified $BaSnO_3$', J Alloy Compd, 2005, 394, (1), pp. 292-302
145 Lu, W., Jiang, S., Zhou, D., and Gong, S.: 'Structural and electrical properties of $Ba(Sn,Sb)O_3$ electroceramics materials', Sensors and Actuators A: Physical, 2000, 80, (1), pp. 35-37
146 Jayaraman, V., Mangamma, G., Gnanasekaran, T., and Periaswami, G.: 'Evaluation of $BaSnO_3$ and $Ba(Zr,Sn)O_3$ solid solutions as semiconductor sensor materials', Solid State Ionics, 1996, 86-88, (Part 2), pp. 1111-1114
147 Shimoyama, J.-i., Kase, J.-i., Kondoh, S., Yanagisawa, E., Matsubara, T., Suzuki, M., and Morimoto, T.: 'Addition of new pinning center to unidirectionally melt solidified Y-Ba-Cu-O superconductor', Japanese Journal of Applied Physics, 1990, 29, (11A), pp. L1999
148 Luo, X., Oh, Y.S., Sirenko, A., Gao, P., Tyson, T., Char, K., and Cheong, S.-W.: 'High carrier mobility in transparent $Ba_{1-x}La_xSnO_3$ crystals with a wide band gap', Applied Physics Letters, 2012, 100, (17), pp. 172112
149 Galazka, Z., Uecker, R., Irmscher, K., Klimm, D., Bertram, R., Kwasniewski, A., Naumann, M., Schewski, R., Pietsch, M., and Juda, U.: 'Melt growth and properties of bulk BaSnO3 single crystals', Journal of Physics: Condensed Matter, 2016, 29, (7), pp. 075701
150 Raghavan, S., Schumann, T., Kim, H., Zhang, J.Y., Cain, T.A., and Stemmer, S.: 'High-mobility $BaSnO_3$ grown by oxide molecular beam epitaxy', Apl Materials, 2016, 4, (1)
151 Chambers, S.A., Kaspar, T.C., Prakash, A., Haugstad, G., and Jalan, B.: 'Band alignment at epitaxial $BaSnO_3/SrTiO_3(001)$ and $BaSnO_3/LaAlO_3(001)$ heterojunctions', Applied Physics Letters, 2016, 108, (15)
152 James, K., Krishnaprasad, P., Hasna, K., and Jayaraj, M.: 'Structural and optical properties of La-doped $BaSnO_3$ thin films grown by PLD', Journal of Physics and Chemistry of Solids, 2015, 76, pp. 64-69
153 Liu, Q.Z., Liu, J.J., Li, B., Li, H., Zhu, G.P., Dai, K., Liu, Z.L., Zhang, P., and Dai, J.M.: 'Composition dependent metal-semiconductor transition in transparent and conductive La-doped BaSnO3 epitaxial films', Applied Physics Letters, 2012, 101, (24)
154 Shan, C., Huang, T., Zhang, J., Han, M., Li, Y., Hu, Z., and Chu, J.: 'Optical and Electrical Properties of Sol–Gel Derived $Ba_{1-x}La_xSnO_3$ Transparent Conducting Films for Potential Optoelectronic Applications', The Journal of Physical Chemistry C, 2014, 118, (13), pp. 6994-7001
155 Wei, R., Tang, X., Hui, Z., Luo, X., Dai, J., Yang, J., Song, W., Chen, L., Zhu, X., and Zhu, X.: 'Solution processing of transparent conducting epitaxial La: $BaSnO_3$ films with improved electrical mobility', Applied Physics Letters, 2015, 106, (10), pp. 101906

156 Ganguly, K., Ambwani, P., Xu, P., Jeong, J.S., Mkhoyan, K.A., Leighton, C., and Jalan, B.: 'Structure and transport in high pressure oxygen sputter-deposited $BaSnO_3$-delta', Apl Materials, 2015, 3, (6)
157 Shin, S.S., Yeom, E.J., Yang, W.S., Hur, S., Kim, M.G., Im, J., Seo, J., Noh, J.H., and Seok, S.I.: 'Colloidally prepared La-doped $BaSnO_3$ electrodes for efficient, photostable perovskite solar cells', Science, 2017, 356, (6334), pp. 167-171
158 Shin, J., Kim, Y.M., Kim, Y., Park, C., and Char, K.: 'High mobility BaSnO3 films and field effect transistors on non-perovskite MgO substrate', Applied Physics Letters, 2016, 109, (26), pp. 262102
159 Iga, F., and Nishihara, Y.: 'Metal-Insulator Transition with Oxygen Content in CaVO3-y', Journal of the Physical Society of Japan, 1992, 61, (6), pp. 1867-1870
160 Hu, L., Luo, X., Zhang, K.J., Tang, X.W., Zu, L., Kan, X.C., Chen, L., Zhu, X.B., Song, W.H., Dai, J.M., and Sun, Y.P.: 'Oxygen vacancies-induced metal-insulator transition in $La_{2/3}Sr_{1/3}VO_3$ thin films: Role of the oxygen substrate-to-film transfer', Applied Physics Letters, 2014, 105, (11)
161 Perez-Casero, R., Perriere, J., Gutierrez-Llorente, A., Defourneau, D., Millon, E., Seiler, W., and Soriano, L.: 'Thin films of oxygen-deficient perovskite phases by pulsed-laser ablation of strontium titanate', Physical Review B, 2007, 75, (16), pp. 165317
162 Scott, J., and Dawber, M.: 'Oxygen-vacancy ordering as a fatigue mechanism in perovskite ferroelectrics', Applied Physics Letters, 2000, 76, (25), pp. 3801-3803
163 Alagdal, I.A., and West, A.R.: 'Oxygen stoichiometry, conductivity and gas sensing properties of $BaSnO_3$', Journal of Materials Chemistry C, 2016, 4, (21), pp. 4770-4777
164 Tan, H., Zhao, Z., Zhu, W.-b., Coker, E.N., Li, B., Zheng, M., Yu, W., Fan, H., and Sun, Z.: 'Oxygen vacancy enhanced photocatalytic activity of pervoskite SrTiO3', ACS applied materials & interfaces, 2014, 6, (21), pp. 19184-19190
165 Wang, X., Hu, C., Song, Y., Zhao, X., Zhang, L., Lv, Z., Wang, Y., Liu, Z., Wang, Y., and Zhang, Y.: 'Effect of Oxygen-deficiencies on Resistance Switching in Amorphous $YFe_{0.5}Cr_{0.5}O_{3-\delta}$ films', Scientific Reports, 2016, 6
166 Shang, J., Liu, G., Yang, H., Zhu, X., Chen, X., Tan, H., Hu, B., Pan, L., Xue, W., and Li, R.W.: 'Thermally stable transparent resistive random access memory based on all-oxide heterostructures', Advanced Functional Materials, 2014, 24, (15), pp. 2171-2179
167 Liu, Q.Z., He, Y.H., Li, H., Li, B., Gao, G.Y., Fan, L.L., and Dai, J.M.: 'Room-temperature ferromagnetism in transparent Mn-doped $BaSnO_3$ epitaxial films', Applied Physics Express, 2014, 7, (3)
168 Jaim, H.I., Lee, S., Zhang, X., and Takeuchi, I.: 'Stability of the oxygen vacancy induced conductivity in $BaSnO_3$ thin films on $SrTiO_3$', Applied Physics Letters, 2017, 111, (17), pp. 172102
169 Alaan, U.S., Shafer, P., N'Diaye, A.T., Arenholz, E., and Suzuki, Y.: 'Gd-doped $BaSnO_3$: A transparent conducting oxide with localized magnetic moments', Applied Physics Letters, 2016, 108, (4)
170 Lebens-Higgins, Z., Scanlon, D.O., Paik, H., Sallis, S., Nie, Y., Uchida, M., Quackenbush, N.F., Wahila, M.J., Sterbinsky, G.E., Arena, D.A., Woicik, J.C., Schlom, D.G., and Piper, L.F.J.: 'Direct Observation of Electrostatically Driven Band

Gap Renormalization in a Degenerate Perovskite Transparent Conducting Oxide', Physical Review Letters, 2016, 116, (2), pp. 027602
171 Wang, H., Liu, Q., Chen, F., Gao, G., Wu, W., and Chen, X.: 'Transparent and conductive oxide films with the perovskite structure: La-and Sb-doped $BaSnO_3$', J App Phys, 101, 106105 (2007)
172 Kumar, A., Singh, B.P., Choudhary, R.N.P., and Thakur, A.K.: 'Ferroelectric phase transition in Te-modified $BaSnO_3$', Materials Letters, 2005, 59, (14–15), pp. 1880-1888
173 Liu, Q., Dai, J., Liu, Z., Zhang, X., Zhu, G., and Ding, G.: 'Electrical and optical properties of Sb-doped $BaSnO_3$ epitaxial films grown by pulsed laser deposition', Journal of Physics D: Applied Physics, 2010, 43, (45), pp. 455401
174 Li, B., Liu, Q.Z., Zhang, Y.X., Liu, Z.L., and Geng, L.: 'Highly conductive Nb doped $BaSnO_3$ thin films on MgO substrates by pulsed laser deposition', J Alloy Compd, 2016, 680, pp. 343-349
175 Balamurugan, K., Kumar, N.H., Ramachandran, B., Rao, M.S.R., Chelvane, J.A., and Santhosh, P.N.: 'Magnetic and optical properties of Mn-doped BaSnO3', Solid State Commun, 2009, 149, (21-22), pp. 884-887
176 Mizoguchi, H., Eng, H.W., and Woodward, P.M.: 'Probing the Electronic Structures of Ternary Perovskite and Pyrochlore Oxides Containing Sn4+ or Sb5+', Inorganic Chemistry, 2004, 43, (5), pp. 1667-1680
177 Sleight, A.W., Gillson, J., and Bierstedt, P.: 'High-temperature superconductivity in the $BaPb_{1-x}Bi_xO3$ systems', Solid State Commun, 1975, 17, (1), pp. 27-28
178 Chaillout, C., Remeika, J.P., Santoro, A., and Marezio, M.: 'The determination of the Bi valence state in $BaBiO_3$ by neutron powder diffraction data', Solid State Commun, 1985, 56, (10), pp. 829-831
179 Yaowen, S., Zizhong, Z., and Meichun, H.: 'Theoretical electronic structure of oxide $BaBiO_3$', Communications in theoretical physics, 1998, 30, (3), pp. 387
180 Namatame, H., Fujimori, A., Takagi, H., Uchida, S., De Groot, F., and Fuggle, J.: 'Electronic structure and the metal-semiconductor transition in $BaPb_{1-x}Bi_xO_3$ studied by photoemission and x-ray-absorption spectroscopy', Phys Rev B, 1993, 48, (23), pp. 16917
181 Sleight, A.W.: 'High-temperature superconductivity in oxides' (ACS Publications, 1987)
182 Cava, R., and Batlogg, B.: 'Superconductivity at High Temperatures Without Copper: $Ba_{1-x}K_xBiO_3$', MRS Bulletin, 1989, 14, (1), pp. 49-52
183 Nicoletti, D., Casandruc, E., Fu, D., Giraldo-Gallo, P., Fisher, I., and Cavalleri, A.: 'Anomalous relaxation kinetics and charge-density-wave correlations in underdoped $BaPb_{1-x}Bi_xO3$', Proceedings of the National Academy of Sciences, 2017, 114, (34), pp. 9020-9025
184 Uchida, S., Kitazawa, K., and Tanaka, S.: 'Superconductivity and metal-semiconductor transition in $BaPb_{1-x}BixO_3$', Phase Transitions, 1987, 8, (2), pp. 95-128
185 Taraphder, A., Pandit, R., Krishnamurthy, H., and Ramakrishnan, T.: 'The exotic barium bismuthates', International Journal of Modern Physics B, 1996, 10, (08), pp. 863-955

186 Braden, M., Reichardt, W., Elkaim, E., Lauriat, J., Shiryaev, S., and Barilo, S.: 'Structural distortion in superconducting $Ba_{1-x}K_xBiO_3$', Phys Rev B, 2000, 62, (10), pp. 6708
187 Giraldo-Gallo, P., Lee, H., Zhang, Y., Kramer, M., Beasley, M., Geballe, T., and Fisher, I.: 'Field-tuned superconductor-insulator transition in $BaPb_{1-x}Bi_xO_3$', Phys Rev B, 2012, 85, (17), pp. 174503
188 Climent-Pascual, E., Ni, N., Jia, S., Huang, Q., and Cava, R.: 'Polymorphism in $BaPb_{1-x}Bi_xO_3$ at the superconducting composition', Phys Rev B, 2011, 83, (17), pp. 174512
189 Medvedeva, J.E., and Hettiarachchi, C.L.: 'Tuning the properties of complex transparent conducting oxides: Role of crystal symmetry, chemical composition, and carrier generation', Phys Rev B, 2010, 81, (12), pp. 125116
190 Aliev, A.E., Xiong, K., Cho, K., and Salamon, M.B.: 'Reversible superconductivity in electrochromic indium-tin oxide films', Applied Physics Letters, 2012, 101, (25), pp. 252603
191 Makise, K., Kokubo, N., Takada, S., Yamaguti, T., Ogura, S., Yamada, K., Shinozaki, B., Yano, K., Inoue, K., and Nakamura, H.: 'Superconductivity in transparent zinc-doped In_2O_3 films having low carrier density', Science and technology of advanced materials, 2009, 9, (4), pp. 044208
192 Engelmann, J., Grinenko, V., Chekhonin, P., Skrotzki, W., Efremov, D., Oswald, S., Iida, K., Hühne, R., Hänisch, J., and Hoffmann, M.: 'Strain induced superconductivity in the parent compound $BaFe_2As_2$', arXiv preprint arXiv:1312.2107, 2013
193 Tan, S., Zhang, Y., Xia, M., Ye, Z., Chen, F., Xie, X., Peng, R., Xu, D., Fan, Q., and Xu, H.: 'Interface-induced superconductivity and strain-dependent spin density waves in FeSe/$SrTiO_3$ thin films', Nature materials, 2013, 12, (7), pp. 634-640
194 Locquet, J.-P., Perret, J., Fompeyrine, J., Mächler, E., Seo, J.W., and Van Tendeloo, G.: 'Doubling the critical temperature of $La_{1.9}Sr_{0.1}CuO_4$ using epitaxial strain', Nature, 1998, 394, (6692), pp. 453-456
195 Baniecki, J.D., Yamazaki, T., Ricinschi, D., Van Overmeere, Q., Aso, H., Miyata, Y., Yamada, H., Fujimura, N., Maran, R., and Anazawa, T.: 'Strain Dependent Electronic Structure and Band Offset Tuning at Heterointerfaces of $ASnO_3$ (A= Ca, Sr, and Ba) and $SrTiO_3$', Scientific Reports, 2017, 7
196 Zhang, Y., Wang, J., Sahoo, M., Shimada, T., and Kitamura, T.: 'Strain-induced ferroelectricity and lattice coupling in $BaSnO_3$ and $SrSnO_3$', Physical Chemistry Chemical Physics, 2017, 19, (38), pp. 26047-26055